



Title	Theoretical Study of Gap Opening/Closing Control of Dirac Cone Using Spin-dependent Potentials in Graphene-based Magnetic Junctions
Author(s)	Wicaksono, Yusuf
Citation	大阪大学, 2022, 博士論文
Version Type	VoR
URL	https://doi.org/10.18910/89505
rights	
Note	

The University of Osaka Institutional Knowledge Archive : OUKA

<https://ir.library.osaka-u.ac.jp/>

The University of Osaka

**Theoretical Study of Gap Opening/Closing
Control of Dirac Cone Using Spin-dependent
Potentials in Graphene-based Magnetic
Junctions**

YUSUF WICAKSONO

JUNE 2022

Theoretical Study of Gap Opening/Closing Control of Dirac Cone Using Spin-dependent Potentials in Graphene-based Magnetic Junctions

A dissertation submitted to
THE GRADUATE SCHOOL OF ENGINEERING SCIENCE
OSAKA UNIVERSITY
in partial fulfillment of the requirements for the degree of
DOCTOR OF PHILOSOPHY IN ENGINEERING

BY

YUSUF WICAKSONO
JUNE 2022

ABSTRACT

In this thesis, a theoretical study is presented based on the first-principles calculation of four main topics on the controllable mass-gapped Dirac cone (MGDC) mechanism of graphene using spin-dependent potentials in graphene-based magnetic junctions. Using a specific stacking configuration design at the interface of graphene sandwiching with magnetic materials, MGDC of graphene can be open and close depending on the magnetic alignment of the upper and lower magnetic materials. A systematic study within spin-polarized generalized-gradient approximation on the interface is presented to understand the influence of physical and chemical properties at the interface that affect the optimum control of MGDC of graphene and its efficiency as a spintronic device. By understanding the origin and characteristics of controllable MGDC of graphene, a successful graphene-based magnetic junction device with high spintronic performance can be created.

At the beginning of this thesis (chapter 1), the introduction to magnetic junctions, their development, and the recent consideration of 2D materials-based magnetic junctions for spintronic devices is presented. The problems that need to be solved, the aims of the research, and the strategy for addressing the problem are also presented. Afterward, the theoretical basis of the computational method used in the research and the physics of graphene and its characters in magnetic junction is discussed in chapter 2. Next, Chapter 3 presents the theoretical framework of the considered design and the computational approach strategy in the simulation.

In the first study (Chapter 4), Ni(111)/graphene/Ni(111) magnetic junction is proposed. Ni(111) slabs are used due to their similar structures to graphene, that is, having the smallest lattice mismatch among transition metals. In this proposed system, the MGDC of graphene can be controlled using the magnetic alignment of the Ni slabs. When the magnetic moments of the upper and lower Ni(111) slabs have an antiparallel configuration (APC), the MGDC is open. However, when the magnetic moments of the upper and lower Ni(111) slabs have parallel configuration (PC), the MGDC is closed. This unique characteristic is because the most stable arrangement of the Ni/graphene/Ni heterostructure occurs when Ni atoms of the upper and lower Ni(111) slabs at the interfaces are hybridized with different graphene sublattices. In other words, Ni atoms from the lower Ni(111) slab hybridized with

C atoms in sublattice A (i.e., C_A), and Ni atoms from the upper Ni(111) slab hybridized with C atoms in sublattice B (i.e., C_B). Although the C atoms of graphene bond with the Ni atoms, this unique hybridization preserves the equipotential between sublattices A and B. Meanwhile, a magnetic moment is induced on the graphene layer by charge transfer from the Ni to C atoms. Therefore, the induced magnetic moments of the C_A and C_B atoms depended on the magnetic alignment of the Ni(111) slabs. Moreover, the induced magnetic moments between C_A and C_B atoms exhibit antiferromagnetic and ferromagnetic orders when the APC and PC states are considered, respectively. This characteristic implies that the pseudospin between sublattices A and B can be controlled to preserve or break the chiral symmetry, making the MGDC controllable.

In the second study (Chapter 5), a theoretical study is presented on the in-plane conductance of graphene partially sandwiched between Ni(111) nanostructures with a width of 12.08 Å. The investigation of the proposed system is conducted to understand the effectiveness of a controllable MGDC of graphene on its in-plane conductance to realize a high magnetoresistance (MR) ratio. The APC and PC states of the upper and lower Ni(111) structures are considered. First-principles quantum transport calculations, which coupled density functional theory (DFT) with the non-equilibrium Green's function, were performed. In the sandwiched part, the MGDC of the graphene was controlled using a pseudospin by changing the magnetic alignment of the Ni(111) nanostructures, in which the mechanism is the same as explained in Chapter 4. Upon considering the APC of Ni(111) nanostructures, the transmission probability calculation of the in-plane conductance of graphene shows a gap-like transmission at $E - E_F = 0.2$ and 0.65 eV from pd-hybridization and controllable MGDC of graphene, respectively. In the PC, the transmission probability calculation showed a profile similar to the pristine graphene. High and colossal in-plane MR ratios of 284% and 3100% were observed at $E - E_F = 0.65$ and 0.2 eV, respectively. A higher MR ratio beyond 3100% was expected at $E - E_F = 0.65$ eV when the width of the Ni(111) nanostructures on the nanometer scale.

The MR changes beyond the charge neutrality point can be overcome by several methods-one of them is by introducing a gate voltage. Thus, the hBN layer can be introduced between the graphene layer and the Ni slabs to optimize the controllability of graphene's Fermi energy while keeping the performance of MGDC controllability. The controllable induced magnetic moment

on graphene is replaced through charge transfer to magnetic proximity effect. The van der Waals interactions between graphene and hBN layers led to easy controllability of graphene Fermi energy by using gate voltage. However, prior to further investigation on the effectivity of proximity effect on controlling MGDC of graphene, understanding how the Ni(111) surface state as evanescent wave work on graphene created magnetic proximity effect is necessary.

In the third study (Chapter 6), a theoretical study is conducted to understand the origin of the magnetic proximity effect in 2D material which was sandwiched with ferromagnetic metal. In this study, a Ni/nhBN/Ni magnetic junctions was considered. First, a study on Ni/2hBN/Ni magnetic junctions showed that the Ni's surface state (111) becomes the main contribution to the tunneling transmission of the electrons when electrons flow from one Ni slab to another through two hBN layers. When the number of hBN is increased to three, the Ni(111) slabs' surface state still survives, giving a magnetic proximity effect on middle hBN. However, the magnetic proximity effect on middle hBN is weak enough since the d_z^2 -orbital of the Ni(111) surface state works on unfilled p_z -orbital of B atoms. However, the d_z^2 -orbital of the Ni(111) surface state works significantly on the graphene layer since it works on π -orbital of graphene. Further study to understand the effectivity of proximity effect on controlling MGDC of graphene is discussed in the next chapter.

In the fourth study (Chapter 7), a study is performed on the role of Ni/hBN slab-graphene interface of Ni/hBN-graphene-hBN/Ni magnetic junction in controlling MGDC of graphene via magnetic proximity effect. The spin-polarized DFT calculation was performed on 12 possible stacking configurations for APC and PC of Ni slabs' magnetic alignment. The 12 stacking configurations can be categorized into three groups based on the relative total energy, corresponding to van der Waals' interaction between hBN and graphene. In group I, the magnetic proximity effect of B atoms on graphene causes the opening and closing MGDC with a small gap size when N atoms are placed on top or below the hollow site of graphene. In group II, when the proximity effect of the Ni(111) surface state as evanescent wave acts on C atoms, both the APC and PC states have one-spin channel with a prominent size of mass-gapped, whereas the other does not. In group III, the MGDC is open with a significant gap size in the APC state and close in the PC state when the asymmetric arrangement of N atoms on different sublattices of graphene is considered. The unique characteristics of graphene's MGDC control, depending on the stacking configuration, can be proposed as a device where

a controllable MGDC is tuned using mechanical motion. Spin-mechatronics device can be realized by proposing a device that can move the upper and lower Ni(111)/hBN slabs translationally. Afterward, the investigation of the several possible barriers between Ni(111) slabs and graphene beside hBN was considered.

Finally, the complete understanding of controlling MGDC of graphene through various approaches is summarized in chapter 8. The results become a foundation for realizing a spintronic device based on graphene in-plane conductance. Furthermore, the new findings show the high performance of graphene-based magnetic junction spintronic devices and functionality beyond the conventional spintronic device.

Keywords: graphene; magnetic junctions; in-plane conductance; magnetoresistance; mass-gapped Dirac cone

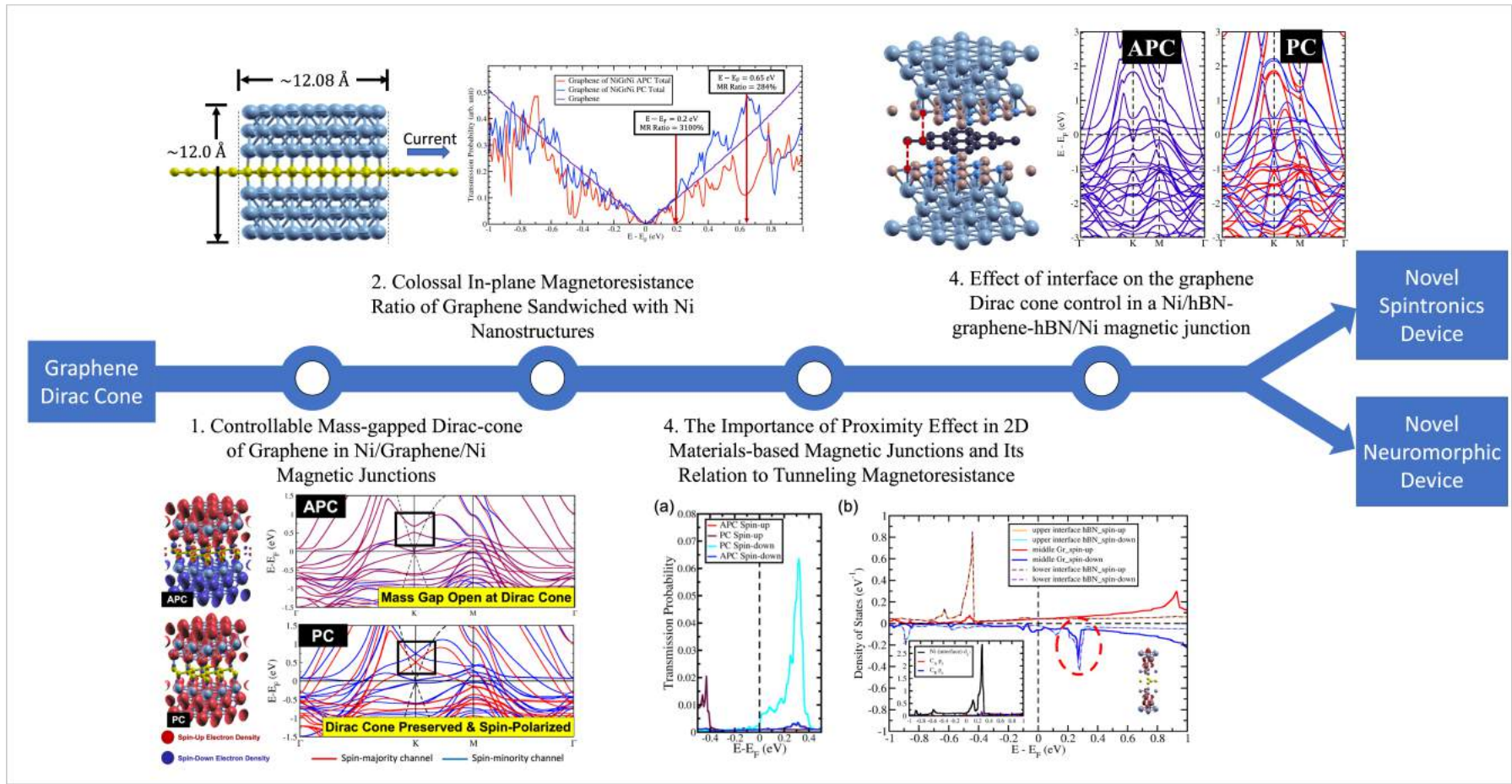


Figure 1: The flow of studies that are presented in this thesis.

This page intentionally left blank

Contents

ABSTRACT	i
CONTENTS	vii
List of Figures	xi
List of Tables	xvii
1 INTRODUCTION	1
1.1 Spintronic Technology through Magnetic Junctions	1
1.1.1 Magnetic Junctions	1
1.1.2 The Development of Spintronics Devices	4
1.1.3 2D Materials-based Spintronics Devices	6
1.2 Strategy and Aim	8
1.3 Thesis Organization	10
2 Theoretical Basis	13
2.1 Review on Many-Body Schrödinger Equation	13
2.1.1 Many-Body Schrödinger Equation	13
2.1.2 Slater Determinant	16
2.1.3 Mean-Field Approximation	19
2.1.4 Hartree–Fock Equations	20
2.2 Density Functional Theory	24
2.2.1 Hohenberg–Kohn theorem	24
2.2.2 The Exchange–Correlation Term	26
2.2.3 The Kohn–Sham Equation	28
2.2.4 Extension to Spin-Polarized DFT	31
2.2.5 Ultrasoft Pseudopotential	32
2.2.6 Monkhorst–Pack Scheme	32
2.3 Theory of Electronic States in Graphene	33

2.3.1	Bloch Theorem	33
2.3.2	Tight-Binding Model	36
2.3.3	Effective Mass Theory	38
2.3.4	Stoner Model	43
2.3.5	Dirac Hamiltonian of Graphene	46
2.3.6	Bandgap Opening on the Graphene Dirac Cone	51
3	COMPUTATIONAL APPROACHES	55
3.1	Theoretical Framework	55
3.2	Model and Computational Strategy	59
3.2.1	Model of Ni/graphene/Ni spin-valve structure	59
3.2.2	Model of Ni/graphene/Ni nano-spin-valve structure for IMR Calculation	61
3.2.3	Model of Ni/nhBN/Ni and Ni/hBN-graphene-hBN/Ni magnetic junctions	62
3.2.4	Model of Ni/hBN-graphene-hBN/Ni spin-valve struc- ture for investigating the possibility on controlling MGDC	64
4	Controllable Mass-gapped Dirac-cone of Graphene in Ni/Graphene/Ni Magnetic Junctions	67
4.1	Introduction	67
4.2	Total energy and magnetic properties	67
4.3	Analysis of electron orbitals for Ni/graphene/Ni with 1-layer Ni slabs	73
4.4	Effect of magnetic configuration on the electronic structure and in-plane conductance	75
4.5	Discussion on the possible application for spin-electronic device	79
4.6	Summary	81
5	Colossal In-plane Magnetoresistance Ratio of Graphene Sand- wiched with Ni Nanostructures	83
5.1	Introduction	83
5.2	Characteristics of Induced Magnetic Moment of Graphene . . .	84
5.3	Colossal In-Plane Magnetoresistance of Graphene	87
5.4	Summary	91
6	The Importance of Proximity Effect in 2D Materials-based Magnetic Junctions and Its Relation to Tunneling Magnetore-	

sistance	93
6.1 Introduction	93
6.2 Transmission Mechanism of Ni/hBN/Ni MTJs with Different Numbers of hBN Layers	94
6.3 High Transmission Magnetoresistance on the Excited State and Influence of the Proximity Effect	98
6.4 Proposed Design and Mechanism of Optically Induced MTJs . .	102
6.5 Summary	103
7 Effect of interface on the graphene Dirac cone control in a Ni/hBN-graphene-hBN/Ni magnetic junction	105
7.1 Introduction	105
7.2 Total energy and magnetic properties of Ni/hBN-graphene-hBN/Ni	106
7.3 Controllable Dirac cone of graphene due to tunable pseudospin term of graphene	111
7.4 Influence of the surface state of Ni works directly on C atoms in the gapped Dirac cone	115
7.5 Controllable mas-gapped Dirac-cone through Ni surface state influence on C atoms	116
7.6 Possible application on the spin mechatronic valve	120
7.7 Summary	121
8 CONCLUSIONS	125
Bibliography	129
Academic Achievements	141
Acknowledgments	147

This page intentionally left blank

List of Figures

1	The flow of studies that are presented in this thesis.	v
1.1	magnetic junction in (a) current-in-plane geometry, so-called spin-valve structure, and (b) current-perpendicular-to-plane geometry, so-called magnetic junctions.	2
1.2	Two electronic states in spin-valve structure: (a) low resistance when PC state is considered and (b) high resistance when APC state is considered.	3
1.3	Two electronic states on magnetic tunnel junction structure: (a) low resistance when the PC state is considered and (b) high resistance when the APC state is considered.	4
1.4	The development of MTJs. Taken from [21]	5
1.5	The calculated conductance and TMR ratio of (a) Ni/ <i>nh</i> BN/Ni and (b)Ni/hBN/ <i>n</i> Gr/Ni (taken from [44]). The proposed spintronics device of graphene act as a bridge between two Ni electrodes (taken from [45]).	7
1.6	The development of 2D materials-based MTJs. Taken from [54]	8
2.1	Structure crystal of graphene in the real space	47
2.2	energy bands of graphene	50
2.3	Band structure of graphene on the top Ni substrate.	52
3.1	Model crystal structures of Ni/graphene/Ni systems. In the left panel (a), the top view of the graphene is depicted. While the proposed model crystal structures of the 3-layer Ni/graphene/3-layer Ni are shown in the (b) AA-stacking structure, (c) BA-stacking structure, and (d) B'A-stacking structure, where the stacking sequences from the graphene to the upper Ni slab are different from one another.	58

3.2	Proposed system of graphene where the middle part is sandwiched by Ni(111) nanostructures. The most stable stacking arrangement from our previous study was considered ²⁴ . The graphene is used as a buffer and electrode.	61
3.3	Side view of the supercell of Ni(111)/3hBN/Ni(111) (as representative of few-layer hBN MTJ) and Ni(111)/hBN-Gr-hBN/Ni(111) used to represent the scattering region and lead corresponding to model calculation for transmission probability calculation.	63
3.4	The proposed twelve stacking configuration of Ni(111)/hBN-Gr-hBN/Ni(111) with the stacking arrangement name.	65
4.1	Spin-charge density of the 3-layer Ni/graphene/3-layer Ni in the (a) anti-parallel configuration (isovalue=0.00170) and (b) parallel configuration (isovalue=0.00168). The charge density in red represents spin-up electron density and that in blue represents spin-down electron density.	70
4.2	Electronic band structure of 1-layer Ni/graphene/1-layer Ni in a non-magnetic state. The black dashed line is the band structure of pristine graphene, to be used as reference. The Dirac cone characteristic can be seen around the K-point high-symmetry and near the Fermi energy as well as around -4 eV.	73
4.3	3-layer Ni/graphene/3-layer Ni band structure in the anti-parallel configuration for the (a) spin majority channel and (b) spin minority channel, and in parallel configuration for the (c) spin majority channel and (d) spin minority channel. The black dashed line is the band structure of the pristine graphene to be used as reference. The Dirac cone characteristic can be seen around the K-point high-symmetry and near the Fermi energy.	76
4.4	Bandstructure of 2-layer Ni/graphene/2-layer Ni in the (a) anti-parallel configuration and (b) parallel configuration; and 4-layer Ni/graphene/4-layer Ni in the (c) anti-parallel configuration and (d) parallel configuration. In (a), (b), (c), and (d), red represents the spin-majority channel, whereas blue represents the spin-minority channel. The black dashed line is the bandstructure of the pristine graphene, taken as a reference.	78
4.5	Scattering region of Ni/Graphene/Ni nano-spin-valve-like structure created on the part of a graphene plane.	79

5.1	Spin-charge density mapping of the proposed system when the Ni(111) nanostructures are in (a) PC and (b) APC states (red: spin-up charge density; blue: spin-down charge density).	84
5.2	The induced magnetic moment of graphene of the proposed system when the Ni(111) nanostructures are in (a) APC and (b) PC states.	86
5.3	The transmission probability of graphene from the proposed system when Ni(111) nanostructures in PC state.	87
5.4	(a) The local density of states (LDOS) of graphene in Ni/graphene/Ni MTJ, (b) projected density of states (PDOS) of C_A and Ni at interface hybridized with C_A , and (c) the transmission probability of graphene from the proposed system when Ni(111) nanostructure in APC state.	88
5.5	(a) The comparison of transmission probability of graphene from the proposed system between APC and PC states. (b) The configuration of gate voltage on the proposed system to shifting the Fermi energy.	90
6.1	The possible charges response when electric field is introduced to the chemical bonding-based interface found in Ni/graphene/Ni MJ (left) and van der Waals-based interface found in Ni/hBN-graphene-hBN/Ni MJ (right).	95
6.2	The TMR ratio vs the number of 2D materials layers as tunnel barrier at two different energies; $E - E_F = 0$ eV (the zero-bias limit) and 0.34 eV (the highest peak of spin-down electrons transmission probability in PC state started from $n = 3$).	96
6.3	(a) The transmission probability of Ni/2hBN/Ni, (b) The spin-charge density mapping (red color represent spin-up charge density mapping) and LDOS of 2hBN insulator barrier in Ni/2hBN/Ni system in PC state, (c) The projected bandstructure of Ni/2hBN/Ni for spin minority channel.	97
6.4	(a) The transmission probability of Ni/3hBN/Ni and (b) The spin charge density mapping of Ni/3hBN/Ni in PC state (red color represent spin-up charge density mapping) and LDOS of 3hBN insulator barrier in Ni/3hBN/Ni system in PC state.	98

6.5	(a) The transmission probability of Ni/4hBN/Ni, (b) The charge density mapping of Ni/4hBN/Ni (red color represent spin-up charge density mapping) and the LDOS of 4hBN insulator barrier of Ni/4hBN/Ni system in PC state, (c) The transmission probability of Ni/5hBN/Ni, and (d) The charge density mapping of Ni/5hBN/Ni (red color represent spin- up charge density mapping) and the LDOS of 5hBN insulator barrier of Ni/5hBN/Ni system in PC state (insert: magnified LDOS of middle hBN of Ni/5hBN/Ni system).	99
6.6	(a) The transmission probability of Ni/hBN-Gr-hBN/Ni and (b) The spin charge density mapping of Ni/hBN-Gr-hBN/Ni (red color represent spin-up charge density mapping) and LDOS of hBN-Gr-hBN insulator barrier of Ni/hBN-Gr-hBN/Ni system in PC state.	101
6.7	(a) The writing and (b) the reading process of Ni/hBN-Gr-hBN/Ni proposed MTJ device with light irradiation.	103
7.1	The relative total energy respect to lowest energy for all proposed stacking configuration and its classification into three groups.	106
7.2	Spin charge density mapping of Ni/hBN-Gr-hBN/Ni magnetic junctions in (a)HC1B-BC2H, (b)BC1B-NC2H, and (c)BC1N-NC2B stacking configurations for APC and PC states. (Red color represent spin-up charge density and blue color represent spin-down charge density)	108
7.3	The band structure of Ni(111)/hBN-Gr-hBN/Ni(111) in (a) HC1H-BC2B and (b) HC1B-BC2H stacking configurations in both APC and PC states.(Red line represent spin majority channel and blue line represent spin minority channel)	115
7.4	The band structure of Ni(111)/hBN-Gr-hBN/Ni(111) in (a)HC1N-BC2H, (b)BC1B-NC2H, (c)HC1H-NC2B and (d)HC1B-BC2N stacking configurations in both APC and PC states.(Red line represent spin majority channel and blue line represent spin minority channel)	116

7.5	The band structure of Ni(111)/hBN-Gr-hBN/Ni(111) in (a)NC1N-HC2H, (b)NC1N-BC2B, and (c)HC1B-NC2N stacking configurations in both APC and PC states.(Red line represent spin majority channel and blue line represent spin minority channel)	118
7.6	The band structure of Ni(111)/hBN-Gr-hBN/Ni(111) in (a)HC1N-NC2H, (b)BC1N-NC2B, and (c)HC1N-NC2B stacking configurations in both APC and PC states.(Red line represent spin majority channel and blue line represent spin minority channel)	119
7.7	The device structure for the proposed application in controlling Dirac cone through mechanical motion. The LDOS of graphene for (a) spin-up and (b) spin-down electrons when Ni/hBN-Gr-hBN/Ni system having HC1B-BC2H, BC1B-NC2H, and BC1N-NC2B stacking configurations.	124

This page intentionally left blank

List of Tables

4.1	Total energy difference for various stacking arrangements of 3Ni/graphene/3Ni. The total energy is expressed in meV relative to the ground state (highlighted in bold font). APC(PC) refers to the antiparallel (parallel) magnetic alignments between the upper and lower nickel slabs	68
4.2	Interlayer distance between the Ni(111) slabs with graphene for three different stacking arrangements. APC(PC) refers to the antiparallel (parallel) magnetic alignment between the upper and lower nickel slabs	69
4.3	Magnetic moment for each atom of 3Ni/graphene/3Ni. AFM(FM) refers to the antiparallel (parallel) magnetic alignment between the upper and lower nickel slabs.	71
4.4	Total energy differences between various numbers of the nickel layer in the BA-stacking arrangement. The total energy is expressed in meV relative to the ground state (highlighted in bold font). APC(PC) refers to the antiparallel (parallel) magnetic alignment between the upper and lower nickel slabs.	72
7.1	The interlayer distance between upper/lower hBN with graphene for all stacking configurations.	107
7.2	The induced magnetic moment on C atoms in sublattice A (C1) and sublattice B (C2) of graphene in both APC and PC states.	109
7.3	The integrated spin-charge density of C1 and C2 in APC and PC states for HC1H-BC2B and HC1B-BC2H stacking configurations.	112
7.4	The integrated spin-charge density of C1 and C2 in APC and PC states for HC1N-BC2H, BC1B-NC2H, HC1H-NC2B and HC1B-BC2N stacking configurations.	112

- 7.5 The integrated spin-charge density of C1 and C2 in APC and PC states for NC1N-HC2H, NC1N-BC2B, HC1B-NC2N, HC1N-NC2H, BC1N-NC2B and HC1N-NC2B stacking configurations. . 113

Chapter 1

INTRODUCTION

1.1 Spintronic Technology through Magnetic Junctions

1.1.1 Magnetic Junctions

Spin-electronics, or so-called spintronics, is a research field that focuses on the manipulation of spin-up and spin-down populations of electrons in solid materials. Manipulating spin polarization to generate inequality in the number of spin-up and spin-down electrons, resulting in a spin current, is the main aim of spintronics materials or devices. A typical way to polarize electron spins is to use a ferromagnetic electrode in electrical contact with a medium where spin-polarized electrons accumulate. The accumulation rate strongly depends on the relaxation or flip of spins, driving the polarization back toward the equilibrium state. The magnetic junctions (MJs) between the ferromagnetic materials with a medium where spin-polarized electrons are accumulated are essential for developing spintronic devices because of their capability to fulfill the high demand for applications based on a spin configuration. These MJs can be categorized into two types based on their mechanism of function.

The first is an MJ with a structure comprising ultrathin nonmagnetic-metal materials sandwiched by ferromagnetic materials, and the current-in-plane (CIP) geometry is considered. This structure is called a "spin-valve." In a spin-valve structure, the current flows along with the layers, and the electrodes are located on one side of the structure, as shown in Fig. 1.1(a). The Albert Fert groups from the University of Paris-Sud, France, and Peter Grünberg from Forschungszentrum Jülich, Germany, introduced this structure in 1988 [1,2]. The practical significance of this experimental discovery was recognized

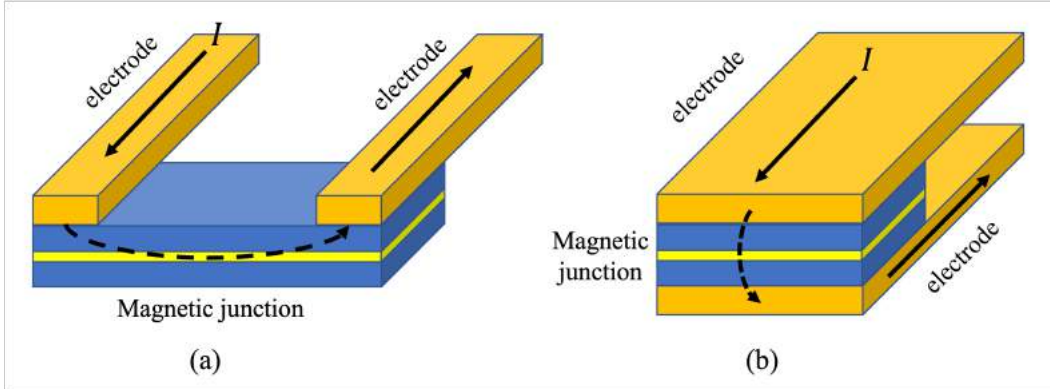


Figure 1.1: magnetic junction in (a) current-in-plane geometry, so-called spin-valve structure, and (b) current-perpendicular-to-plane geometry, so-called magnetic junctions.

by the Nobel Prize in Physics awarded to Fert and Grünberg in 2007. This structure is proven important as hard-drive magnetic read heads and magnetic sensors [3]. On the other hand, the second structure is the so-called magnetic tunnel junction (MTJ). MTJ is a structure comprising an ultrathin layer of a nonmagnetic insulator sandwiched by ferromagnetic materials. In MTJ, the current-perpendicular-to-plane (CPP) configuration is considered, where the current is passed perpendicular to the layers. The electrodes are located on different sides of the superlattice. Thus, the ultrathin insulator leads to the tunneling of electrons through the barrier when a bias voltage is applied to the upper and lower ferromagnetic electrodes, as shown in Fig. 1.1(b). This device structure was introduced by Julliere in 1975 [4] and by Maekawa and Gafvert in 1982 [5]. Nowadays, this structure is used in memory storage and logic devices [6–11].

Both spin-valve and MTJ have the same functionality, where the conductance through the device corresponds to the magnetic alignment of the ferromagnetic layer. In both spin-valve and MTJ, one ferromagnetic layer has a fixed magnetic orientation. In comparison, another one has a controllable magnetic alignment, resulting in two configurations of magnetic alignment between two ferromagnetic layers, parallel configuration (PC) and antiparallel configuration (APC). In the PC state, the conductance through the device is high, whereas in the APC state, the conductance is low. However, spin-valve and MTJ have different origins for creating high and low conductance when PC and APC states are considered.

Since the CIP scheme is considered in the spin-valve structure, the electrodes were attached to the free-layer ferromagnetic layer, as shown in figure

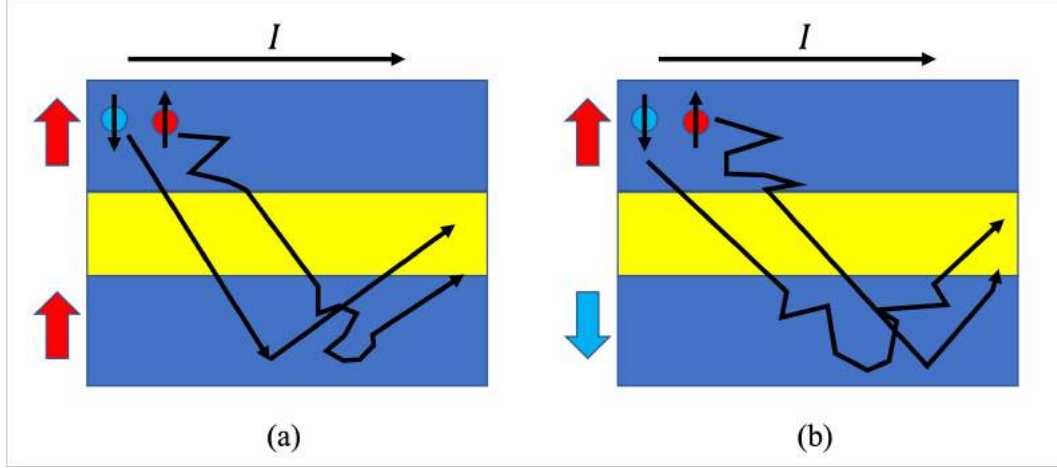


Figure 1.2: Two electronic states in spin-valve structure: (a) low resistance when PC state is considered and (b) high resistance when APC state is considered.

1.1(a). Fig. 1.2 shows that when the PC state is considered, the spin-up electrons (spin antiparallel to the magnetization) can travel through the sandwich nearly unscattered, providing a conductivity shortcut and low resistance. In contrast, in the APC state, both spin-up and spin-down electrons collide in either the upper or lower ferromagnetic layer, providing higher overall resistance.

On the other hand, in MTJ, the electrodes were placed on both the upper and lower ferromagnetic layers, creating a CPP scheme. Figure 1.3 shows that when the PC state is considered, a large number of electrons with minority (majority) spin from the lower ferromagnetic layer tunneling through the barrier are accepted by a large number of unfilled states of minority (majority) spin of the upper ferromagnetic layer. As a result, the conductance will be high. In the APC state, however, the identity of majority and minority spin is reversed, which causes only a few numbers of the majority spin electrons of the lower ferromagnetic layer tunnel to the upper ferromagnetic layer and be accepted by a large number of unfilled states of the minority spin, and vice versa.

The two different mechanisms of spin filtering in spin-valve and MTJ lead to different performance efficiencies, where MTJ has a higher magnetoresistance (MR) ratio than spin-valve. An example is the $\text{Co}_{10}\text{Cu}_{90}$ junction. At a temperature of 4.2 K, when the CIP geometry was considered, the highest MR ratio, as high as 80%, was observed by varying the thickness of Cu. In contrast, an MR ratio as high as 125% was observed when the CPP geometry was considered. When the temperature is increased to room temperature

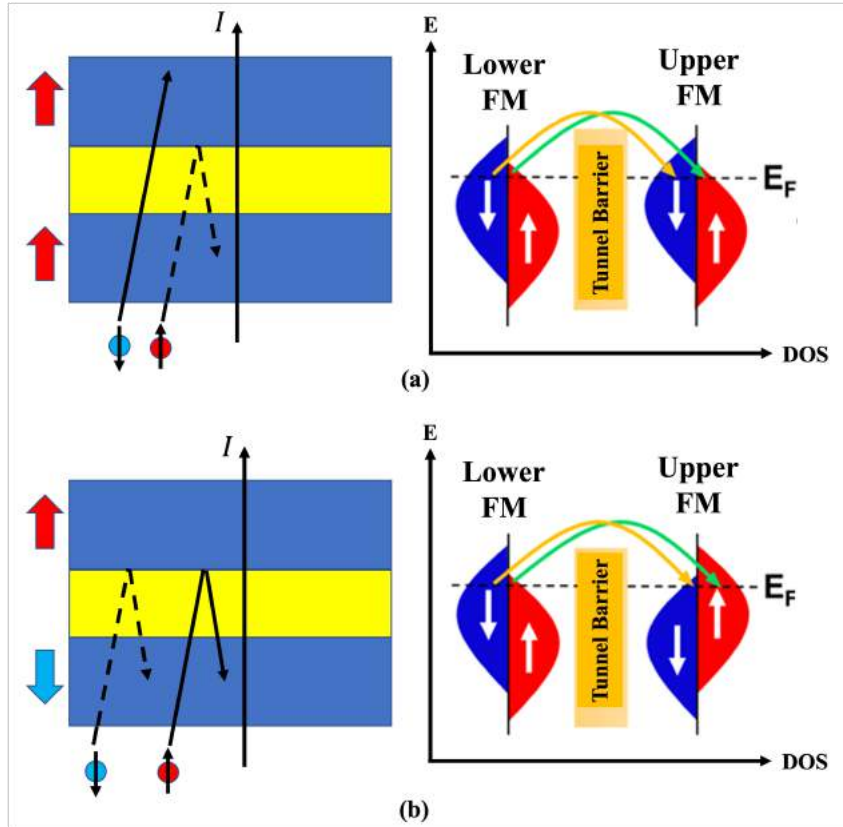


Figure 1.3: Two electronic states on magnetic tunnel junction structure: (a) low resistance when the PC state is considered and (b) high resistance when the APC state is considered.

(300 K), the MR ratios for the CIP and CPP geometries are 20% and 80%, respectively [12, 13].

1.1.2 The Development of Spintronics Devices

Due to its efficiency in achieving a high performance by having a high MR ratio, the MTJ device has been continuously studied. So far, the major competition for improvement the MTJ performance is to achieve a higher level of tunneling MR (TMR) ratio. Fully understanding the nature of the properties of this device is essential to enable successful design and application. A critical point that determines the performance of the MTJ is its tunnel barrier. As explained in the previous subsection, the TMR effect was initially discovered by Michel Jullière from the University of Rennes, France, in 1975. At that time, Ge-O was used as a tunnel barrier in Fe/Ge-O/Co-junctions. At a temperature of 4.2 K, the TMR ratio was approximately 14% [4]. The next important finding occurred in 1991 when Terunobu Miyazaki from Tohoku

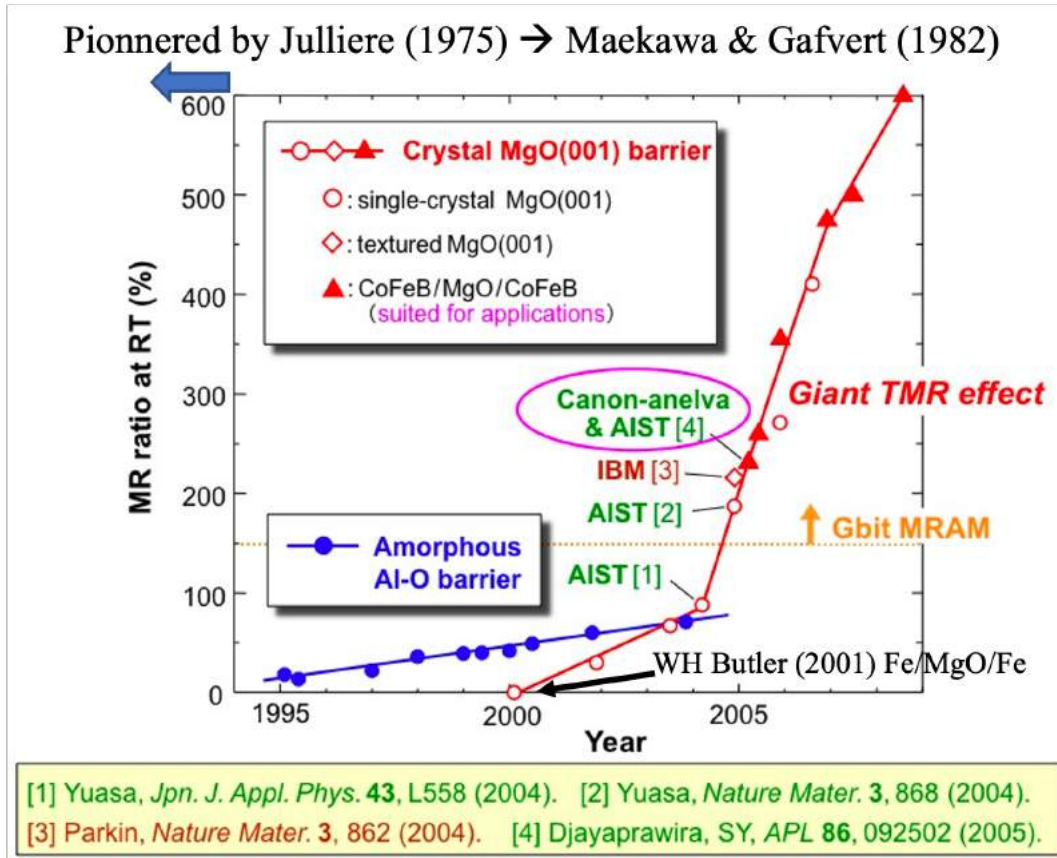


Figure 1.4: The development of MTJs. Taken from [21]

University, Japan, found a TMR ratio of 2.7% at room temperature. Later, in 1994, Miyazaki found a TMR ratio of 18% on Fe/Al₂O₃/Fe MTJ [14], and Jagadeesh Moodera found a TMR ratio of 11.8% when CoFe and Co electrodes replaced iron electrodes [15]. The highest effect observed with Al₂O₃ insulators were approximately 70% at 300K, as shown in Fig 1.4.

Due to the limit found on amorphous Al₂O₃ tunnel barriers, starting from 2000, tunnel barriers of crystalline magnesium oxide (MgO) were investigated. In 2001, Butler theoretically predicted that using iron as the ferromagnet and MgO as the insulator, the tunnel MR can reach several thousand percent [16]. The same year, Bowen et al. were the first to report experiments showing a significant TMR in an MgO-based MTJ by considering the Fe/MgO/FeCo(001) junction [17]. In 2004, Parkin and Yuasa made Fe/MgO/Fe junctions that reach over 200% TMR at room temperature [18,19]. In 2008, the effects of up to 604% at room temperature and more than 1100% at 4.2 K were observed in CoFeB/MgO/CoFeB MTJs by Ikeda and Ohno groups of Tohoku University in Japan [20]. The development of MTJs to achieve a high TMR ratio is summarized in Fig. 1.4.

1.1.3 2D Materials-based Spintronics Devices

A critical application of MJs is as a memory device. Thus, the density of MJs in a device becomes important because of its relation to the memory capacity of the device. Increasing the density of the MJ can be done by down-scaling its size. To downscale the device while retaining a high transmission, it is essential to reduce the barrier thickness. However, when this is realized, TMR can be reduced to 55% due to uncontrollable defects in the MgO tunnel barrier [22].

On the other hand, in the early 2000s, a one-atomic-thickness material called graphene was introduced. Graphene, a carbon-based 2D material with extraordinary in-plane charge mobility [23], has attracted interest as an ideal material for application in microelectronics [24, 25] and sensing [26]. Experimentally, graphene is synthesized by chemical vapor deposition and yields well-ordered *3m symmetry* on the substrate surface [27, 28]. Its interesting tunable transport properties and unique magnetic response, as well as its weak spin-orbit coupling and long spin scattering length [29], make graphene a prospective material for spintronics devices.

The low dimensionality of graphene was expected to solve the downscaling problem of MTJs. Recently, graphene has been examined for the nonmagnetic spacers in CPP MTJs. One example is Ni/graphene/Ni MTJ. Owing to its structure, which is similar to that of graphene (the smallest lattice mismatch), the Ni/graphene junction can be synthesized easily through various methods [30–40]. Further, the Ni/graphene/Ni MTJ successfully shows the change in the MR ratio due to an external magnetic field. However, a small TMR ratio was found [30–40]. Further investigation was conducted using hexagonal boron nitride (hBN), an insulating one-atomic-thickness material, but a satisfactory result has not been achieved yet [41–43]. The recent experimental development of graphene and hBN used as a tunnel barrier in MTJ is shown in Fig. 1.6.

On the other hand, a theoretical study was done to investigate Ni/*n*hBN/Ni magnetic junctions with *n* is the number of hBN layers [44]. The study suggests that the highest TMR ratio, as high as 60%, was reached when the number of hBN layers was two. Once the number of hBN layers increases, the TMR ratio is reduced significantly, as shown in Figure 1.5(a). Further investigation was done by inserting a graphene layer into the insulator barrier, creating Ni/hBN/*n*Gr/Ni with *n* as the graphene layer number. The calculation results show that the optimum TMR ratio as high as 100% was reached when five graphene layers were considered. When the number of the graphene

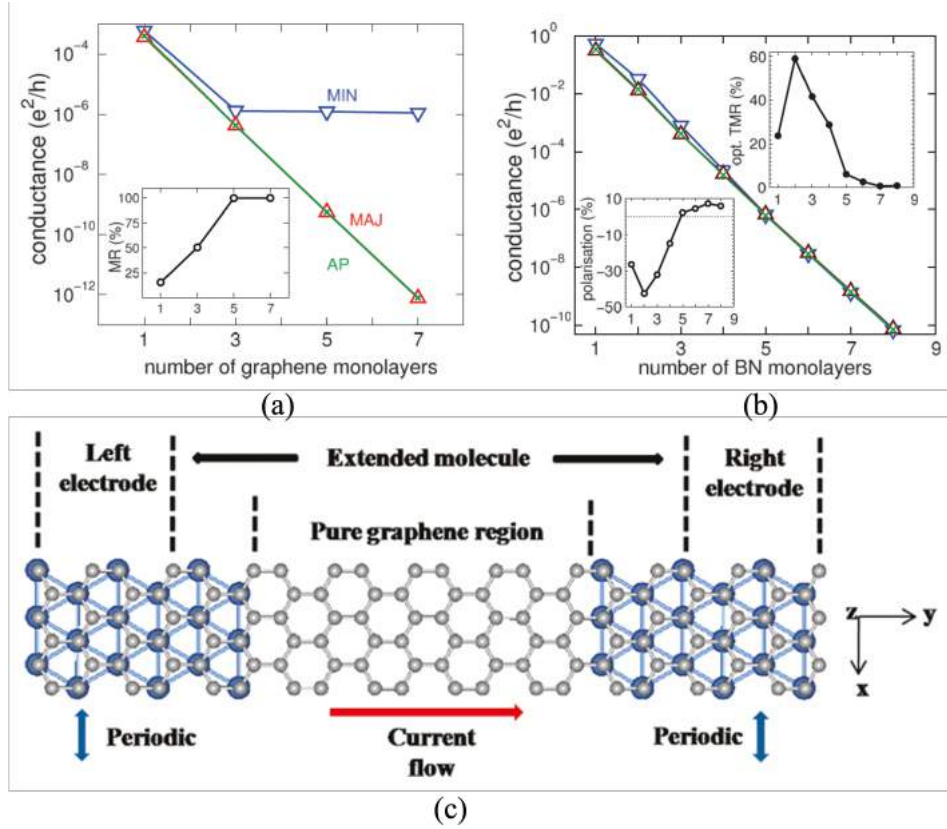


Figure 1.5: The calculated conductance and TMR ratio of (a) Ni/nhBN/Ni and (b) Ni/hBN/nGr/Ni (taken from [44]). The proposed spintronics device of graphene act as a bridge between two Ni electrodes (taken from [45]).

layer is increased further, the TMR ratio was kept at 100%, as shown in Figure 1.5(b). Another theoretical study introduced a new strategy to obtain high performance on 2D materials-based spintronic devices; graphene was used as a bridge between ferromagnetic materials to get optimum magnetoresistance ratio, as shown in Figure. The idea came from the fact that graphene has a long spin scattering length [29]. One the example is Ni/Gr—Gr—Gr/Ni device, which is shown in Figure 1.5(c). Nickel electrodes were used as ferromagnetic materials [45]. By injecting selective spin electrons from the left Ni electrode into graphene, which connects two ferromagnetic as a bridge, a spin valve device was expected to be created by interchanging the left and right electrodes to have APC and PC states. The results show that a maximum 110% magnetoresistance ratio was observed on the device. Those two theoretical studies above gave an insight into the unknown properties and strategies that have not been utilized to get the best performance of 2D materials-based spintronics devices.

From another perspective, the chemical and physical interactions between

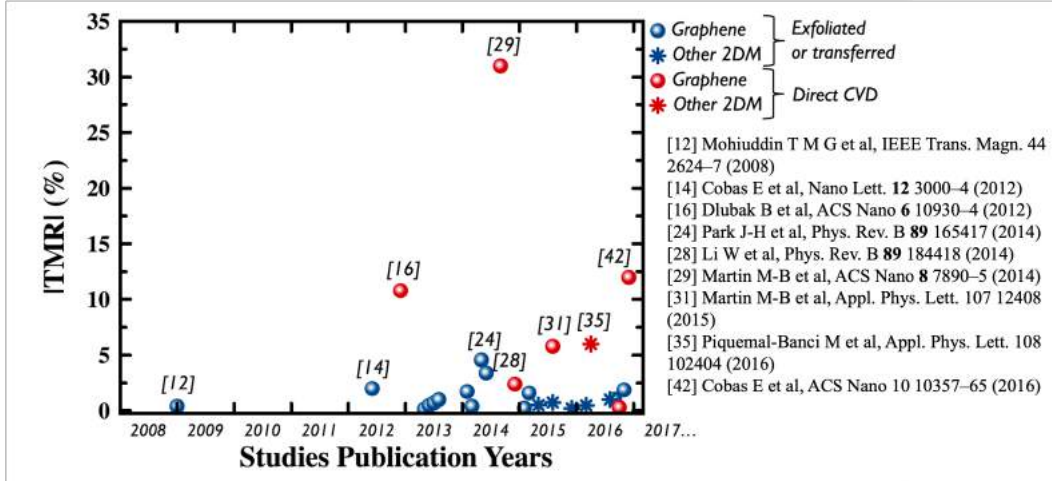


Figure 1.6: The development of 2D materials-based MTJs. Taken from [54]

graphene or hBN with the ferromagnetic layer are interesting and can be further developed. When graphene is grown on top of the transition metal, transport properties of graphene can be sensitively tuned [46,47]. Further, graphene gives a unique magnetic response by growing on top of the ferromagnetic material [46, 48–53]. Therefore, graphene was still expected to give a unique characteristic as MTJ and to have a new device mechanism that could not be found in the conventional one. However, a new strategy and further systematic investigation to unlock hidden properties in graphene-based MJs are necessary to successfully realize a spintronics device based on graphene.

1.2 Strategy and Aim

This thesis proposes an in-plane MR (IMR) scheme of graphene in a sandwich structure of monolayer graphene with ferromagnetic slabs, instead of considering the TMR scheme. In other words, instead of investigating the MR effect from CPP geometry, the CIP geometry of the MR effect was considered on graphene due to the magnetic alignment of the upper and lower ferromagnetic materials, i.e., APC and PC. The Ni(111) slab was considered to sandwich graphene, owing to its structure, which is similar to that of graphene (having small lattice mismatch). In chapter 3, it will be explained in detail that the consideration of investigating the IMR properties of a graphene-based spin-valve has something to do with the controllability of the spin-dependent Dirac cone of graphene.

This study aims to propose a successful design of a graphene-based spin-valve as a spintronic device having a high MR ratio. To achieve the aim of the

study, the study stages have been proposed:

1. In the first stage, an investigation was considered to explore graphene's magnetic properties and electronic structure in the Ni/graphene/Ni spin-valve structure. The study emphasized graphene's induced magnetic moment properties and Dirac cone characteristics due to its response to the upper and lower Ni slabs' antiparallel or parallel magnetic configuration. A density functional theory (DFT) spin-polarized generalized-gradient approximation (spin-GGA) calculation was done. A band structure calculation and spin-charge density mapping were done to show the indication of graphene in-plane conductivity change by observing the change in the Dirac cone characteristic.
2. In the second stage, since the controllable mass-gapped Dirac cone (MGDC) of graphene was found on the Ni/graphene/Ni spin-valve structure (explained in chapter 4), further investigation was conducted to understand the effectiveness of MGDC in creating a high MR ratio. For that purpose, first-principles quantum transport calculations, which coupled DFT with the nonequilibrium Green's function, were performed.
3. After that, in the final stage, optimization to create a successful design of a graphene-based spin-valve structure spintronics device was performed. The optimization was needed for realization of the actual device and for ensuring a performance comparable to that predicted in this theoretical study. The chemical bonding between the Ni slabs and graphene in Ni/graphene/Ni needs to be perfect to get control on graphene's MGDC. This perfect surface can be realized experimentally; however, it is relatively difficult. Thus, to avoid a complete change in the IMR of graphene due to a defect at the Ni/graphene interface, a barrier is necessary to maintain the graphene Dirac cone, although some defect occurs on the Ni surface. Furthermore, by introducing the barrier between Ni slabs and graphene, an easier controllability of graphene's Fermi energy will be expected. In this thesis hBN layer is introduced as a barrier between Ni slabs and graphene. In this stage, an investigation was conducted to understand whether graphene's MGDC is still controllable after the barrier was introduced.

All the results provided a key leading aspect for realizing a successful graphene-based spin-valve device.

1.3 Thesis Organization

This thesis consists of nine chapters. Chapter 1 introduces MJs, graphene-based MJs, and the proposed strategy to achieve high-performance graphene-based spintronics devices. Chapter 2 introduces the literature review on the theory behind the atomistic modeling techniques, conductance simulation, and the Dirac cone of graphene. Chapter 3 presents the theoretical framework of our consideration design and the computational approach strategy in the simulation. The results and discussions presented in chapters 4-7 in this thesis are an integration of published studies (Chapters 4-6) [55–57] and those under review (Chapters 7) in international journals. The details of each chapter are as follows:

- In chapter 4, Ni(111)/graphene/Ni(111) MJ investigation is proposed through DFT spin-GGA calculations. From the calculation, it was predicted that in the Ni(111)/graphene/Ni(111) system, the MGDC of graphene could be controlled using the magnetic alignment of the Ni slabs. When the magnetic moments of the upper and lower Ni(111) slabs have an APC state, the MGDC is open. However, when the magnetic moments of the upper and lower Ni(111) slabs have a PC state, the MGDC is closed. This characteristic implies that the pseudospin between sublattices A and B can be controlled to preserve or break the chiral symmetry, making the MGDC controllable. This chapter discusses the origin of the controllable chiral symmetry perseverance of graphene due to Ni slabs' magnetic alignment in detail.
- In chapter 5, a theoretical study is presented on the in-plane conductance of graphene partially sandwiched between Ni(111) nanostructures with a width of 12.08 Å. The investigation of the proposed system is conducted to understand the effectiveness of a controllable MGDC of graphene, which was explained in the previous chapter, on its in-plane conductance to realize a high MR ratio. First-principles quantum transport calculations, which coupled DFT with the nonequilibrium Green's function, were performed. The results predicted that a colossal MR ratio beyond 3100% was expected when the width of the Ni(111) nanostructures was at the nanometer scale.
- In chapter 6, a theoretical study is conducted to understand the origin of the magnetic proximity effect in Ni/*nh*BN/Ni MTJs, which is the

main contribution to the CPP tunneling conductance of the MTJ. First, a study on Ni/2hBN/Ni MJs showed that the Ni's surface state (111) becomes the main contribution to the tunneling transmission of the electrons when electrons flow from one Ni slab to another through two hBN layers. When the number of hBNs is increased to three, the Ni(111) slabs' surface state still survives, resulting in a magnetic proximity effect on the middle hBN. However, the magnetic proximity effect on the middle hBN is weak since the d_z -orbital of the Ni(111) surface state works on the unfilled p_z -orbital of B atoms. However, when the middle hBN is replaced with graphene, creating an Ni/hBN-graphene-hBN/Ni junction, the d_z -orbital of the Ni(111) surface state works significantly on the graphene layer, since it works on the π -orbital of graphene. The role of the proximity effect in controlling the MGDC of graphene is discussed in the next chapter.

- In chapter 7, a study is performed on the role of the Ni/hBN slab-graphene interface of the Ni/hBN-graphene-hBN/Ni MJ in controlling the MGDC of graphene via the magnetic proximity effect. The spin-polarized DFT calculation was performed on 12 possible stacking configurations for the APC and PC of Ni slabs' magnetic alignment. The 12 stacking configurations can be categorized into three groups based on the relative total energy, corresponding to van der Waals' interaction between hBN and graphene. In group I, the magnetic proximity effect of B atoms on graphene causes the opening and closing of MGDC with a small gap size when N atoms are placed on top or below the hollow site of graphene. In group II, when the proximity effect of the Ni(111) surface state as an evanescent wave acts on C atoms, both the APC and PC states have a spin channel with a prominent size of mass-gapped, whereas the other does not. In group III, the MGDC is open with a significant gap size in the APC state and close in the PC state, when the asymmetric arrangement of N atoms on different sublattices of graphene is considered. The unique characteristics of graphene's MGDC control, depending on the stacking configuration, can be proposed as a device where a controllable MGDC is tuned using mechanical motion. A spin-mechatronics device can be realized by proposing a device that can move the upper and lower Ni(111)/hBN slabs translationally.

Finally, the thesis summary is presented in chapter 8.

This page intentionally left blank

Chapter 2

Theoretical Basis

2.1 Review on Many-Body Schrödinger Equation

2.1.1 Many-Body Schrödinger Equation

In this section, improvement of the quantum theory from a single-particle description in the external potential to the quantum many-body theory for materials is introduced. From the basic quantum theory, the quantum mechanical wavefunction contains all the information of a given system, and that information can be obtained by solving a Schrödinger equation. The time-independent Schrödinger equation can be expressed as follows:

$$(\hat{T} + \hat{V})\psi = E\psi \quad (2.1)$$

where \hat{T} , \hat{V} , and E are kinetic energy, potential energy, and total energy of the given system, respectively.

The realistic and useful theory of materials is developed by describing systems with many electrons and nuclei. The *many-body* wavefunction needs to be introduced, which depends on the positions of each nucleus and electrons in the system. The wavefunction of the system which has N electrons with coordinates $\mathbf{r}_1, \mathbf{r}_2, \dots, \mathbf{r}_N$ and M nuclei with coordinates $\mathbf{R}_1, \mathbf{R}_2, \dots, \mathbf{R}_M$ can be expressed as follows:

$$\Psi = \Psi(\mathbf{r}_1, \mathbf{r}_2, \dots, \mathbf{r}_N; \mathbf{R}_1, \mathbf{R}_2, \dots, \mathbf{R}_M). \quad (2.2)$$

By using the many-body wavefunction, the single-particle Schrödinger equation at eq.2.1 can be transformed to the many-body Schrödinger , which is

written as follows:

$$\hat{H}\Psi(\mathbf{r}_1, \mathbf{r}_2, \dots, \mathbf{r}_N; \mathbf{R}_1, \mathbf{R}_2, \dots, \mathbf{R}_M) = E\Psi(\mathbf{r}_1, \mathbf{r}_2, \dots, \mathbf{r}_N; \mathbf{R}_1, \mathbf{R}_2, \dots, \mathbf{R}_M) \quad (2.3)$$

where \hat{H} is Hamiltonian that consists of kinetic and potential energies.

In many applications, the total electronic charge density, which means the probability of finding any electron at position \mathbf{r} , becomes the interest. The electron density, $n(\mathbf{r})$, is expressed as follows:

$$n(\mathbf{r}) = N \int |\Psi(\mathbf{r}, \mathbf{r}_2, \dots, \mathbf{r}_N; \mathbf{R}_1, \dots, \mathbf{R}_M)|^2 d\mathbf{r}_2 \dots d\mathbf{r}_N d\mathbf{R}_1 \dots d\mathbf{R}_M, \quad (2.4)$$

and if the many-body wavefunction is normalized into unity within the system, it gives

$$\int |\Psi(\mathbf{r}, \mathbf{r}_2, \dots, \mathbf{r}_N; \mathbf{R}_1, \dots, \mathbf{R}_M)|^2 d\mathbf{r}_2 \dots d\mathbf{r}_N d\mathbf{R}_1 \dots d\mathbf{R}_M = 1. \quad (2.5)$$

The combination of eq.2.4 and eq.2.5 leads to the fact that the integral of the electronic charge density throughout the whole system yields the number of electrons. It is mathematically written as follows:

$$\int n(\mathbf{r}) d\mathbf{r} = N. \quad (2.6)$$

The many-body wavefunction and the many-body Schrödinger equation have been introduced. Now, let us move on to the Hamiltonian of materials. At first, let us consider the kinetic energy of materials. Similar to the previous discussion, we consider N electrons and M nuclei. Thus, we should write down the kinetic energy for all electrons and all nuclei as follows:

$$\hat{T} = - \sum_{i=1}^N \frac{\hbar^2}{2m_e} \nabla_i^2 - \sum_{I=1}^M \frac{\hbar^2}{2M_I} \nabla_I^2 \quad (2.7)$$

where M_1, M_2, \dots are the masses of the nuclei, and m_e is the mass of an electron. Next, we need to consider the potential energy of materials. The potential energy of materials consists of three terms, namely, potential energy from Coulomb repulsion between electrons, Coulomb repulsion between two nuclei, and Coulomb attraction between an electron and a nucleus. Each of

the terms could be written as follows:

$$\hat{V}_{ee} = \frac{1}{2} \sum_{i \neq j} \frac{e^2}{4\pi\epsilon_0} \frac{1}{|\mathbf{r}_i - \mathbf{r}_j|}, \quad (2.8)$$

$$\hat{V}_{nn} = \frac{1}{2} \sum_{I \neq J} \frac{e^2}{4\pi\epsilon_0} \frac{Z_I Z_J}{|\mathbf{R}_I - \mathbf{R}_J|}, \quad (2.9)$$

$$\hat{V}_{en} = - \sum_{i,I} \frac{e^2}{4\pi\epsilon_0} \frac{Z_I}{|\mathbf{r}_i - \mathbf{R}_I|}, \quad (2.10)$$

where \hat{V}_{ee} , \hat{V}_{nn} , and \hat{V}_{en} are potential energy of electron–electron, nuclei–nuclei, and electron–nuclei interactions, respectively. Z_I and Z_J denote the atomic numbers; e , the electron charge; and ϵ_0 , the permittivity of vacuum. Finally, by substituting the Hamiltonian of materials into many-body Schrödinger equation, the Schrödinger equation for materials is given as follows:

$$\left[- \sum_{i=1}^N \frac{\hbar^2}{2m_e} \nabla_i^2 - \sum_{I=1}^N \frac{\hbar^2}{2M_I} \nabla_I^2 + \frac{1}{2} \sum_{i \neq j} \frac{e^2}{4\pi\epsilon_0} \frac{1}{|\mathbf{r}_i - \mathbf{r}_j|} + \frac{1}{2} \sum_{I \neq J} \frac{e^2}{4\pi\epsilon_0} \frac{Z_I Z_J}{|\mathbf{R}_I - \mathbf{R}_J|} - \sum_{i,I} \frac{e^2}{4\pi\epsilon_0} \frac{Z_I}{|\mathbf{r}_i - \mathbf{R}_I|} \right] \Psi = E_{tot} \Psi \quad (2.11)$$

By converting the units into Hartree atomic units ($\hbar = m_e = e = 1$), the many-body Schrödinger equation for materials acquires the following elegant form:

$$\left[- \sum_i^N \frac{\nabla_i^2}{2} - \sum_I^N \frac{\nabla_I^2}{2M_I} - \sum_{i,I} \frac{Z_I}{|\mathbf{r}_i - \mathbf{R}_I|} + \frac{1}{2} \sum_{i \neq j} \frac{1}{|\mathbf{r}_i - \mathbf{r}_j|} + \frac{1}{2} \sum_{I \neq J} \frac{Z_I Z_J}{|\mathbf{R}_I - \mathbf{R}_J|} \right] \Psi = E_{tot} \Psi. \quad (2.12)$$

Eq.2.12 is too general because it describes almost everything, and it is too complex to be solved analytically, except for some simple cases like hydrogen-like atoms. At this stage, it is necessary to adopt a good approximation method to the Hamiltonian and the many-body wavefunction, so that the equation can be solved within a reasonable time and a computational cost while keeping the important and correct physics.

The forces on both the electrons and ions are of the same order of mag-

nitude; their momenta are also comparable. However, since the ions are so massive compared with the electrons, the kinetic energy of the ions is much smaller than that of the electrons. Therefore, we can consider $M_I = \infty$ in eq.2.12. This consideration implies the negligence of the kinetic energy of the nuclei in eq.2.12, whereas the Coulomb repulsion between nuclei is simply constant. This idea forms the basis of the Born–Oppenheimer approximation [58].

Now, let us apply the Born–Oppenheimer approximation to eq.2.12. First, for the convenience, we separate a constant from the Coulomb repulsion between nuclei from the expression by defining

$$E = E_{tot} - \frac{1}{2} \sum_{I \neq J} \frac{Z_I Z_J}{|\mathbf{R}_I - \mathbf{R}_J|}. \quad (2.13)$$

By using this definition and omitting the kinetic energy of the nuclei, it allows us to rewrite eq.2.12 as follows:

$$\left[- \sum_i^N \frac{\nabla_i^2}{2} - \sum_{i,I} \frac{Z_I}{|\mathbf{r}_i - \mathbf{R}_I|} + \frac{1}{2} \sum_{i \neq j} \frac{1}{|\mathbf{r}_i - \mathbf{r}_j|} \right] \Psi = E_{tot} \Psi. \quad (2.14)$$

where the nuclear coordinates, \mathbf{R}_I can be regarded as external parameters. Thus, we can consider the wavefunction, Ψ , only as a function of the electron coordinates, if we substitute into eq.2.14 the following definition:

$$V_n(\mathbf{r}) = - \sum_I \frac{Z_I}{|\mathbf{r} - \mathbf{R}_I|} \quad (2.15)$$

which indicates the Coulomb potential of the nuclei experienced by the electrons. By using the definition, eq.2.14 can be written as follows:

$$\left[- \sum_i^N \frac{\nabla_i^2}{2} - \sum_i V_n(\mathbf{r}_i) + \frac{1}{2} \sum_{i \neq j} \frac{1}{|\mathbf{r}_i - \mathbf{r}_j|} \right] \Psi = E_{tot} \Psi. \quad (2.16)$$

This equation is the fundamental equation of the *electronic structure theory*. In the next sections, we will discuss the techniques to solve this Schrödinger equation.

2.1.2 Slater Determinant

The identical particles, *i.e.* particles characterized by the same quantum numbers such as mass, charge, and spin, are in principle indistinguishable.

Before going into further to solve eq.2.16, we should consider the fact that electrons are indistinguishable particles. If we suppose that two coordinates in an N -particle wavefunction are interchanged, it yields the same physical state, and the corresponding wavefunction will be different from the original one only by a simple prefactor λ . Using this procedure twice, we have an equality,

$$\begin{aligned}\Psi(\mathbf{r}_1, \dots, \mathbf{r}_j, \dots, \mathbf{r}_k, \dots, \mathbf{r}_N) &= \lambda \Psi(\mathbf{r}_1, \dots, \mathbf{r}_k, \dots, \mathbf{r}_j, \dots, \mathbf{r}_N) \\ &= \lambda^2 \Psi(\mathbf{r}_1, \dots, \mathbf{r}_j, \dots, \mathbf{r}_k, \dots, \mathbf{r}_N).\end{aligned}\quad (2.17)$$

Because electrons are fermions, it means that they need to fulfill the Pauli exclusion principle, where the many body-body wavefunction, Ψ , must change the sign if the variable of any two electrons is changed. Therefore, the prefactor λ for the fermion case is $\lambda = -1$ for fermions, which yields

$$\Psi(\mathbf{r}_1, \dots, \mathbf{r}_j, \dots, \mathbf{r}_k, \dots, \mathbf{r}_N) = -\Psi(\mathbf{r}_1, \dots, \mathbf{r}_k, \dots, \mathbf{r}_j, \dots, \mathbf{r}_N).\quad (2.18)$$

Now, we want to change our expression of the N -particle wavefunction $\Psi(\mathbf{r}_1, \mathbf{r}_2, \dots, \mathbf{r}_N)$ into a linear superposition of product states containing N factors of single-particle basis states. First, from an arbitrary N -particle state $\Psi(\mathbf{r}_1, \mathbf{r}_2, \dots, \mathbf{r}_N)$, we form the $(N - 1)$ -particle function $A_{\nu_1}(\mathbf{r}_2, \dots, \mathbf{r}_N)$ by projecting it onto the basis state $\psi_{\nu_1}(\mathbf{r}_1)$

$$A_{\nu_1}(\mathbf{r}_2, \dots, \mathbf{r}_N) \equiv \int d\mathbf{r}_1 \psi_{\nu_1}^*(\mathbf{r}_1) \Psi(\mathbf{r}_1, \mathbf{r}_2, \dots, \mathbf{r}_N)\quad (2.19)$$

Then, it can be inverted by multiplying with $\psi_{\nu_1}(\tilde{\mathbf{r}}_1)$ and summing over ν_1 ,

$$\begin{aligned}\sum_{\nu_1} \psi_{\nu_1}(\tilde{\mathbf{r}}_1) A_{\nu_1}(\mathbf{r}_2, \dots, \mathbf{r}_N) &= \sum_{\nu_1} \psi_{\nu_1}(\tilde{\mathbf{r}}_1) \int d\mathbf{r}_1 \psi_{\nu_1}^*(\mathbf{r}_1) \Psi(\mathbf{r}_1, \mathbf{r}_2, \dots, \mathbf{r}_N) \\ &= \int d\mathbf{r}_1 \left[\sum_{\nu_1} \psi_{\nu_1}^*(\mathbf{r}_1) \psi_{\nu_1}(\tilde{\mathbf{r}}_1) \right] \Psi(\mathbf{r}_1, \mathbf{r}_2, \dots, \mathbf{r}_N) \\ &= \int d\mathbf{r}_1 \delta(\tilde{\mathbf{r}}_1 - \mathbf{r}_1) \Psi(\mathbf{r}_1, \mathbf{r}_2, \dots, \mathbf{r}_N) \\ &= \Psi(\tilde{\mathbf{r}}_1, \mathbf{r}_2, \dots, \mathbf{r}_N) \\ \Psi(\tilde{\mathbf{r}}_1, \mathbf{r}_2, \dots, \mathbf{r}_N) &= \sum_{\nu_1} \psi_{\nu_1}(\tilde{\mathbf{r}}_1) A_{\nu_1}(\mathbf{r}_2, \dots, \mathbf{r}_N)\end{aligned}\quad (2.20)$$

Now, we analogously define $A_{\nu_1, \nu_2}(\mathbf{r}_3, \dots, \mathbf{r}_N)$ from $A_{\nu_1}(\mathbf{r}_2, \dots, \mathbf{r}_N)$:

$$A_{\nu_1, \nu_2}(\mathbf{r}_3, \dots, \mathbf{r}_N) \equiv \int d\mathbf{r}_2 \psi_{\nu_2}^*(\mathbf{r}_2) A_{\nu_1}(\mathbf{r}_2, \dots, \mathbf{r}_N). \quad (2.21)$$

and by doing so, it will lead to

$$\Psi(\tilde{\mathbf{r}}_1, \tilde{\mathbf{r}}_2, \mathbf{r}_3, \dots, \mathbf{r}_N) = \sum_{\nu_1, \nu_2} \psi_{\nu_1}(\tilde{\mathbf{r}}_1) \psi_{\nu_2}(\tilde{\mathbf{r}}_2) A_{\nu_1, \nu_2}(\mathbf{r}_3, \dots, \mathbf{r}_N) \quad (2.22)$$

We can continue all the way through $\tilde{\mathbf{r}}_N$ (and then writing \mathbf{r} instead of $\tilde{\mathbf{r}}$. Finally, we end up with

$$\Psi(\mathbf{r}_1, \mathbf{r}_2, \dots, \mathbf{r}_N) = \sum_{\nu_1, \dots, \nu_N} A_{\nu_1, \nu_2, \dots, \nu_N} \psi_{\nu_1}(\mathbf{r}_1) \psi_{\nu_2}(\mathbf{r}_2) \dots \psi_{\nu_N}(\mathbf{r}_N) \quad (2.23)$$

where $A_{\nu_1, \nu_2, \dots, \nu_N}$ is just a complex number. However, from our discussion on indistinguishable particle of fermions, the aforementioned product is not a physically useful basis because the coordinates have to appear anti-symmetrically. Then, to solve the problem, the fermionic anti-symmetrization operator \hat{S}_- is introduced to the product state and defined by the following determinants:

$$\begin{aligned} & \hat{S}_- \psi_{\nu_1}(\mathbf{r}_1) \psi_{\nu_2}(\mathbf{r}_2) \dots \psi_{\nu_N}(\mathbf{r}_N) \\ &= \begin{vmatrix} \psi_{\nu_1}(\mathbf{r}_1) & \psi_{\nu_1}(\mathbf{r}_2) & \dots & \psi_{\nu_1}(\mathbf{r}_N) \\ \psi_{\nu_2}(\mathbf{r}_1) & \psi_{\nu_2}(\mathbf{r}_2) & \dots & \psi_{\nu_2}(\mathbf{r}_N) \\ \vdots & \vdots & \ddots & \vdots \\ \psi_{\nu_N}(\mathbf{r}_1) & \psi_{\nu_N}(\mathbf{r}_2) & \dots & \psi_{\nu_N}(\mathbf{r}_N) \end{vmatrix}_- = \sum_{p \in S_N} \left(\prod_{j=1}^N \psi_{\nu_j}(\mathbf{r}_{p(j)}) \right) \text{sign}(p) \end{aligned} \quad (2.24)$$

which in physics are denoted as Slater determinants. Then, by using the symmetrized basis states gets, $\psi(\mathbf{r}_1, \mathbf{r}_2, \dots, \mathbf{r}_N)$ is replaced by the following equation

$$\Psi(\mathbf{r}_1, \mathbf{r}_2, \dots, \mathbf{r}_N) = \sum_{\nu_1, \dots, \nu_N} B_{\nu_1, \nu_2, \dots, \nu_N} \hat{S}_- \psi_{\nu_1}(\mathbf{r}_1) \psi_{\nu_2}(\mathbf{r}_2) \dots \psi_{\nu_N}(\mathbf{r}_N) \quad (2.25)$$

2.1.3 Mean-Field Approximation

We understand that each many-body wavefunction is expanded in a series of Slater determinants. We also need to simplify our Hamiltonian in eq.2.16, because the Schrödinger equation in eq.2.16 is still too complex, which needs high computational cost to be solved in the exact manner. At first, we need to make an approximation so that the problem becomes much simpler without omitting any important physics. The Coulomb interaction term between electrons is the most time-consuming and needs high computational cost for the calculation. Approximation is performed to reduce the complexity of the calculation. The Coulomb interaction between electrons cannot be neglected because it is in the same order with the other terms. However, we can instead maintain a single-particle description and take the Coulomb repulsion into account in an approximate form. This approximation is so-called mean-field approximation.

Let us consider a distribution of electronic charge, $n(\mathbf{r})$, in classical electrostatic point of view as

$$n(\mathbf{r}) = \sum_i |\phi_i|^2 \quad (2.26)$$

which generates an electric potential $\varphi(\mathbf{r})$ through Poisson's equation:

$$\nabla^2 \varphi(\mathbf{r}) = 4\pi n(\mathbf{r}). \quad (2.27)$$

The potential energy of electron, which is immersed in this electric potential, is $V_H(\mathbf{r}) = -\varphi(\mathbf{r})$, which is the well-known Hartree potential. The Hartree potential satisfies Poisson's equation as follows:

$$\nabla^2 V_H(\mathbf{r}) = 4\pi n(\mathbf{r}). \quad (2.28)$$

The formal solution of this equation is

$$V_H(\mathbf{r}) = \int d\mathbf{r}' \frac{n(\mathbf{r}')}{|\mathbf{r} - \mathbf{r}'|}, \quad (2.29)$$

which means that each element of volume $d\mathbf{r}'$ has a charge $dQ = -n(\mathbf{r}')d\mathbf{r}'$. This charge generates a Coulomb potential at point \mathbf{r} given by $dQ/|\mathbf{r} - \mathbf{r}'|$.

Thus, the fundamental equation of the electronic structure theory, which is shown in eq.2.16, can be simplified by taking the Hartree potential into account as

$$\left[-\sum_i^N \frac{\nabla_i^2}{2} - \sum_i V_n(\mathbf{r}_i) + V_H(\mathbf{r}) \right] \Psi = E_{tot} \Psi. \quad (2.30)$$

This kind of approach, which simplifies the Coulomb repulsion so that the single-particle description is still maintained, is a kind of mean-field approximation. It needs to be noted that eq.2.30, eq.2.28, and eq.2.26 must be solved simultaneously by using the self-consistent field method, which was introduced by Hartree in 1928.

2.1.4 Hartree–Fock Equations

In the mean-field approximation, because electrons are assumed not to interact via the Coulomb repulsion, the many-body wavefunction is written as a Slater determinant, and the single-particle wavefunctions can be obtained by solving a simpler single-particle Schrödinger equation, which is presented in eq.2.30. Now, let us consider the fact that electrons do interact indeed. However, this interaction is not too strong; thus, the solution can still be written in a Slater determinant form.

We start from deriving the solution of the case of two electrons to keep formalism as simple as possible. The Schrödinger equation for the two-electron system is given by

$$\left[H_0(\mathbf{r}_1) + H_0(\mathbf{r}_2) + \frac{1}{|\mathbf{r}_1 - \mathbf{r}_2|} \right] \Psi = E \Psi, \quad (2.31)$$

where

$$H_0(\mathbf{r}) = -\frac{1}{2} \nabla^2 + V_n(\mathbf{r}), \quad (2.32)$$

while the Slater determinant for the two-electron system is given by

$$\Psi(\mathbf{r}_1, \mathbf{r}_2) = \frac{1}{\sqrt{2}} \left[\psi_1(\mathbf{r}_1) \psi_2(\mathbf{r}_2) - \psi_1(\mathbf{r}_2) \psi_2(\mathbf{r}_1) \right] \quad (2.33)$$

where we need to determine ψ_1 and ψ_2 , so that eq.2.33 is the solution of eq.2.31 with the lowest energy, E_0 . At first, to find ψ_1 and ψ_2 , which minimize the total energy, we write E as an explicit functional of the wavefunctions as follows:

$$\begin{aligned}
E &= \int d\mathbf{r}_1 d\mathbf{r}_2 \Psi^* \left[H_0(\mathbf{r}_1) + H_0(\mathbf{r}_2) + \frac{1}{|\mathbf{r} - \mathbf{r}'|} \right] \Psi \\
E &= \int d\mathbf{r}_1 d\mathbf{r}_2 \Psi^* H_0(\mathbf{r}_1) \Psi + \int d\mathbf{r}_1 d\mathbf{r}_2 \Psi^* H_0(\mathbf{r}_2) \Psi + \int d\mathbf{r}_1 d\mathbf{r}_2 \Psi^* \frac{1}{|\mathbf{r}_1 - \mathbf{r}_2|} \Psi \\
&= \langle \psi_1 | H_0 | \psi_1 \rangle \langle \psi_2 | \psi_2 \rangle + \langle \psi_2 | H_0 | \psi_2 \rangle \langle \psi_1 | \psi_1 \rangle - \langle \psi_1 | H_0 | \psi_2 \rangle \langle \psi_2 | \psi_1 \rangle \\
&\quad - \langle \psi_2 | H_0 | \psi_1 \rangle \langle \psi_1 | \psi_2 \rangle + \int d\mathbf{r}_1 d\mathbf{r}_2 \frac{|\psi_1(\mathbf{r}_1)|^2 |\psi_2(\mathbf{r}_2)|^2}{|\mathbf{r}_1 - \mathbf{r}_2|} \\
&\quad - \int d\mathbf{r}_1 d\mathbf{r}_2 \frac{\psi_1^*(\mathbf{r}_1) \psi_2^*(\mathbf{r}_2) \psi_1(\mathbf{r}_2) \psi_2(\mathbf{r}_1)}{|\mathbf{r}_1 - \mathbf{r}_2|}.
\end{aligned} \tag{2.34}$$

Eq.2.34 can be simplified, if the functions $\psi_1(\mathbf{r})$ and $\psi_2(\mathbf{r})$ are required to be orthonormal, which corresponds to the following conditions:

$$\langle \psi_1 | \psi_1 \rangle = \langle \psi_2 | \psi_2 \rangle = 1, \text{ and } \langle \psi_1 | \psi_2 \rangle = \langle \psi_2 | \psi_1 \rangle = 0. \tag{2.35}$$

These conditions make sure that the trial function is nicely normalized. By substituting eq.2.35 into eq.2.34, we have energy E as a functional of ψ_1 and ψ_2 , $E = E[\psi_1, \psi_2]$ as follows:

$$\begin{aligned}
E[\psi_1, \psi_2] &= \int d\mathbf{r} \psi_1^*(\mathbf{r}) H_0(\mathbf{r}) \psi_1(\mathbf{r}) + \int d\mathbf{r} \psi_2^*(\mathbf{r}) H_0(\mathbf{r}) \psi_2(\mathbf{r}) \\
&\quad + \int d\mathbf{r}_1 d\mathbf{r}_2 \frac{\psi_1^*(\mathbf{r}_1) \psi_2^*(\mathbf{r}_2) \psi_1(\mathbf{r}_1) \psi_2(\mathbf{r}_2)}{|\mathbf{r}_1 - \mathbf{r}_2|} \\
&\quad - \int d\mathbf{r}_1 d\mathbf{r}_2 \frac{\psi_1^*(\mathbf{r}_1) \psi_2^*(\mathbf{r}_2) \psi_1(\mathbf{r}_2) \psi_2(\mathbf{r}_1)}{|\mathbf{r}_1 - \mathbf{r}_2|}.
\end{aligned} \tag{2.36}$$

The functions ψ_1 and ψ_2 , which minimize this functional, can be obtained by requiring that the functional derivative of E with respect to ψ_1 (or ψ_2) be equal to zero:

$$\frac{\delta E}{\delta \psi_1} = 0, \quad \frac{\delta E}{\delta \psi_2} = 0. \tag{2.37}$$

The minimization process requires that the functions need to satisfy the constraints in eq.2.35; thus, the Lagrange multipliers method is used to effectively deal with the constraints. First, we introduce a new functional, which incorporates the constraints:

$$L[\psi_1, \psi_2, \lambda_{11}, \dots, \lambda_{22}] = E[\psi_1, \psi_2] - \sum_{ij} \lambda_{ij} [\langle \psi_1 | \psi_j \rangle - \delta_{ij}], \quad (2.38)$$

where the constants λ_{ij} are called *Lagrange multipliers*. In Lagrange's method, the *constrained minimization* problem defined in eq.2.35 and eq.2.37 is replaced by *unconstrained minimization* problem as follows:

$$\frac{\delta L}{\delta \psi_i} = 0, \quad i = 1, 2, \quad \frac{\delta L}{\delta \lambda_{ij}} = 0, \quad i, j = 1, 2. \quad (2.39)$$

Before performing the derivation, there is a remark that needs to be considered to make the derivation simpler. The derivatives with respect to ψ_i and ψ_i^* are not independent; however, it can effectively be treated like that. This crafty point is related to the fact that the Hamiltonian is Hermitian. Therefore, for the sake of convenience, instead of evaluating the derivatives with respect to ψ_i , the derivatives with respect to ψ_i^* is used. Thus, the functional derivatives of eq.2.38 can be obtained as follows:

$$\begin{aligned} \frac{\delta L}{\delta \psi_1^*} &= H_0(\mathbf{r})\psi_1(\mathbf{r}) + \int d\mathbf{r}' \frac{|\psi_2(\mathbf{r}')|^2}{|\mathbf{r} - \mathbf{r}'|} \psi_1(\mathbf{r}) \\ &\quad - \int d\mathbf{r}' \frac{\psi_2^*(\mathbf{r}')\psi_2(\mathbf{r}')}{|\mathbf{r} - \mathbf{r}'|} \psi_1(\mathbf{r}') - \lambda_{11}\psi_1(\mathbf{r}) - \lambda_{12}\psi_2(\mathbf{r}) = 0, \\ \frac{\delta L}{\delta \psi_2^*} &= H_0(\mathbf{r})\psi_2(\mathbf{r}) + \int d\mathbf{r}' \frac{|\psi_1(\mathbf{r}')|^2}{|\mathbf{r} - \mathbf{r}'|} \psi_2(\mathbf{r}) \\ &\quad - \int d\mathbf{r}' \frac{\psi_1^*(\mathbf{r}')\psi_1(\mathbf{r}')}{|\mathbf{r} - \mathbf{r}'|} \psi_2(\mathbf{r}') - \lambda_{21}\psi_1(\mathbf{r}) - \lambda_{22}\psi_2(\mathbf{r}) = 0, \\ \frac{\delta L}{\delta \lambda_{ij}} &= \delta_{ij} - \langle \psi_i | \psi_j \rangle = 0 \quad \text{for any } i, j = 1, 2. \end{aligned} \quad (2.40)$$

Finally, we have the same form of fundamental equation of the electronic structure theory as follows:

$$\begin{aligned} \left[-\frac{\nabla^2}{2} - V_n(\mathbf{r}) + V_H(\mathbf{r}) \right] \psi_1(\mathbf{r}) + \int d\mathbf{r}' V_X(\mathbf{r}, \mathbf{r}') \psi_1(\mathbf{r}') &= \lambda_{11}\psi_1(\mathbf{r}) - \lambda_{12}\psi_2(\mathbf{r}) \\ \left[-\frac{\nabla^2}{2} - V_n(\mathbf{r}) + V_H(\mathbf{r}) \right] \psi_2(\mathbf{r}) + \int d\mathbf{r}' V_X(\mathbf{r}, \mathbf{r}') \psi_2(\mathbf{r}') &= \lambda_{21}\psi_1(\mathbf{r}) - \lambda_{22}\psi_2(\mathbf{r}) \end{aligned} \quad (2.41)$$

where $V_H(\mathbf{r})$ and $V_X(\mathbf{r}, \mathbf{r}')$ are the Hartree potential and the Fock-exchange potential, respectively. Both of them are expressed as follows:

$$V_H(\mathbf{r}) = \sum_j \int d\mathbf{r}' \frac{|\psi_j(\mathbf{r}')|^2}{|\mathbf{r} - \mathbf{r}'|}, \quad V_X(\mathbf{r}, \mathbf{r}') = - \sum_j \frac{\psi_j^*(\mathbf{r}')\psi_j(\mathbf{r})}{|\mathbf{r} - \mathbf{r}'|} \quad \text{for } j = 1, 2. \quad (2.42)$$

The final step is to eliminate the Lagrange multiplier term. Because the Hamiltonian is Hermitian and so do the Lagrange multipliers, elimination of the Lagrange multipliers can be achieved by using unitary transformation, which diagonalizes Lagrange multipliers as follows:

$$S \begin{pmatrix} \lambda_{11} & \lambda_{12} \\ \lambda_{21} & \lambda_{22} \end{pmatrix} S^{-1} = \begin{pmatrix} \varepsilon_1 & 0 \\ 0 & \varepsilon_2 \end{pmatrix}. \quad (2.43)$$

Consequently, now we define new wavefunctions, ϕ_1 and ϕ_2 , as follows:

$$\phi_i = \sum_j S_{ij} \psi_j. \quad (2.44)$$

Thus, we can write eq.2.41 as

$$\begin{cases} \left[-\frac{\nabla^2}{2} - V_n(\mathbf{r}) + V_H(\mathbf{r}) \right] \phi_1(\mathbf{r}) + \int d\mathbf{r}' V_X(\mathbf{r}, \mathbf{r}') \phi_1(\mathbf{r}') = \varepsilon_1 \phi_1(\mathbf{r}), \\ \left[-\frac{\nabla^2}{2} - V_n(\mathbf{r}) + V_H(\mathbf{r}) \right] \phi_2(\mathbf{r}) + \int d\mathbf{r}' V_X(\mathbf{r}, \mathbf{r}') \phi_2(\mathbf{r}') = \varepsilon_2 \phi_2(\mathbf{r}). \end{cases} \quad (2.45)$$

Finally, we generalize the Hartree–Fock equation for the case of the N -electrons system as follows:

$$\left[-\frac{\nabla^2}{2} - V_n(\mathbf{r}) + V_H(\mathbf{r}) \right] \phi_i(\mathbf{r}) + \int d\mathbf{r}' V_X(\mathbf{r}, \mathbf{r}') \phi_i(\mathbf{r}') = \varepsilon_i \phi_i(\mathbf{r}). \quad (2.46)$$

Here, we show that we change our approximation from classical in the mean-field approximation into quantum electrons in the Hartree–Fock equation. The Fock-exchange potential V_X arises precisely from Pauli's exclusion principle and prevent two electrons from occupying the same quantum state. However, the potential V_X is nonlocal, and its evaluation involves an integration over the additional variable \mathbf{r}' . This problem significantly complicates the practical

solution of the Hartree–Fock equations.

2.2 Density Functional Theory

2.2.1 Hohenberg–Kohn theorem

In section 2.1.4, we explained that any change in E must be associated with changes in the many-body wavefunction, Ψ . Therefore, we explicitly expressed E as a functional of Ψ as follows:

$$E = \mathcal{F}[\Psi]. \quad (2.47)$$

Hohenberg–Kohn in 1964 stated (also known as the Hohenberg–Kohn theorem): *in the ground state, i.e. E is in the lowest possible energy of the system, E become a functional of the electron density.*

$$E = F[n]. \quad (2.48)$$

The Hohenberg–Kohn theorem is based on the following three premises:

- In any quantum state, the total energy is a functional of the many-body wavefunction, which is explicitly expressed in eq.2.47.
- In any quantum state, the external potential, V_n , uniquely determines the many-body wavefunction: $V_n \rightarrow \Psi$.
- In the ground state, the electron density uniquely determines the external potential of the nuclei, V_n : $n \rightarrow V_n$.

By combining the three premises, we can conclude that in the ground state, the density uniquely determines the total energy: $n \rightarrow V_n \rightarrow \Psi \rightarrow E$ which is refer to Hohenberg-Kohn theorem in eq.2.48.

Now, let us prove the validity of those premises. The first premise can be proven from the explanation in the previous section. The second premise means that if the atomic position is changed, the potential energy V_n also changes, then the different many-body wavefunctions are obtained. This premise is rather intuitive because different V_n will give different Hamiltonians, which leads to different solutions. Thus, this premise requires a careful proof, which is possible by considering that all scalar potentials appearing in the Hamiltonian are Coulomb potentials. Lastly, the last premise is not intuitive, but it can be mathematically proven.

However, before proving this premise, it is better to introduce the concept of variational principle. The concept of variational principle states that the energy expectation value of any state is larger or equal to the ground state. To understand the concept, let us first consider the Schrödinger equation for N electrons as

$$\mathcal{H}\Phi = E_0\Phi, \quad (2.49)$$

where Φ is the ground state of the system, and E_0 is the ground-state energy. Now, let us consider a trial state, Ψ , with the expectation of the energy defined as

$$E[\Psi] = \frac{\langle \Psi | \mathcal{H} | \Psi \rangle}{\langle \Psi | \Psi \rangle}, \quad (2.50)$$

where $\langle \Psi | \mathcal{H} | \Psi \rangle = \int \Psi^* \mathcal{H} \Psi d\tau$ with $\tau = (\mathbf{r}_1, \sigma_1, \dots, \mathbf{r}_N, \sigma_N)$. The variational principle states that

$$E[\Psi] \geq E_0. \quad (2.51)$$

By using the previous definition, we can rewrite the equation as

$$\begin{aligned} \int \Psi^* \mathcal{H} \Psi d\tau &\geq E_0 \int \Psi_T^* \Psi_T d\tau \\ \int \left(\sum_j a_j^* u_j \right) \left(\sum_i E_i a_i u_i \right) d\tau &\geq E_0 \int \left(\sum_j a_j^* u_j \right) \left(\sum_i a_i u_i \right) d\tau \\ \sum_{ij} a_j^* a_i E_i \int u_j^* u_i d\tau &\geq E_0 \sum_{ij} a_j^* a_i \int u_j^* u_i d\tau \\ \sum_{ij} a_j^* a_i E_i \delta_{ij} &\geq E_0 \sum_{ij} a_j^* a_i \delta_{ij} \\ \sum_i E_i |a_i|^2 &\geq E_0 \sum_i |a_i|^2 \end{aligned} \quad (2.52)$$

which proves that

$$E_T = \frac{\int \Psi^* \mathcal{H} \Psi d\tau}{\int \Psi_T^* \Psi_T d\tau} \geq E_0. \quad (2.53)$$

Now, by using the concept variational principle, we prove the last premise. To make the proving easier, let us introduce the symbolic notation for the kinetic and Coulomb energies in eq.2.16:

$$T = -\sum_i \frac{1}{2} \nabla_i^2, \quad V_{ee} = \frac{1}{2} \sum_{i \neq j} \frac{1}{|\mathbf{r}_i - \mathbf{r}_j|}. \quad (2.54)$$

Thus, we can write the total energy as

$$E = \langle \Psi | \sum_i V_n(\mathbf{r}_i) | \Psi \rangle + \langle \Psi | T + V_{ee} | \Psi \rangle \quad (2.55)$$

By using the relation between the wavefunction and electron density, we obtain

$$E = \int d\mathbf{r} n(\mathbf{r}) V_n(\mathbf{r}) + \langle \Psi | T + V_{ee} | \Psi \rangle. \quad (2.56)$$

Now, consider two different potentials, $V_n(\mathbf{r})$ and $V'_n(\mathbf{r})$, where $V_n(\mathbf{r}) \neq V'_n(\mathbf{r})$. Suppose $V_n(\mathbf{r})$ and $V'_n(\mathbf{r})$ lead to the same density n . Let E and Ψ be the ground-state energy and wavefunction of potential V_n , respectively. From the two previous premises, each potential has a unique ground-state energy and wavefunction, $V_n \rightarrow \Psi \rightarrow E$, so E' and Ψ' become the ground-state energy and wavefunction of potential V'_n , respectively. Because Ψ is not the ground state of V'_n , we have

$$\begin{aligned} & \int d\mathbf{r} n(\mathbf{r}) V'_n(\mathbf{r}) + \langle \Psi | T + V_{ee} | \Psi \rangle > E' \\ & \int d\mathbf{r} n(\mathbf{r}) V'_n(\mathbf{r}) + E - \int d\mathbf{r} n(\mathbf{r}) V_n(\mathbf{r}) > E' \\ & E - E' > \int d\mathbf{r} n(\mathbf{r}) [V_n(\mathbf{r}) - V'_n(\mathbf{r})]. \end{aligned} \quad (2.57)$$

Now, we can apply similar logic as above for the case of V_n resulting

$$E' - E > \int d\mathbf{r} n(\mathbf{r}) [V'_n(\mathbf{r}) - V_n(\mathbf{r})]. \quad (2.58)$$

Finally, if we add the last two equations, we will have $0 > 0$, which is obviously contradicting. Therefore, the assumption of two different potentials, $V_n(\mathbf{r}) \neq V'_n(\mathbf{r})$, resulting in the same ground-state density n must be false. This proves the last premise and completes the proof for the Hohenberg theorem.

2.2.2 The Exchange-Correlation Term

The Hohenberg–Kohn theorem states that the total energy of many electrons in their ground state is a functional of electron density; however, the functional itself has not yet been constructed by this theorem. If we try to

find a hint from the Hohenberg–Kohn theorem, the functional can be written as

$$F[n] = \int d\mathbf{r} n(\mathbf{r})V_n(\mathbf{r}) + \langle \Psi[n]|T + V_{ee}|\Psi[n] \rangle. \quad (2.59)$$

The first term of the functional is already explicitly dependent on the density, whereas the second (kinetic energy) and third (Coulomb energy) terms are still implicitly dependent on the density. The idea proposed by Kohn and Sham in 1965 was to split the implicit terms to be the kinetic and Coulomb energies of independent electron additional with extra term so-called *exchange and correlation* energy, E_{XC} in which everything that is left out is into accounts:

$$E = F[n] = \int d\mathbf{r} n(\mathbf{r})V_n(\mathbf{r}) - \sum_i \int d\mathbf{r} \phi'_i(\mathbf{r}) \frac{\nabla^2}{2} \phi_i(\mathbf{r}) + \frac{1}{2} \int \int d\mathbf{r} d\mathbf{r}' \frac{n(\mathbf{r})n(\mathbf{r}')}{|\mathbf{r} - \mathbf{r}'|} + E_{XC}[n]. \quad (2.60)$$

At this stage, we introduce exchange-correlation energy as an approximate functional, *e.g.* E_{XC}^{LDA} , to take further steps.

To introduce the Kohn–Sham equation, we need to construct an accurate exchange and correlation functional $E_{XC}[n]$. The simplest way to construct $E_{XC}[n]$ is by using the concept of the homogeneous gas electron model. This model is created with the assumption that the energy of the electron density in small volume at the \mathbf{r} (local density electron) is given by the homogeneous electron gas at the density. The exchange-correlation energy constructed by this assumption is called local density approximation (LDA) exchange-correlation energy. The exchange-correlation energy functional is written adding up each contribution from exchange (E_x) and correlation energy (E_c). In LDA, E_x is defined by Dirac as

$$E_x = -\frac{3}{4} \left(\frac{3}{\pi} \right)^{\frac{1}{3}} \int_V n^{4/3}(\mathbf{r}) d\mathbf{r} \quad (2.61)$$

In contrast to the exchange energy, it is not possible to analytically determine the correlation energy. Correlation energy is possible to determine by calculating the correlation energy for the simple model by directly solving the many-particle Schrödinger equation using the stochastic numerical method [59]. The correlation energy E_c can thus be extracted from analytical estimation or numerical data by removing the known kinetic, Hartree, and

exchange contribution from the calculated total energies. Nowadays, the most accurate E_c is given by the data obtained using the quantum Monte Carlo calculation. Not only does the LDA approximation work for materials with slowly varying or homogeneous electron densities but also practically demonstrates surprisingly accurate results for a wide range of ionic, covalent, and metallic materials.

An alternative, slightly more sophisticated approximation is the *Generalized Gradient Approximation*(GGA), which estimates the contribution of each volume element to the exchange-correlation based on the magnitude and gradient of the electron density within that element. The exchange correlation for GGA can be written as follows:

$$E_{XC}^{GGA}[n_\uparrow, n_\downarrow] = \int d^3r f(n_\uparrow, n_\downarrow, \nabla n_\uparrow, \nabla n_\downarrow). \quad (2.62)$$

The GGA exchange-correlation energy is suitable for describing 3D metals, 3D semiconductors, strong metallic ferromagnets, molecules, and molecular solids without $\pi - \pi$ stacking.

2.2.3 The Kohn–Sham Equation

In the last section, we have introduced some forms of $E_{XC}[n]$, each of which is represented by an explicit functional of $n(\mathbf{r})$. This means that the functional derivatives of $E_{XC}[n]$ are given in computations. In the density functional theory, the function $n(\mathbf{r})$ that minimizes the total energy, E , is the ground-state density n_0 , which can be expressed as follows:

$$\frac{\delta E}{\delta n(\mathbf{r})} = \frac{\delta}{\delta n(\mathbf{r})} \left[\int d\mathbf{r} n(\mathbf{r})V_n(\mathbf{r}) - \sum_i \int d\mathbf{r} \phi'_i(\mathbf{r}) \frac{\nabla^2}{2} \phi_i(\mathbf{r}) + \frac{1}{2} \int \int d\mathbf{r} d\mathbf{r}' \frac{n(\mathbf{r})n(\mathbf{r}')}{|\mathbf{r} - \mathbf{r}'|} + E_{XC}[n] \right] \Big|_{n_0} = 0. \quad (2.63)$$

Now, we find the same minimization problem as that in the derivation of the Hartree–Fock equation. By using similar process, we can find an equation for the wavefunction $\phi_i(\mathbf{r})$. By applying the chain rule to the E with respect to any of ψ_i^* , we obtain

$$\frac{\delta E}{\delta \psi_i^*} = \frac{\delta E}{\delta n} \frac{\delta n}{\delta \psi_i^*} = \frac{\delta E}{\delta n} \psi_i, \quad (2.64)$$

Eq.2.63 and 2.64 state that the Kohn–Sham orbitals must satisfy the following condition:

$$\frac{\delta E}{\delta \psi_i^*} = 0. \quad (2.65)$$

As we already know, the Kohn–Sham wavefunctions must satisfy the orthonormality:

$$\langle \psi_i | \psi_j \rangle = \delta_{ij}. \quad (2.66)$$

Thus, we have Eq.2.65 and 2.66 as the two constraints that must be satisfied. The existence of these constraints causes the minimization process to be done effectively by using the Lagrange multipliers (δ_{ij}) method [60]. Hence, we first introduce Lagrange functional as follows:

$$L = E - \sum_{ij} \lambda_{ij} [\langle \psi_i | \psi_j \rangle - \delta_{ij}], \quad (2.67)$$

and looking for the extrema of this functional, we find

$$\frac{\delta L}{\delta \psi_i^*} = 0 \longrightarrow \frac{\delta E}{\delta \psi_i^*} = \sum_{ij} \lambda_{ij} \psi_j(\mathbf{r}). \quad (2.68)$$

From this, we can use Eq.2.64 and 2.2.2 to evaluate the functional derivative, $\frac{\delta E}{\delta \psi_i^*}$. Thus, we obtain

$$\begin{aligned} & -\frac{\nabla^2}{2} \psi_i(\mathbf{r}) + \frac{\delta}{\delta n} \left\{ \frac{1}{2} \int \int d\mathbf{r} d\mathbf{r}' \frac{n(\mathbf{r})n(\mathbf{r}')}{|\mathbf{r} - \mathbf{r}'|} + \int V_{ext}(\mathbf{r})n(\mathbf{r})d\mathbf{r} + E_{XC}[n] \right\} \psi_i(\mathbf{r}) \\ & = \sum_j \lambda_{ij} \psi_j(\mathbf{r}), \end{aligned} \quad (2.69)$$

where the second term needs to be simplified by using the definition of functional derivative. Thus, the first term of the second term in Eq.2.69 can be simplified by firstly denoting it as $E_H[n]$:

$$E_H[n] = \frac{1}{2} \int \int d\mathbf{r} d\mathbf{r}' \frac{n(\mathbf{r})n(\mathbf{r}')}{|\mathbf{r} - \mathbf{r}'|}, \quad (2.70)$$

where H denotes Hartree. By using the definition of the functional derivative,

$$\begin{aligned}
\int \frac{\delta E_H[n]}{\delta n}(\mathbf{r})g(\mathbf{r}) d\mathbf{r} &= \left[\frac{d}{d\varepsilon} V_H[n(\mathbf{r}) + \varepsilon g(\mathbf{r})] \right]_{\varepsilon=0} \\
&= \left[\frac{d}{d\varepsilon} \left(\frac{1}{2} \int \int d\mathbf{r}d\mathbf{r}' \frac{[n(\mathbf{r}) + \varepsilon g(\mathbf{r})][n(\mathbf{r}') + \varepsilon g(\mathbf{r}')] }{|\mathbf{r} - \mathbf{r}'|} \right) \right] \\
&= \frac{1}{2} \int \int \frac{n(\mathbf{r}')g(\mathbf{r})}{|\mathbf{r} - \mathbf{r}'|} d\mathbf{r}d\mathbf{r}' + \frac{1}{2} \int \int \frac{n(\mathbf{r})g(\mathbf{r}')}{|\mathbf{r} - \mathbf{r}'|} d\mathbf{r}d\mathbf{r}',
\end{aligned} \tag{2.71}$$

in which the first term is equal to the second term in the last Eq.2.71 because r and r' are interchangeable. Thus, we obtain

$$\int \frac{\delta E_H[n]}{\delta n}(\mathbf{r})g(\mathbf{r}) d\mathbf{r} = \int \left(\int d\mathbf{r}' \frac{n(\mathbf{r}')}{|\mathbf{r} - \mathbf{r}'|} \right) g(\mathbf{r}) d\mathbf{r}, \tag{2.72}$$

and the functional derivative of E_H with respect to $n(\mathbf{r})$ is

$$\frac{\delta E_H[n]}{\delta n(\mathbf{r})} = \int d\mathbf{r}' \frac{n(\mathbf{r}')}{|\mathbf{r} - \mathbf{r}'|}. \tag{2.73}$$

The middle term of the second term in Eq.2.69 can be simplified in the same way as the first term by firstly denoting it as $E_{ext}[n]$:

$$E_{ext}[n] = \frac{\delta}{\delta n(\mathbf{r})} \left[\int V_{ext}(\mathbf{r})n(\mathbf{r})d\mathbf{r} \right], \tag{2.74}$$

and applying the definition in Eq.2.72,

$$\begin{aligned}
\int \frac{\delta E_{ext}[n]}{\delta n}(\mathbf{r})g(\mathbf{r}) d\mathbf{r} &= \left[\frac{d}{d\varepsilon} E_{ext}[n + \varepsilon g] \right]_{\varepsilon=0} \\
&= \left[\frac{d}{d\varepsilon} \int [n(\mathbf{r}) + \varepsilon g(\mathbf{r})]V_{ext}(\mathbf{r})d\mathbf{r} \right]_{\varepsilon=0} \\
&= \int V_{ext}(\mathbf{r})g(\mathbf{r})d\mathbf{r}.
\end{aligned} \tag{2.75}$$

Thus, from Eq.2.75, we obtain

$$\frac{\delta E_{ext}[n]}{\delta n(\mathbf{r})} = V_{ext}. \tag{2.76}$$

Therefore, Eq.2.69 can now be expressed as

$$\left[-\frac{\nabla^2}{2} + V_{ext}(\mathbf{r}) + \int d\mathbf{r}' \frac{n(\mathbf{r}')}{|\mathbf{r} - \mathbf{r}'|} + \frac{\delta E_{XC}}{\delta n(\mathbf{r})} \right] \psi_i(\mathbf{r}) = \sum_j \lambda_{ij} \psi_j(\mathbf{r}). \quad (2.77)$$

The third and fourth terms inside the square brackets are the Hartree potential, $V_H(\mathbf{r})$, and the exchange and correlation potentials, $V_{XC}(\mathbf{r})$, respectively. The explicit form of V_{XC} is given by E_x and a functional form of E_C , *e.g.* E_{XC}^{GGA} , determined in each simulation. Eq. 2.77 can also be written as

$$H_{eff} \psi_i(\mathbf{r}) = \left[-\frac{\nabla^2}{2} + V_{eff}(\mathbf{r}) \right] \psi_i(\mathbf{r}) = \sum_j \lambda_{ij} \psi_j(\mathbf{r}). \quad (2.78)$$

$$V_{eff}(\mathbf{r}) = V_{ext}(\mathbf{r}) + V_H(\mathbf{r}) + V_{XC}(\mathbf{r}),$$

which shows the single-particle Schrödinger equation with one-electron Hamiltonian H_{eff} as a Hermitian operator and effective potential V_{eff} as a local operator. Thus, λ_{ij} is a Hermitian matrix and can be diagonalized by a unitary transformation of the Kohn–Sham wavefunctions. Finally, by introducing the new wavefunctions, $\phi_i(\mathbf{r})$, and the eigen values, ε_i , the Kohn–Sham equations could be written as

$$\left[-\frac{1}{2} \nabla^2 + V_{eff}(\mathbf{r}) \right] \phi_i(\mathbf{r}) = \varepsilon_i \phi_i(\mathbf{r}). \quad (2.79)$$

2.2.4 Extension to Spin-Polarized DFT

For the case of magnetic system, we shall introduce energy functionals considering the spin density as a relevant secondary order parameter. Let us introduce the scalar electronic density and magnetization density as follows:

$$n(\mathbf{r}) = n_{\uparrow}(\mathbf{r}) + n_{\downarrow}(\mathbf{r}) \quad (2.80)$$

$$m(\mathbf{r}) = g\mu_B(n_{\uparrow}(\mathbf{r}) - n_{\downarrow}(\mathbf{r})) \quad (2.81)$$

$\uparrow(\downarrow)$ are up(down) spin direction. The spin density can also be represented in terms of spin-up and spin-down orbital, $\phi_{\sigma}(\mathbf{r})$ as follows:

$$n_{\sigma}(\mathbf{r}) = \sum_i |\phi_{\sigma}(\mathbf{r})|^2 \quad (2.82)$$

where $\sigma = \uparrow, \downarrow$ with the Kohn–Sham equation can be rewritten as

$$\left[-\frac{1}{2}\nabla^2 + V_{eff}^\sigma(\mathbf{r}) \right] \phi_{i\sigma}(\mathbf{r}) = \varepsilon_{i\sigma} \phi_{i\sigma}(\mathbf{r}), \quad (2.83)$$

where the effective potential can be written as

$$V_{eff}^\sigma(\mathbf{r}) = \int \frac{n(\mathbf{r}')}{|\mathbf{r} - \mathbf{r}'|} d\mathbf{r}' + \frac{\delta E_{XC}^{GGA}[n_\uparrow(\mathbf{r}), n_\downarrow(\mathbf{r})]}{\delta n_\sigma(\mathbf{r})} + V_{ext}(\mathbf{r}) + \mu B(\mathbf{r}) \quad (2.84)$$

The last term on the left side is so-called effective magnetic field with $\mathbf{B}_{XC}(\mathbf{r})$ as exchange and correlation magnetic field.

2.2.5 Ultrasoft Pseudopotential

In early 1990, David Vanderbilt developed for the first time a new approach for the construction of pseudopotential, namely, ultrasoft pseudopotential [61]. The valence electron density is defined as follows:

$$n_v(\mathbf{r}) = \sum_{n,\mathbf{k}} \phi_{n\mathbf{k}} * (\mathbf{r}) \phi_{n\mathbf{k}}(\mathbf{r}) + \sum_{i,j} \rho_{ij} Q_{ji}(\mathbf{r}), \quad (2.85)$$

where

$$Q_{ji}(\mathbf{r}) = \psi_i * (\mathbf{r}) \psi_j(\mathbf{r}) - \phi_i * (\mathbf{r}) \phi_j(\mathbf{r}), \quad (2.86)$$

$$\rho_{ij} = \sum_{n,\mathbf{k}} \langle \beta_i | \phi_{n\mathbf{k}} \rangle \langle \phi_{n\mathbf{k}} | \beta_j \rangle. \quad (2.87)$$

Eq.2.86 shows an augmentation function containing $\psi_i(\mathbf{r})$ and $\psi_j(\mathbf{r})$, which are the ultrasoft and electron wavefunctions, respectively. The difference between the charge density of many electrons and pseudo wavefunctions is called augmentation charges.

Here, the ultra (pseudo) wavefunction obeys the orthonormality condition by defining a nonlocal operator S as follows:

$$\langle \phi | S | \phi \rangle = \delta_{ij}. \quad (2.88)$$

2.2.6 Monkhorst–Pack Scheme

To optimize the calculation, a special set of k-points in the Brillouin zone has to be carefully selected. In this study, the Monkhorst–Pack scheme is implemented as a scheme with an efficient means to generate k-points with

some good accuracy. In this method, three integers q along the coordinates is used as the number of the special k-points. By using these integers, a sequence of numbers is generated as follows:

$$u_r = \frac{2r - q - 1}{2q} \quad (r = 1, 2, 3, 4, \dots, q). \quad (2.89)$$

By using u_r , q^3 distinct points, uniformly distributed in the Brillouin zone, can be obtained by defining

$$k_{j,k,l} = u_j b_1 + u_k b_2 + u_l b_3 \quad (2.90)$$

where b_1, b_2, b_3 are the reciprocal lattice vectors.

2.3 Theory of Electronic States in Graphene

2.3.1 Bloch Theorem

In the crystal, the Kohn–Sham effective potential for an electron, $V_{eff}(\mathbf{r})$, has periodicity

$$V_{eff}(\mathbf{r} + \mathbf{R}) = V_{eff}(\mathbf{r}) \quad (2.91)$$

where \mathbf{R} is a translation vector of the crystal lattice. It means that the crystal offers the translational symmetry. In quantum mechanics, translation by the lattice vector \mathbf{R} can be expressed by the following operator.

$$\hat{S}_{\mathbf{R}} = \exp\left(\frac{1}{\hbar} \hat{\mathbf{p}} \cdot \mathbf{R}\right) = \exp(\mathbf{R} \cdot \nabla). \quad (2.92)$$

This operator generates a unitary transformation if it is operated to a state vector that possesses a real momentum. We can understand the operation of operator \hat{S} by explicitly operating it to the following wavefunction:

$$\psi(\mathbf{r}) = \sum_{\mathbf{G}} C_{\mathbf{G}} \exp(i\mathbf{G} \cdot \mathbf{r}). \quad (2.93)$$

which results in

$$\begin{aligned}
\hat{S}_{\mathbf{R}}\psi(\mathbf{r}) &= \sum_{\mathbf{G}} C_{\mathbf{G}} \exp(\mathbf{R} \cdot \nabla) \exp(i\mathbf{G} \cdot \mathbf{r}) \\
&= \sum_{\mathbf{G}} C_{\mathbf{G}} (\mathbf{R} \cdot \nabla) \exp(i\mathbf{G} \cdot \mathbf{r}) \\
&= \sum_{\mathbf{G}} C_{\mathbf{G}} (i\mathbf{R} \cdot \mathbf{G}) \exp(i\mathbf{G} \cdot \mathbf{r}) \\
&= \sum_{\mathbf{G}} C_{\mathbf{G}} \exp(i\mathbf{R} \cdot \mathbf{G}) \exp(i\mathbf{G} \cdot \mathbf{r}) \\
&= \sum_{\mathbf{G}} C_{\mathbf{G}} \exp(i\mathbf{G} \cdot (\mathbf{r} + \mathbf{R})) \\
&= \psi(\mathbf{r} + \mathbf{R})
\end{aligned} \tag{2.94}$$

where \mathbf{G} is the wave vector. After the translation operation by operator $\hat{S}_{\mathbf{R}}$, the function is shifted by \mathbf{R} . If we recall effective Hamiltonian for the electronic system in the crystal as

$$\hat{H}_{eff} = -\frac{1}{2}\nabla^2 + V_{eff}(\mathbf{r}), \tag{2.95}$$

and applied translation operator, we can obtain the following operation:

$$\begin{aligned}
\hat{S}_{\mathbf{R}}\hat{H}_{eff}\phi_{n,\mathbf{k},\sigma}(\mathbf{r}) &= \exp(\mathbf{R} \cdot \nabla) \left\{ -\frac{1}{2}\nabla^2 + V_{eff}(\mathbf{r}) \right\} \phi_{n,\mathbf{k},\sigma}(\mathbf{r}) \\
&= \left\{ -\frac{1}{2}\nabla^2 + V_{eff}(\mathbf{r} + \mathbf{R}) \right\} \phi_{n,\mathbf{k},\sigma}(\mathbf{r} + \mathbf{R}) \\
&= \left\{ -\frac{1}{2}\nabla^2 + V_{eff}(\mathbf{r} + \mathbf{R}) \right\} \hat{S}_{\mathbf{R}}\phi_{n,\mathbf{k},\sigma}(\mathbf{r}).
\end{aligned} \tag{2.96}$$

By using Eq.2.91, we can have the following operator identity:

$$\begin{aligned}
\hat{S}_{\mathbf{R}}\hat{H}_{eff}\hat{S}_{\mathbf{R}}^{-1} &= -\frac{1}{2}\nabla^2 + V_{eff}(\mathbf{r} + \mathbf{R}) \\
&= -\frac{1}{2}\nabla^2 + V_{eff}(\mathbf{r}) \\
&= \hat{H}_{eff}.
\end{aligned} \tag{2.97}$$

Therefore, we conclude that \hat{H}_{eff} is invariant under the translational transformation $\hat{S}_{\mathbf{R}}$. Both operators follow the commutation relation

$$[\hat{S}_{\mathbf{R}}, \hat{H}_{eff}] = 0, \tag{2.98}$$

which means that $\hat{S}_{\mathbf{R}}$ and \hat{H}_{eff} are commutable.

Recall the Kohn–Sham equation, which is written in eq.2.79. By operating the translational operator $\hat{S}_{\mathbf{R}}$ on both sides, we can find the following relation:

$$\begin{aligned}\hat{S}_{\mathbf{R}}\hat{H}_{eff}\phi_{n,\mathbf{k},\sigma}(\mathbf{r}) &= \hat{S}_{\mathbf{R}}\varepsilon_{n,\mathbf{k}}\phi_{n,\mathbf{k},\sigma}(\mathbf{r}) \\ \hat{H}_{eff}\hat{S}_{\mathbf{R}}\phi_{n,\mathbf{k},\sigma}(\mathbf{r}) &= \varepsilon_{n,\mathbf{k}}\hat{S}_{\mathbf{R}}\phi_{n,\mathbf{k},\sigma}(\mathbf{r}) \\ \hat{H}_{eff}\phi_{n,\mathbf{k},\sigma}(\mathbf{r} + \mathbf{R}) &= \varepsilon_{n,\mathbf{k}}\phi_{n,\mathbf{k},\sigma}(\mathbf{r} + \mathbf{R}),\end{aligned}\tag{2.99}$$

which is showing that $\phi_{n,\mathbf{k},\sigma}(\mathbf{r} + \mathbf{R})$ is an eigenstate with the eigenvalue $\varepsilon_{n,\mathbf{k}}$. For the case without degeneracy, $\phi_{n,\mathbf{k},\sigma}(\mathbf{r} + \mathbf{R})$ has to be identical to $\phi_{n,\mathbf{k},\sigma}(\mathbf{r})$, except for an overall phase. By using this rule, we construct the so-called Bloch function.

The phase difference between $\phi_{n,\mathbf{k},\sigma}(\mathbf{r} + \mathbf{R})$ and $\phi_{n,\mathbf{k},\sigma}(\mathbf{r})$ can be explicitly written by introducing a phase factor $\exp(i\mathbf{k} \cdot \mathbf{r})$, so that we have the following relation:

$$\phi_{n,\mathbf{k},\sigma}(\mathbf{r} + \mathbf{R}) = \exp(i\mathbf{k} \cdot \mathbf{R})\phi_{n,\mathbf{k},\sigma}(\mathbf{r}).\tag{2.100}$$

Bloch's theorem states that the solutions of the one-electron equation can be written as a product of a plane wave and a periodic function. By introducing periodic function $u_{n,\mathbf{k},\sigma}(\mathbf{r})$ as

$$u_{n,\sigma}(\mathbf{r}) = \exp(-i\mathbf{k} \cdot \mathbf{r})\phi_{n,\mathbf{k},\sigma}(\mathbf{r})\tag{2.101}$$

where its periodicity can be easily proven as

$$\begin{aligned}u_{n,\sigma}(\mathbf{r} + \mathbf{R}) &= \exp(-i\mathbf{k} \cdot \mathbf{r} - i\mathbf{k} \cdot \mathbf{R})\phi_{n,\mathbf{k},\sigma}(\mathbf{r} + \mathbf{R}) \\ &= \exp(-i\mathbf{k} \cdot \mathbf{r} - i\mathbf{k} \cdot \mathbf{R})\exp(i\mathbf{k} \cdot \mathbf{R})\phi_{n,\mathbf{k},\sigma}(\mathbf{r}) \\ &= \exp(-i\mathbf{k} \cdot \mathbf{r})\phi_{n,\mathbf{k},\sigma}(\mathbf{r}) \\ &= u_{n,\sigma}(\mathbf{r}).\end{aligned}\tag{2.102}$$

We can finally get another form of the Bloch function, which is given as follows:

$$\phi_{n,\mathbf{k},\sigma}(\mathbf{r}) = \exp(i\mathbf{k} \cdot \mathbf{r})u_{n,\sigma}(\mathbf{r})\tag{2.103}$$

For the case of degeneracy, by introducing a unitary transformation, the same function form like eq.2.103 is concluded.

By performing Fourier transformation on the Bloch function, we can obtain

the Wannier functions. The Wannier functions are localized functions that span the same space as the eigenstates of a band or a group of bands. Using the Bloch function solution of materials $\phi_{n,\mathbf{k},\sigma}(\mathbf{r})$, the corresponding Wannier orbitals around a lattice point \mathbf{r}_i can be expressed as follows:

$$\phi_{n,\sigma}(\mathbf{r} - \mathbf{r}_i) = \frac{1}{\sqrt{N}} \sum_{\mathbf{k}} \exp(i\mathbf{k} \cdot \mathbf{r}_i) \phi_{n,\mathbf{k},\sigma}(\mathbf{r}). \quad (2.104)$$

A set of $\phi_{n,\mathbf{k},\sigma}(\mathbf{r})$ gives an orthonormal complete set as follows:

$$\int d^3r \phi_{n,\mathbf{k},\sigma}^*(\mathbf{r}) \phi_{n',\mathbf{k}',\sigma'}(\mathbf{r}) = \delta_{n,n'} \delta_{\mathbf{k},\mathbf{k}'} \delta_{\sigma,\sigma'}, \quad (2.105)$$

while a set of $\phi_{n,\sigma}(\mathbf{r} - \mathbf{r}_i)$ gives an orthonormal complete set as follows:

$$\begin{aligned} \int d^3r \phi_{n,\sigma}^*(\mathbf{r} - \mathbf{r}_i) \phi_{n,\sigma}(\mathbf{r} - \mathbf{r}_j) &= \frac{1}{N} \sum_{\mathbf{k},\mathbf{k}'} \exp(i\mathbf{k} \cdot \mathbf{r}_i - i\mathbf{k}' \cdot \mathbf{r}_j) \\ &\quad \int d^3r \phi_{n,\mathbf{k},\sigma}^*(\mathbf{r}) \phi_{n,\mathbf{k}',\sigma}(\mathbf{r}) \\ &= \frac{1}{N} \sum_{\mathbf{k},\mathbf{k}'} \exp(i\mathbf{k} \cdot \mathbf{r}_i - i\mathbf{k}' \cdot \mathbf{r}_j) \delta_{\mathbf{k},\mathbf{k}'} \quad (2.106) \\ &= \frac{1}{N} \sum_{\mathbf{k}} \exp(i\mathbf{k} \cdot (\mathbf{r}_i - \mathbf{r}_j)) \\ &= \delta_{\mathbf{r}_i, \mathbf{r}_j} \end{aligned}$$

2.3.2 Tight-Binding Model

In a crystal, an electron is typically bound tightly to one particular atom with some energy E , which is less than the potential barrier between atoms. However, because the wavefunctions of two atoms in the lattice will have some overlap, there is always the possibility that an electron can tunnel through the potential barrier and hop from one atom to another.

The tight-binding approximation deals with the case in which the overlap of the atomic wavefunction is sufficient to require correction to the picture of isolated atoms, but not so much as to render the atomic description completely irrelevant. This approximation is most useful for describing an energy band that arises from partially filled d-orbitals of transition metal atoms or for describing an insulator in solid.

The idea behind the tight-binding model is the ability to tunnel between atoms is favored by the electron because the more extensive space available to

it causes its energy to become lower. The precise amount by which the energy is lowered depends on the nature of the crystal. If an electron tunnels from crystal lattice site i to site j , its energy changes by an amount of $-t_{ij}$. This tunneling effect is equivalent (in the second quantization language) to electron annihilation at site i and creation at site j , so the portion of the Hamiltonian dealing with tunneling can be written as

$$\hat{H} = - \sum_{i,j} t_{ij} \left(c_{i\sigma}^\dagger c_{j\sigma} + H.c. \right) \quad (2.107)$$

where c_i^\dagger and c_j are the fermion creation and annihilation operators, whereas σ denotes the electron spin. The t_{ij} value decreases along with the separation of two atoms. To simplify the model, we can assume that electron only hopping to the neighboring atoms. Thus, $t_{ij} = 0$ for all other atom pairs beside the neighboring atoms. Then, the above equation becomes

$$\hat{H} = - \sum_{i,\gamma} \left(t_{i,i+\gamma} c_i^\dagger c_{i+\gamma} + H.c. \right) \quad (2.108)$$

where γ is the nearest-neighbor site and the sum over γ means to sum over atoms close to i . To diagonalize equation 2.108, we can apply Fourier transforms to creation and annihilation operators.

$$c_j = \frac{1}{\sqrt{N}} \sum_k e^{i\mathbf{k}\cdot\mathbf{r}_j} c_k \quad (2.109)$$

$$c_i^\dagger = \frac{1}{\sqrt{N}} \sum_q e^{-i\mathbf{q}\cdot\mathbf{r}_i} c_q^\dagger \quad (2.110)$$

Therefore, equation 2.108 becomes

$$\begin{aligned} \hat{H} &= - \sum_{i,\gamma} t_{i,i+\gamma} \frac{1}{\sqrt{N}} \sum_q e^{-i\mathbf{q}\cdot\mathbf{r}_i} c_q^\dagger \frac{1}{\sqrt{N}} \sum_k e^{i\mathbf{k}\cdot(\mathbf{r}_i+\mathbf{r}_\gamma)} c_k \\ &= - \frac{1}{N} \sum_{i,\gamma} \sum_{\mathbf{k},\mathbf{q}} t_{i,i+\gamma} e^{i\mathbf{r}_i\cdot(\mathbf{k}-\mathbf{q})} e^{i\mathbf{k}\cdot\mathbf{r}_\gamma} c_q^\dagger c_k \end{aligned} \quad (2.111)$$

Since

$$\frac{1}{N} \sum_l e^{i\mathbf{r}_l\cdot(\mathbf{k}-\mathbf{q})} = \delta_{\mathbf{k},\mathbf{q}} \quad (2.112)$$

our equation becomes

$$\hat{H} = - \sum_{\tau} \sum_{\mathbf{k}} t_{i,i+\gamma} e^{i\mathbf{k}\cdot\mathbf{r}_{\gamma}} c_{\mathbf{k}}^{\dagger} c_{\mathbf{k}} \quad (2.113)$$

2.3.3 Effective Mass Theory

Using the orthonormal set of Bloch function and Wannier orbital from the previous section, we can define a set of creation and annihilation operators, $c_{i,\sigma}^{\dagger}$ and $c_{i,\sigma}$ as well as $c_{n,\mathbf{k},\sigma}^{\dagger}$ and $c_{n,\mathbf{k},\sigma}$. In the single-band case, we have the following relation:

$$\begin{aligned} c_{i,\sigma} &= \frac{1}{\sqrt{N}} \sum_{\mathbf{k}} \exp(-i\mathbf{k} \cdot \mathbf{r}_i) c_{n,\mathbf{k},\sigma}, & c_{n,\mathbf{k},\sigma} &= \frac{1}{\sqrt{N}} \sum_{\mathbf{r}_i} \exp(i\mathbf{k} \cdot \mathbf{r}_i) c_{i,\sigma}, \\ c_{i,\sigma}^{\dagger} &= \frac{1}{\sqrt{N}} \sum_{\mathbf{k}} \exp(i\mathbf{k} \cdot \mathbf{r}_i) c_{n,\mathbf{k},\sigma}^{\dagger}, & c_{n,\mathbf{k},\sigma}^{\dagger} &= \frac{1}{\sqrt{N}} \sum_{\mathbf{r}_i} \exp(-i\mathbf{k} \cdot \mathbf{r}_i) c_{i,\sigma}^{\dagger}. \end{aligned} \quad (2.114)$$

Now, let us consider the second quantization form of the effective Hamiltonian operator, which can be defined as

$$\hat{H}_{eff} = \sum_{\mathbf{k},\sigma} \varepsilon_{n,\mathbf{k}} c_{n,\mathbf{k},\sigma}^{\dagger} c_{n,\mathbf{k},\sigma}. \quad (2.115)$$

the Hamiltonian can be proved by applying it to a trial state of single-particle $|n, \mathbf{k}, \sigma\rangle \equiv c_{n,\mathbf{k},\sigma}^{\dagger} |0\rangle$ as follows:

$$\begin{aligned} \hat{H}_{eff} |n, \mathbf{k}, \sigma\rangle &= \sum_{m,\mathbf{k}',\sigma'} \varepsilon_{m,\mathbf{k}'} c_{m,\mathbf{k}',\sigma'}^{\dagger} c_{m,\mathbf{k}',\sigma'} c_{n,\mathbf{k},\sigma}^{\dagger} |0\rangle \\ &= \sum_{m,\mathbf{k}',\sigma'} \varepsilon_{m,\mathbf{k}'} c_{m,\mathbf{k}',\sigma'}^{\dagger} \left(\{c_{m,\mathbf{k}',\sigma'}, c_{n,\mathbf{k},\sigma}^{\dagger}\} - c_{n,\mathbf{k},\sigma}^{\dagger} c_{m,\mathbf{k}',\sigma'} \right) |0\rangle \\ &= \sum_{m,\mathbf{k}',\sigma'} \varepsilon_{m,\mathbf{k}'} \left(\delta_{m,n} \delta_{\mathbf{k},\mathbf{k}'} \delta_{\sigma,\sigma'} c_{m,\mathbf{k}',\sigma'}^{\dagger} |0\rangle - c_{m,\mathbf{k}',\sigma'}^{\dagger} c_{n,\mathbf{k},\sigma}^{\dagger} c_{m,\mathbf{k}',\sigma'} |0\rangle \right) \\ &= \varepsilon_{n,\mathbf{k}} c_{n,\mathbf{k},\sigma}^{\dagger} |0\rangle \\ \hat{H}_{eff} |n, \mathbf{k}, \sigma\rangle &= \varepsilon_{n,\mathbf{k}} |n, \mathbf{k}, \sigma\rangle. \end{aligned} \quad (2.116)$$

The above expression shows the Schrödinger equation in the second quantization form. By using relation in eq.2.114, the effective Hamiltonian operator could be expressed as follows:

$$\begin{aligned}
\hat{H}_{eff} &= \frac{1}{N} \sum_{\mathbf{k}, \sigma} \varepsilon_{n, \mathbf{k}} \sum_{\mathbf{r}_i} \exp(-i\mathbf{k} \cdot \mathbf{r}_i) c_{i, \sigma}^\dagger \sum_{\mathbf{r}_j} \exp(i\mathbf{k} \cdot \mathbf{r}_j) c_{j, \sigma} \\
&= \sum_{i, j, \sigma} t_{i, j} c_{i, \sigma}^\dagger c_{j, \sigma},
\end{aligned} \tag{2.117}$$

where $t_{i, j}$ is the transfer integral, which is express as

$$t_{i, j} = \frac{1}{N} \sum_{\mathbf{k}} \exp\left(-i\mathbf{k} \cdot (\mathbf{r}_i - \mathbf{r}_j)\right) \varepsilon_{n, \mathbf{k}}. \tag{2.118}$$

To be noted in this derivation, we restrict our consideration only for the n -th band. The band lower than the n -th band is assumed to be filled with electrons, whereas the band higher than the n -th band is assumed to be empty.

To simplify the discussion, let us consider the cubic lattice with lattice constant a and sample length L . Here, we take the infinite length limit, which is so-called continuum limit, where the lattice constant a is small enough compared with the scale of whole sample ($a \rightarrow 0$), the number of lattice point N is large enough to have a microscopic sample ($L \rightarrow \infty$), and the size of the sample is fixed as $R = La = \text{const.}$. Before we continue deriving the effective Hamiltonian into effective continuum Hamiltonian, let us define several mathematical definitions from the continuum limit to simplify the derivation.

First, we introduce continuous variable \mathbf{r}_i and \mathbf{k}_j as

$$\mathbf{r}_i = (an_{i1}, an_{i2}, an_{i3}), \tag{2.119}$$

$$\mathbf{k}_j = \left(\Delta k m_{j1}, \Delta k m_{j2}, \Delta k m_{j3} \right), \tag{2.120}$$

where the latter equation can be reexpressed by defining $\Delta k = \frac{2\pi}{La}$,

$$\mathbf{k}_j = \left(\frac{2\pi}{R} m_{j1}, \frac{2\pi}{R} m_{j2}, \frac{2\pi}{R} m_{j3} \right). \tag{2.121}$$

Because we take the limit of $a \rightarrow 0$ and considering the sufficiently large R , we can define the differentials dr and dk as

$$dr = a, \quad dk = \frac{2\pi}{R}, \tag{2.122}$$

leading to the range of \mathbf{r} and \mathbf{k} as

$$\mathbf{r} \in [0, R]^3, \quad \mathbf{k} \in [-\infty, \infty]^3. \quad (2.123)$$

Now, we start the derivation of the integral equation by eq.2.106

$$\frac{1}{N} \sum_{\mathbf{k}} \exp \left(i\mathbf{k} \cdot (\mathbf{r}_i - \mathbf{r}_j) \right) = \delta_{\mathbf{r}_i, \mathbf{r}_j}. \quad (2.124)$$

From our previous definition on continuum limit, we note that $N = L^3 = (R/a)^3$. Using the definition in eq.2.122 and identifying the summation as an integral, we have

$$\begin{aligned} \left(\frac{a}{R} \right)^3 \sum_{\mathbf{k}} \exp \left(i\mathbf{k} \cdot (\mathbf{r}_i - \mathbf{r}_j) \right) &= \left(\frac{a}{2\pi} \right)^3 \left(\frac{2\pi}{R} \right)^3 \sum_{\mathbf{k}} \exp \left(i\mathbf{k} \cdot (\mathbf{r}_i - \mathbf{r}_j) \right) \\ &= \left(\frac{a}{2\pi} \right)^3 \int d^3k \exp \left(i\mathbf{k} \cdot (\mathbf{r}_i - \mathbf{r}_j) \right) = \delta_{\mathbf{r}_i, \mathbf{r}_j}. \end{aligned} \quad (2.125)$$

By identifying $\delta_{\mathbf{r}_i, \mathbf{r}_j}$ as $\delta(\mathbf{r} - \mathbf{r}')$, we can obtain

$$\int d^3k \exp \left(i\mathbf{k} \cdot (\mathbf{r} - \mathbf{r}') \right) = \left(\frac{2\pi}{a} \right)^3 \delta(\mathbf{r} - \mathbf{r}'). \quad (2.126)$$

Similarly, if we consider the following equation,

$$\frac{1}{N} \sum_{\mathbf{r}} \exp \left(i(\mathbf{k} - \mathbf{k}') \cdot \mathbf{r} \right) = \delta_{\mathbf{k}, \mathbf{k}'}, \quad (2.127)$$

By using the continuum limit definition and identifying the summation as an integral, we can obtain

$$\left(\frac{a}{R} \right)^3 \sum_{\mathbf{r}} \exp \left(i(\mathbf{k} - \mathbf{k}') \cdot \mathbf{r} \right) = \left(\frac{1}{R} \right)^3 \int d^3r \exp \left(i(\mathbf{k} - \mathbf{k}') \cdot \mathbf{r} \right) = \delta_{\mathbf{k}, \mathbf{k}'}. \quad (2.128)$$

by identifying $\delta_{\mathbf{k}, \mathbf{k}'}$ as $\delta(\mathbf{k} - \mathbf{k}')$, we have

$$\int d^3r \exp \left(i(\mathbf{k} - \mathbf{k}') \cdot \mathbf{r} \right) = R^3 \delta(\mathbf{k} - \mathbf{k}'). \quad (2.129)$$

Now, by using the definition in eq.2.125 and 2.128, we have two following expressions:

$$\begin{aligned}
\int d^3r \delta(\mathbf{r} - \mathbf{r}') &= \int d^3r \left(\frac{a}{2\pi}\right)^3 \int d^3k \exp\left(i\mathbf{k} \cdot (\mathbf{r} - \mathbf{r}')\right) \\
&= \int d^3k \left(\frac{a}{2\pi}\right)^3 \left[\int d^3r \exp(i\mathbf{k} \cdot \mathbf{r}) \right] \exp(-i\mathbf{k} \cdot \mathbf{r}') \\
&= \int d^3k \left(\frac{a}{2\pi}\right)^3 R^3 \delta_{\mathbf{k},\mathbf{0}} \exp(-i\mathbf{k} \cdot \mathbf{r}') \\
&= \left(\frac{2\pi}{R}\right)^3 \left(\frac{a}{2\pi}\right)^3 R^3 \sum_{\mathbf{k}} \delta_{\mathbf{k},\mathbf{0}} \\
\int d^3r \delta(\mathbf{r} - \mathbf{r}') &= a^3 \tag{2.130}
\end{aligned}$$

$$\begin{aligned}
\int d^3k \delta_{\mathbf{k},\mathbf{k}'} &= \int d^3k \left(\frac{1}{R}\right)^3 \int d^3r \exp\left(i(\mathbf{k} - \mathbf{k}') \cdot \mathbf{r}\right) \\
&= \left(\frac{1}{R}\right)^3 \int d^3r \left[\int d^3k \exp(i\mathbf{k} \cdot \mathbf{r}) \right] \exp(i\mathbf{k}' \cdot \mathbf{r}) \\
&= \left(\frac{1}{R}\right)^3 \int d^3r \left(\frac{2\pi}{a}\right)^3 \delta_{\mathbf{r},\mathbf{0}} \exp(i\mathbf{k}' \cdot \mathbf{r}) \\
&= \left(\frac{1}{R}\right)^3 \left(\frac{2\pi}{a}\right)^3 a^3 \sum_{\mathbf{r}} \delta_{\mathbf{r},\mathbf{0}} \\
\int d^3k \delta(\mathbf{k} - \mathbf{k}') &= \left(\frac{2\pi}{R}\right)^3. \tag{2.131}
\end{aligned}$$

By using the range of \mathbf{r} and \mathbf{k} in eq.2.123, the integral in eq.2.126, 2.129, 2.130, and 2.131 can be completed as follows:

$$\begin{aligned}
\int_0^R d^3r \exp\left(i(\mathbf{k} - \mathbf{k}') \cdot \mathbf{r}\right) &= R^3 \delta(\mathbf{k} - \mathbf{k}'), & \int_{-\infty}^{\infty} d^3k \delta(\mathbf{k} - \mathbf{k}') &= \left(\frac{2\pi}{R}\right)^3 \\
\int_{-\infty}^{\infty} d^3k \exp\left(i\mathbf{k} \cdot (\mathbf{r} - \mathbf{r}')\right) &= \left(\frac{2\pi}{a}\right)^3 \delta(\mathbf{r} - \mathbf{r}'), & \int_0^R d^3r \delta(\mathbf{r} - \mathbf{r}') &= a^3.
\end{aligned} \tag{2.132}$$

Finally, let us define field operators using the Bloch functions as

$$\psi_{\sigma}^{\dagger}(\mathbf{r}) = \left(\frac{R}{2\pi}\right)^3 \int_{-\infty}^{\infty} d^3k \exp(i\mathbf{k} \cdot \mathbf{r}) c_{\mathbf{k},\sigma}^{\dagger}, \tag{2.133}$$

$$c_{\mathbf{k},\sigma}^\dagger = \frac{1}{(aR)^{3/2}} \int_0^R d^3r \exp(-i\mathbf{k} \cdot \mathbf{r}) \psi_\sigma^\dagger(\mathbf{r}) \quad (2.134)$$

Now, we start our derivation of effective continuum Hamiltonian. For the sake of simplicity, we consider a simple cubic structure taking into account that the transfer term comes only from the nearest neighbor. The band dispersion of such a system is given by

$$\varepsilon_{n,\mathbf{k}} = -2t \sum_{i=x,y,z} \cos(ak_i) \simeq ta^2 \sum_{i=x,y,z} k_i^2 + \text{const.} \quad (2.135)$$

By only keeping the second expression of the expansion, we have the effective Hamiltonian.

$$\hat{H} = \sum_{\mathbf{k},\sigma} \varepsilon_{n,\mathbf{k}} c_{\mathbf{k},\sigma}^\dagger c_{\mathbf{k},\sigma} \simeq \left(\frac{R}{2\pi}\right)^3 \int_{-\infty}^{\infty} c_{\mathbf{k},\sigma}^\dagger \left(ta^2 \sum_{i=x,y,z} k_i^2 \right) c_{\mathbf{k},\sigma}. \quad (2.136)$$

Rewriting the equation in the field operator, we obtain the following expression:

$$\begin{aligned}
\hat{H} &= \left(\frac{R}{2\pi}\right)^3 \frac{1}{a^3 R^3} \int_0^R d^3 r \int_0^R d^3 r' \int_{-\infty}^{\infty} d^3 k \exp(i\mathbf{k} \cdot \mathbf{r}) \psi_{\sigma}^{\dagger}(\mathbf{r}) \\
&\quad \left(t a^2 \sum_{i=x,y,z} k_i^2 \right) \exp(-i\mathbf{k} \cdot \mathbf{r}') \psi_{\sigma}(\mathbf{r}') \\
&= \frac{t}{a(2\pi)^3} \int_0^R d^3 r \int_0^R d^3 r' \int_{-\infty}^{\infty} d^3 k \psi_{\sigma}^{\dagger}(\mathbf{r}) \psi_{\sigma}(\mathbf{r}') \exp(i\mathbf{k} \cdot \mathbf{r}) \\
&\quad \left(- \sum_{i=x,y,z} \nabla_{\mathbf{r}'}^2 \right) \exp(-i\mathbf{k} \cdot \mathbf{r}'), \\
&= \frac{t}{a(2\pi)^3} \int_0^R d^3 r \int_0^R d^3 r' \psi_{\sigma}^{\dagger}(\mathbf{r}) \psi_{\sigma}(\mathbf{r}') \left(- \sum_{i=x,y,z} \nabla_{\mathbf{r}'}^2 \right) \\
&\quad \int_{-\infty}^{\infty} d^3 k \exp(i\mathbf{k} \cdot (\mathbf{r} - \mathbf{r}')), \\
&= \frac{t}{a(2\pi)^3} \left(\frac{2\pi}{a}\right)^3 \int_0^R d^3 r \int_0^R d^3 r' \psi_{\sigma}^{\dagger}(\mathbf{r}) \psi_{\sigma}(\mathbf{r}') \left(- \sum_{i=x,y,z} \nabla_{\mathbf{r}'}^2 \right) \delta(\mathbf{r} - \mathbf{r}') \\
&= \frac{t}{a(2\pi)^3} \left(\frac{2\pi}{a}\right)^3 a^3 \int_0^R d^3 r \psi_{\sigma}^{\dagger}(\mathbf{r}) \left(- \sum_{i=x,y,z} \nabla_{\mathbf{r}}^2 \right) \psi_{\sigma}(\mathbf{r}) \\
&= \frac{t}{a} \int_0^R d^3 r \psi_{\sigma}^{\dagger}(\mathbf{r}) \left(- \sum_{i=x,y,z} \nabla_{\mathbf{r}}^2 \right) \psi_{\sigma}(\mathbf{r}) \\
&= \int_0^R d^3 r \psi_{\sigma}^{\dagger}(\mathbf{r}) \left(- \frac{\hbar^2}{2m^*} \sum_{i=x,y,z} \nabla_{\mathbf{r}}^2 \right) \psi_{\sigma}(\mathbf{r}),
\end{aligned} \tag{2.137}$$

where m^* is the effective mass, which can be explicitly described as

$$m^* = \frac{\hbar^2 a}{2t}. \tag{2.138}$$

In general, the effective mass is a tensor; thus, the general effective Hamiltonian is described as

$$\hat{H} = \int_0^R d^3 r \lim_{\mathbf{r} \rightarrow \mathbf{r}'} \sum_{i,j=x,y,z} \nabla_i \psi_{\sigma}^{\dagger}(\mathbf{r}) \left(+ \frac{\hbar^2}{2m^*} \right) \nabla'_j \psi_{\sigma}(\mathbf{r}'). \tag{2.139}$$

2.3.4 Stoner Model

Ferromagnetism can be described in the strong correlation regime, in which the electron–electron repulsion is considered. The stoner model is a mean-field approach in the Hubbard model, in which the exchange splitting in the band

energy is derived from the Hubbard interaction.

Now, let us consider the Hubbard model with $1 < N_e < N$, where N_e and N denote the number of electrons and the number of atomic sites, respectively. The Hamiltonian of the Hubbard model can be expressed as follows:

$$\mathcal{H}_U = U n_{i\uparrow} n_{i\downarrow}, \quad (2.140)$$

where U denotes the Hubbard parameter, and $n_{i,\sigma}$ with $\sigma = \uparrow, \downarrow$ is the occupation number operator. We can define the occupation number operator as

$$\begin{aligned} n_{i\sigma} &\equiv \langle n_{i\sigma} \rangle + (n_{i\sigma} - \langle n_{i\sigma} \rangle) \\ &\equiv \langle n_{i\sigma} \rangle + \delta n_{i\sigma}. \end{aligned} \quad (2.141)$$

By using this definition, the occupation number in Hubbard Hamiltonian can be expressed as

$$\begin{aligned} n_{i\uparrow} n_{i\downarrow} &= (\langle n_{i\uparrow} \rangle + \delta n_{i\uparrow})(\langle n_{i\downarrow} \rangle + \delta n_{i\downarrow}) \\ &= \langle n_{i\uparrow} \rangle \langle n_{i\downarrow} \rangle + \langle n_{i\uparrow} \rangle \delta n_{i\downarrow} + \langle n_{i\downarrow} \rangle \delta n_{i\uparrow} + \delta n_{i\uparrow} \delta n_{i\downarrow} \\ &= \langle n_{i\uparrow} \rangle \langle n_{i\downarrow} \rangle + \langle n_{i\uparrow} \rangle (n_{i\downarrow} - \langle n_{i\downarrow} \rangle) + \langle n_{i\downarrow} \rangle (n_{i\uparrow} - \langle n_{i\uparrow} \rangle) + \delta n_{i\uparrow} \delta n_{i\downarrow} \\ &= \langle n_{i\uparrow} \rangle n_{i\downarrow} + n_{i\uparrow} \langle n_{i\downarrow} \rangle - \langle n_{i\uparrow} \rangle \langle n_{i\downarrow} \rangle + \delta n_{i\uparrow} \delta n_{i\downarrow}. \end{aligned} \quad (2.142)$$

The mean-field theory for the Hubbard model is given by neglecting the fluctuation (correlation) part, which is described in the last term. Thus, the Hubbard Hamiltonian can be written as

$$U n_{i\uparrow} n_{i\downarrow} \simeq U (\langle n_{i\uparrow} \rangle n_{i\downarrow} + n_{i\uparrow} \langle n_{i\downarrow} \rangle - \langle n_{i\uparrow} \rangle \langle n_{i\downarrow} \rangle). \quad (2.143)$$

Let us introduce electron density and spin density as

$$n \equiv \langle n_{i\uparrow} \rangle + \langle n_{i\downarrow} \rangle, \quad (2.144)$$

$$m \equiv \langle n_{i\uparrow} \rangle - \langle n_{i\downarrow} \rangle. \quad (2.145)$$

By using simple algebra, we can rewrite eq.2.143 as

$$\begin{aligned}
Un_{i\uparrow}n_{i\downarrow} &\simeq U(\langle n_{i\uparrow} \rangle n_{i\downarrow} + n_{i\uparrow} \langle n_{i\downarrow} \rangle - \langle n_{i\uparrow} \rangle \langle n_{i\downarrow} \rangle), \\
&= \frac{U}{2}(\langle n_{i\uparrow} \rangle n_{i\downarrow} + n_{i\uparrow} \langle n_{i\downarrow} \rangle) + \frac{U}{2}(\langle n_{i\uparrow} \rangle n_{i\downarrow} + n_{i\uparrow} \langle n_{i\downarrow} \rangle) - U \langle n_{i\uparrow} \rangle \langle n_{i\downarrow} \rangle \\
&= \frac{U}{2}(\langle n_{i\uparrow} \rangle n_{i\downarrow} + n_{i\uparrow} \langle n_{i\downarrow} \rangle + \langle n_{i\uparrow} \rangle n_{i\uparrow} + \langle n_{i\downarrow} \rangle n_{i\downarrow}) \\
&\quad + \frac{U}{2}(\langle n_{i\uparrow} \rangle n_{i\downarrow} + n_{i\uparrow} \langle n_{i\downarrow} \rangle - \langle n_{i\uparrow} \rangle n_{i\uparrow} - \langle n_{i\downarrow} \rangle n_{i\downarrow}) - U \langle n_{i\uparrow} \rangle \langle n_{i\downarrow} \rangle \\
&= \frac{U}{2}(\langle n_{i\uparrow} \rangle + \langle n_{i\downarrow} \rangle)(n_{i\uparrow} + n_{i\downarrow}) - (\langle n_{i\uparrow} \rangle - \langle n_{i\downarrow} \rangle)(n_{i\uparrow} - n_{i\downarrow}) \\
&\quad - U \langle n_{i\uparrow} \rangle \langle n_{i\downarrow} \rangle \\
&\simeq \frac{U}{2}n(n_{i\uparrow} + n_{i\downarrow}) - \frac{U}{2}m(n_{i\uparrow} - n_{i\downarrow}) - U \langle n_{i\uparrow} \rangle \langle n_{i\downarrow} \rangle.
\end{aligned} \tag{2.146}$$

If we consider the Hamiltonian in the matrix form, it can be written as

$$\mathcal{H}_U = \sum_{i,\sigma} \begin{pmatrix} c_{i,\uparrow}^\dagger & c_{i,\downarrow}^\dagger \end{pmatrix} \begin{pmatrix} \frac{U}{2}(n-m) & 0 \\ 0 & \frac{U}{2}(n+m) \end{pmatrix} \begin{pmatrix} c_{i,\uparrow} \\ c_{i,\downarrow} \end{pmatrix} - U \langle n_{i\uparrow} \rangle \langle n_{i\downarrow} \rangle. \tag{2.147}$$

Next, by employing the decoupling approach, we have the effective mean-field Hamiltonian as follows:

$$\mathcal{H}_{MF} = \sum_{\mathbf{k},\sigma} \varepsilon_{\mathbf{k}} c_{\mathbf{k}\sigma}^\dagger c_{\mathbf{k}\sigma} + U \sum_{i,\sigma} \langle n_{i\sigma} \rangle n_{i\sigma} - UN. \tag{2.148}$$

The energy of a mean-field solution defined by

$$|\Psi_{MF}\rangle = \prod_{\varepsilon_{\mathbf{k}} < \varepsilon_{\uparrow}} c_{\mathbf{k}\uparrow}^\dagger \prod_{\varepsilon_{\mathbf{k}'} < \varepsilon_{\downarrow}} c_{\mathbf{k}\downarrow}^\dagger \tag{2.149}$$

with a total spin of $S_z = \frac{1}{2}mN$ is given by

$$\begin{aligned}
E(S_z) &= \langle \Psi_{MF} | \mathcal{H}_{MF} | \Psi_{MF} \rangle \\
&= \sum_{\sigma} \sum_{\varepsilon_{\mathbf{k}} < \varepsilon_{\sigma}} \varepsilon_{\mathbf{k}} + \frac{1}{4}NU(n^2 - m^2),
\end{aligned} \tag{2.150}$$

where the first term representing the kinetic energy increases when $m > 0$, whereas the second interaction term decreases with the exchange for $m > 0$.

2.3.5 Dirac Hamiltonian of Graphene

A carbon atom has six electrons with the electronic configuration in the ground state $1s^2 2s^2 2p^2$, which means that two electrons fill the inner shell $1s$ and the other four occupy the outer shell of the $2s$ and $2p$ orbitals. Because the $2p$ orbitals, which consist of $2p_x$, $2p_y$, and $2p_z$, have roughly 4eV higher energy compared with the $2s$ orbitals, it is energetically favorable to distribute 2 electrons in the $2s$ orbital and the other 2 in the $2p$ orbitals. However, in the presence of other atoms, it is favorable to excite one electron from the $2s$ orbital to the $2p$ orbitals so that the covalent bond can be formed with the other atoms.

Graphene is made of carbon atoms. In graphene, the electron in $1s^2$ is strongly bounded and regarded as core electrons, whereas the other four are regarded as valence electrons. Therefore, two electrons fill the inner shell $1s$, whereas the other electrons fill the outer shell of the $2s$ and $2p$ orbitals. To make a covalent bond between carbon atoms in graphene, one electron from the $2s$ orbital tends to excite to the $2p_z$ orbital. The $2s$ orbital superposes with the $2p_x$ and $2p_y$ orbitals and hybridizes to carry out the so-called sp^2 hybridization. Due to this hybridization, the energy level of the $2p$ orbitals ($2p_x$, $2p_y$, and $2p_z$) are degenerated with the $2s$ orbital. The hybridization also forms the σ bonds with other three carbon atoms, in which those bonds have high stability, leading to the formation of a honeycomb lattice and causing the graphene to become a strong material. Meanwhile, the $2p_z$ orbital is delocalized on the whole graphene layer, which allows conduction of an electrical current. The electronic structure of graphene can be very well described with a tight-binding approximation.

Figure 2.1 presents the crystal structure of graphene, also known as the “honeycomb” structure. It is classified as a two-dimensional hexagonal lattice with two basis atoms per unit cell where, from the figure, the gray shade indicates the unit cell of graphene, or a two-dimensional hexagonal lattice with two sublattices, one for each basis atom, customarily called the A and B sublattices. The two bases are located $r_0 \approx 1.42\text{\AA}$ apart, which corresponds to the C–C bond length in graphene. \mathbf{a}_1 and \mathbf{a}_2 are the lattice basis vectors. Both have the same magnitude of $a = r_0\sqrt{3} \approx 2.46\text{\AA}$. The third lattice basis vector, \mathbf{a}_3 , only exists in graphite, with the magnitude of twice the interlayer spacing between graphene layers $c \approx 3.4\text{\AA}$. In the vector notation, the lattice basis vectors can be expressed as follows:

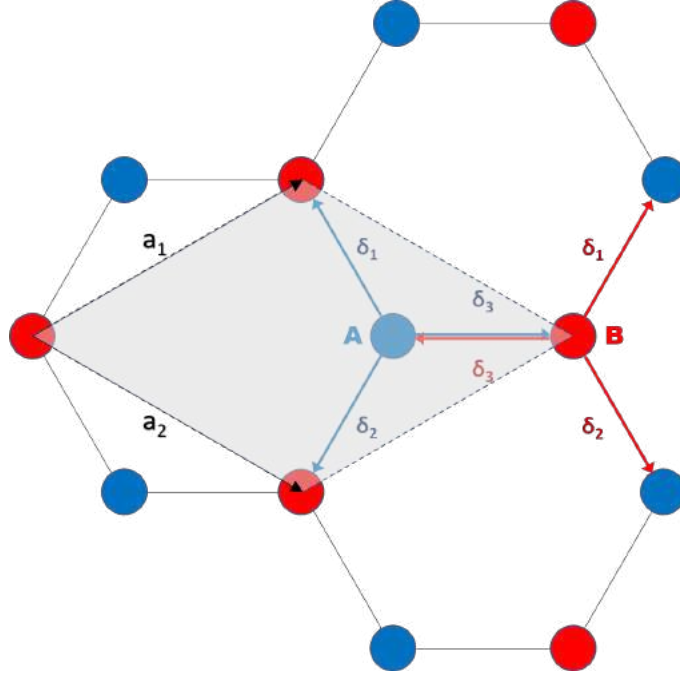


Figure 2.1: Structure crystal of graphene in the real space

$$\begin{aligned}\mathbf{a}_1 &= \left(-\frac{3}{2}a, \frac{\sqrt{3}}{2}a\right), \\ \mathbf{a}_2 &= \left(\frac{3}{2}a, \frac{\sqrt{3}}{2}a\right),\end{aligned}\tag{2.151}$$

while the two reciprocal lattice vectors can be expressed as follows:

$$\begin{aligned}\mathbf{b}_1 &= \left(-\frac{2\pi}{3a}, \frac{2\pi}{\sqrt{3}a}\right), \\ \mathbf{b}_2 &= \left(\frac{2\pi}{3a}, \frac{2\pi}{\sqrt{3}a}\right),\end{aligned}\tag{2.152}$$

The vectors $\vec{\tau}_1$, $\vec{\tau}_2$, and $\vec{\tau}_3$ are the nearest-neighbor vectors, which connect each site on sublattice A to its three nearest neighbors in sublattice B and vice versa. In the vector notation, these nearest-neighbor vectors can be expressed as follows:

$$\begin{aligned}\vec{\tau}_1 &= \frac{a}{2}(-1, \sqrt{3}), \\ \vec{\tau}_2 &= \frac{a}{2}(-1, -\sqrt{3}), \\ \vec{\tau}_3 &= a(1, 0)\end{aligned}\tag{2.153}$$

Now, we assume that the electron in the p_z orbital of carbon atoms in graphene can only hop to their nearest neighbors. The carbon atoms in graphene have three nearest-neighbors, which are three carbon atoms for both sublattice A and sublattice B; therefore, the hopping parameters for both sublattices are the same, $t_{ij} = -t$. Using the formalism of the second quantization, the Hamiltonian for graphene within the tight-binding approximation in the real space can be written as follows:

$$\hat{H} = -t \sum_{\langle i,j \rangle, \sigma} (c_{A,j+\tau_i, \sigma}^\dagger c_{B,j, \sigma} + c_{B,j+\tau_i, \sigma}^\dagger c_{A,j, \sigma}). \quad (2.154)$$

Here, t is the nearest-neighbor hopping parameter (in units of eV), $c_{A,j+\tau_i, \sigma}^\dagger$ is the creation operator for the $2p_z$ electrons with spin σ on site $j + \tau_i$ in sublattice A, $c_{A,j, \sigma}$ is the annihilation operator for $2p_z$ electrons with spin σ on site j in sublattice A, $c_{B,j+\tau_i, \sigma}^\dagger$ is the creation operator for $2p_z$ electrons with spin σ on site $j + \tau_i$ in sublattice B, and $c_{B,j, \sigma}$ is the annihilation operator for $2p_z$ electrons with spin σ on site j in sublattice B.

Because of the periodicity of the graphene crystal structure, equation 2.154 can be Fourier-transformed into the momentum space simplified by using equation 2.109, 2.110, and 2.112 as follows:

$$\hat{H} = -t \sum_{\mathbf{k}, \sigma} \left(\sum_i e^{i\mathbf{k} \cdot \tau_i} \right) (c_{A, \mathbf{k}, \sigma}^\dagger c_{B, \mathbf{k}, \sigma} + c_{B, \mathbf{k}, \sigma}^\dagger c_{A, \mathbf{k}, \sigma}) \quad (2.155)$$

By transforming equation 2.155 into matrix form, the tight-binding Hamiltonian of graphene becomes

$$\hat{H} = \sum_{\mathbf{k}, \sigma} \begin{pmatrix} c_{A, \mathbf{k}, \sigma}^\dagger & c_{B, \mathbf{k}, \sigma}^\dagger \end{pmatrix} \begin{pmatrix} 0 & \varepsilon_{\mathbf{k}}^* \\ \varepsilon_{\mathbf{k}} & 0 \end{pmatrix} \begin{pmatrix} c_{A, \mathbf{k}, \sigma} \\ c_{B, \mathbf{k}, \sigma} \end{pmatrix} \quad (2.156)$$

where $\varepsilon_{\mathbf{k}}$ is given by

$$\varepsilon_{\mathbf{k}} = -t \left[e^{ik_x a} + e^{-i\frac{k_x a}{2} - i\frac{\sqrt{3}k_y a}{2}} + e^{-i\frac{k_x a}{2} + i\frac{\sqrt{3}k_y a}{2}} \right] \quad (2.157)$$

By diagonalizing the Hamiltonian, we have

$$H = \sum_{\mathbf{k}, \sigma} (E_{\mathbf{k}}^- c_{v\mathbf{k}\sigma}^\dagger c_{v\mathbf{k}\sigma} + E_{\mathbf{k}}^+ c_{c\mathbf{k}\sigma}^\dagger c_{c\mathbf{k}\sigma}) \quad (2.158)$$

with the eigenvalues:

$$E_{\mathbf{k}}^{\pm} = \pm t \sqrt{3 + 2 \cos \left(\frac{3}{2} k_x a + \frac{\sqrt{3}}{2} k_y a \right) + 2 \cos \left(\frac{3}{2} k_x a - \frac{\sqrt{3}}{2} k_y a \right) + 2 \cos (\sqrt{3} k_y a)}. \quad (2.159)$$

Thus, we have the conduction band E^+ and the valence band E^- where at each \mathbf{k} -point, we only have two bands.

Two special high-symmetry points, \mathbf{K} and \mathbf{K}' , shown in fig.2.1, can be mathematically written as follows:

$$\mathbf{K} = \frac{2}{3} \mathbf{b}_2 - \frac{1}{3} \mathbf{b}_1 = \left(\frac{2\pi}{3a}, \frac{2\pi}{3\sqrt{3}a} \right), \quad (2.160)$$

$$\mathbf{K}' = \frac{1}{3} \mathbf{b}_2 - \frac{2}{3} \mathbf{b}_1 = \left(\frac{2\pi}{3a}, -\frac{2\pi}{3\sqrt{3}a} \right). \quad (2.161)$$

For $\mathbf{k} = \mathbf{K} + \mathbf{k}'$ with $|\mathbf{k}'| \ll \frac{\pi}{a}$,

$$\begin{aligned} E_{\mathbf{k}}^{\pm} &= \pm t \sqrt{3 + 2 \cos \left(\frac{3}{2} k_x a + \frac{\sqrt{3}}{2} k_y a \right) + 2 \cos \left(\frac{3}{2} k_x a - \frac{\sqrt{3}}{2} k_y a \right) + 2 \cos (\sqrt{3} k_y a)} \\ &= \pm t \sqrt{\frac{9}{4} (k'_x)^2 a^2 + \frac{9}{4} (k'_y)^2 a^2} \\ &= \pm \frac{3}{2} t |\mathbf{k}'| a. \end{aligned} \quad (2.162)$$

A similar assumption is also applicable for the \mathbf{K}' point. Meanwhile, for $\mathbf{k} = \mathbf{K}$ and $\mathbf{k} = \mathbf{K}'$, $E_{\mathbf{K}}^{\pm} = E_{\mathbf{K}'}^{\pm} = 0$, showing that there is no gap at the \mathbf{K} and \mathbf{K}' . These results indicate that the energy bands form two circular cones around these two \mathbf{k} -points, connected one with the other at their extreme. This energy band is called the Dirac cone. Due to these cones, the electrons in the graphene behave in a peculiar manner, and they all have the same velocity and absolutely no inertia. It is as if they have no mass, similar to what the theory of relativity predicts for a particle traveling at the speed of light, except that the velocity is about 1/300 of the light velocity.

Now, we want to take the continuum limit into graphene and make an effective continuum Hamiltonian from it. At first, let us start from eq.2.157, where for $\mathbf{k} = \mathbf{K} + \mathbf{k}'$ with $|\mathbf{k}'| \ll \frac{\pi}{a}$; we have

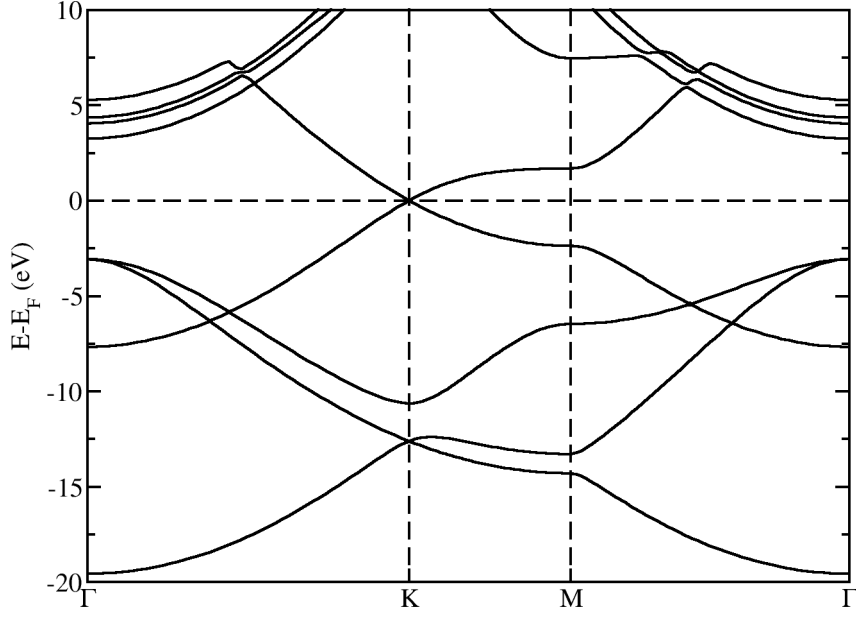


Figure 2.2: energy bands of graphene

$$\begin{aligned}
-\frac{1}{t}\varepsilon_{\mathbf{k}} &= \exp\left(ia\left(\frac{2\pi}{3a} + k'_x\right)\right) + \exp\left(-i\left\{\frac{a}{2}\left(\frac{2\pi}{3a} + k'_x\right) + \frac{\sqrt{3}a}{2}\left(\frac{2\pi}{3\sqrt{3}a} + k'_y\right)\right\}\right) \\
&\quad + \exp\left(-i\left\{\frac{a}{2}\left(\frac{2\pi}{3a} + k'_x\right) - \frac{\sqrt{3}a}{2}\left(\frac{2\pi}{3\sqrt{3}a} + k'_y\right)\right\}\right) \\
&= -\frac{3}{2}\frac{1}{i}\omega(k'_x - k'_y).
\end{aligned} \tag{2.163}$$

Here, we have $\omega = \exp(2\pi i/3)$. Next, let us introduce a gauge transformation as $\bar{c}_{B,\mathbf{k},\sigma}^\dagger = \omega^{-1}c_{B,\mathbf{k},\sigma}^\dagger$ from which we define another operator $d_{a,\eta,\sigma}^\dagger$ as

$$\begin{aligned}
d_{A,R,\sigma}^\dagger(\mathbf{k}') &= c_{A,\mathbf{K}+\mathbf{k},\sigma}^\dagger, & d_{B,R,\sigma}^\dagger(\mathbf{k}') &= c_{B,\mathbf{K}+\mathbf{k},\sigma}^\dagger \\
d_{A,L,\sigma}^\dagger(\mathbf{k}') &= c_{A,\mathbf{K}+\mathbf{k},\sigma}^\dagger, & d_{B,L,\sigma}^\dagger(\mathbf{k}') &= c_{B,\mathbf{K}+\mathbf{k},\sigma}^\dagger
\end{aligned} \tag{2.164}$$

where from here, we have two flavors; \mathbf{R} (\mathbf{L}) denotes the \mathbf{k} near \mathbf{K} (\mathbf{K}'). Because we can make \mathbf{k}' a continuum variable, we can assume that $d_{a,\eta,\sigma}^\dagger$ is a continuum Dirac field. From it, we can have an effective Hamiltonian density $\mathcal{H} = H/(\text{the number of unit cells})$ for $|\mathbf{k}'| \ll \frac{\pi}{a}$ as

$$\mathcal{H} = \frac{3t}{2i} \sum_{\eta,\sigma} \int \frac{d^2k}{(2\pi^2)} \begin{pmatrix} d_{A,\eta,\sigma}^\dagger(\mathbf{k}) & d_{B,\eta,\sigma}^\dagger(\mathbf{k}) \end{pmatrix} \begin{pmatrix} 0 & k_x - ik_y \\ k_x - ik_y & 0 \end{pmatrix} \begin{pmatrix} d_{A,\eta,\sigma}(\mathbf{k}) \\ d_{B,\eta,\sigma}(\mathbf{k}) \end{pmatrix}, \quad (2.165)$$

where $\eta = R, L$ denotes the flavor. From the equation, we have the k -dependent submatrix of the Hamiltonian as

$$\mathcal{H}_k = \begin{pmatrix} 0 & k_x - ik_y \\ k_x + ik_y & 0 \end{pmatrix} = \vec{\sigma} \cdot \mathbf{k}. \quad (2.166)$$

2.3.6 Bandgap Opening on the Graphene Dirac Cone

From the previous section, the Dirac cone of graphene comes from the chiral symmetry of graphene in which the equipotential between carbon atoms in sublattice A and sublattice B is preserved. In the presence of potential difference 2Δ between the A and B sites, the chiral symmetry is broken, and the Hamiltonian becomes

$$\mathcal{H}_k = \begin{pmatrix} \Delta & k_x - ik_y \\ k_x + ik_y & -\Delta \end{pmatrix} \quad (2.167)$$

This kind of potential asymmetry can arise when graphene grows on the top of a certain substrate where the covalent bond is formed between the graphene and the substrate. One of the cases is when graphene grown on a SiC substrate resulting band gap of 250 meV [62]. By using a similar approach as above, taking the k -points near to the \mathbf{K} and \mathbf{K}' points, the energy band becomes

$$E_{\mathbf{k}}^\pm = \pm \sqrt{|\mathbf{k}^2| + \Delta^2}, \quad (2.168)$$

resulting mass gap opens in the Dirac cone.

In the case of graphene on the top of the magnetic substrate such as nickel (Ni), the covalent bonds are formed between the d_{z^2} orbital of Ni atoms with the p^z orbital of carbon atoms either in sublattice A or sublattice B. This covalent bond leads to the potential asymmetry between sublattices A and B, opening the mass gap of the graphene Dirac cone. Furthermore, due to the covalent bonds, the charge transfer occurs from the Ni to C atoms, inducing a magnetic moment on the carbon atom. The magnetic moment of the C atoms that form a covalent bond with the Ni atoms have opposite direction with the magnetic moment of the Ni atoms. It originates from the interaction between

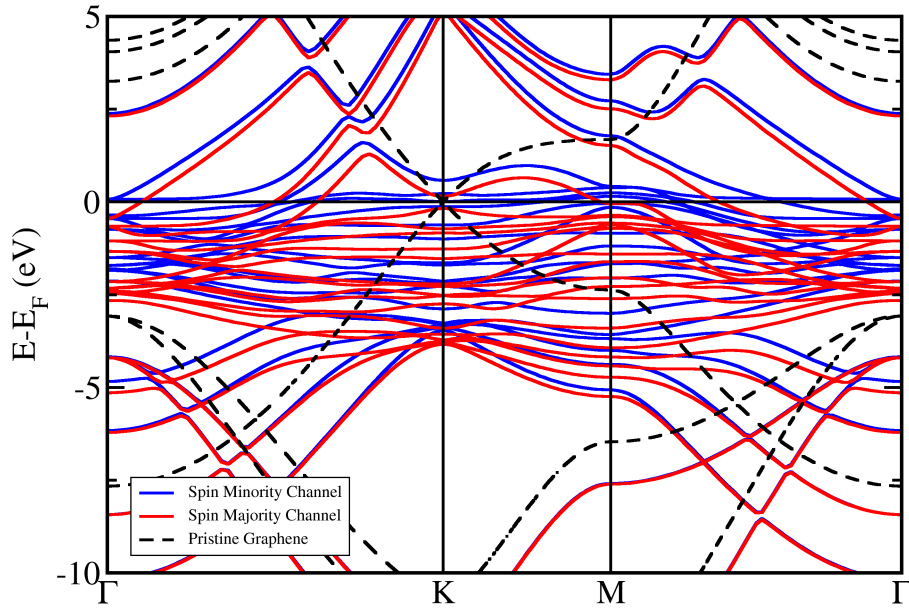


Figure 2.3: Band structure of graphene on the top Ni substrate.

the d_{z^2} orbital of the Ni atoms and the p^z orbital of the C atoms, resulting in the formation of the bonding and antibonding states. In the case of the majority-spin channel, the bonding and antibonding states are occupied due to the Stoner gap, and the net effect would be an energy cost. However, the filled d_{z^2} orbital gains little energy by repelling the empty p^z orbital of the C atoms, resulting in an antiferromagnetism configuration [63]. The magnetic moment in the carbon atom sublattice A is in the opposite direction of sublattice B due to the half-filled p^z orbital and Pauli's exclusion principle. This rule is often found in organic molecules in sp^2 hybridization or magnetic alternant hydrocarbon systems.

The potential difference Δ in eq.2.167 for the case of graphene growing on the top of a magnetic substrate comes from the covalent bond and the opposite direction of the induced magnetic moment on the carbon atoms in sublattices A and B. Let us introduce the addition of potential energy due to the bond formation in one of the sublattices as \mathcal{V} . On the other hand, we recall the Stoner model Hamiltonian to describe the potential difference due to the induced magnetic moment on graphene. Thus, the total effective Hamiltonian can be described as follows:

$$\mathcal{H}_{\mathbf{k},\sigma} = \begin{pmatrix} \mathcal{V}_{A\uparrow} + I \langle n_{A\downarrow} \rangle & k_x - ik_y & 0 & 0 \\ k_x + ik_y & I \langle n_{B\downarrow} \rangle & 0 & 0 \\ 0 & 0 & \mathcal{V}_{A\downarrow} + I \langle n_{A\uparrow} \rangle & k_x - ik_y \\ 0 & 0 & k_x - ik_y & I \langle n_{B\uparrow} \rangle \end{pmatrix}, \quad (2.169)$$

where I is a Stoner interatomic exchange parameter. Here, we assume that the covalent bond is formed between the C atoms in the sublattice A with the Ni atoms. Both contributions on the potential difference Δ leading to the opening mass gap of the Dirac cone and resulting spin-polarized band structure as shown in figure.2.3. In this thesis, we will present a study on the control of the opening of mass gap in the Dirac cone and preservation of the Dirac cone of graphene in graphene-based magnetic junction.

This page intentionally left blank

Chapter 3

COMPUTATIONAL APPROACHES

3.1 Theoretical Framework

In this thesis, we propose a way to control the opening and closing of graphene's mass-gapped Dirac cone (MGDC). The first graphene-based magnetic junction proposed is Ni/graphene/Ni nano-spin-valve-structure. This proposal comes from the fact discussed in the previous section where the MGDC of graphene is open when graphene is placed on the Ni substrate due to the formation of the covalent bond by pd-hybridization of p_z -orbital of C atoms and d_{z^2} -orbital of Ni atoms. The pd-hybridization occurs between Ni atoms and C atoms of either sublattice A or B leading to the potential difference between sublattice A and B, resulting in broken chiral symmetry of graphene. Thus, if a Ni/graphene/Ni nano-spin-valve structure where Ni atoms of the upper and lower Ni slabs at the interfaces are hybridized with different graphene sublattices is considered, the chiral symmetry could be preserved. In other words, Ni atoms from the lower Ni(111) slab hybridized with C atoms in sublattice A (i.e., C_A), and Ni atoms from the upper Ni(111) slab hybridized with C atoms in sublattice B (i.e., C_B), thus no potential difference between sublattice A and B which comes from chemical bonding to be expected. Although the C atoms of graphene bond with the Ni atoms, this unique hybridization preserves the equipotential between sublattices A and B. Therefore, we can modify eq.2.169 as follows

$$\mathcal{H}_{\mathbf{k},\sigma} = \begin{pmatrix} \mathcal{V}_{A\uparrow} + I \langle n_{A\downarrow} \rangle & k_x - ik_y & 0 & 0 \\ k_x + ik_y & \mathcal{V}_{B\uparrow} + I \langle n_{B\downarrow} \rangle & 0 & 0 \\ 0 & 0 & \mathcal{V}_{A\downarrow} + I \langle n_{A\uparrow} \rangle & k_x - ik_y \\ 0 & 0 & k_x + ik_y & \mathcal{V}_{B\downarrow} + I \langle n_{B\uparrow} \rangle \end{pmatrix}, \quad (3.1)$$

where $\mathcal{V}_{A\sigma} = \mathcal{V}_{B\sigma}$. Since, in the Gr-Ni system, the induced magnetic moment appears on graphene due to charge transfer from Ni atoms to C atoms, we expect similar phenomena for our case. However, here we have two ferromagnetic slabs, which are upper and lower Ni slabs, where two different magnetic alignments can occur between upper and lower Ni, *i.e.*, parallel and antiparallel alignments.

In the case of the antiparallel configuration (APC), the induced magnetic moment occurs in C_A and C_B with the alignment corresponding to Ni slabs with which the C atoms form bonding. For the example, the lower (upper) Ni slab has the upward (downward) direction of magnetic alignment and forms a covalent bond with C atoms of sublattice A (B). Thus, C_A and C_B have magnetic moments, which are the same in their magnitude but in the opposite direction. Therefore, for antiparallel alignment, we have the following relation:

$$m_A = -m_B \rightarrow \langle n_{A\downarrow} \rangle = \langle n_{B\uparrow} \rangle > \langle n_{A\uparrow} \rangle = \langle n_{B\downarrow} \rangle. \quad (3.2)$$

The inequality above implies the broken chiral symmetry of graphene. Thus, opening MGDC of graphene is to be expected. However, the band dispersion of graphene is not spin-polarized due to an equivalent amount of the moment size for both upward and downward directions.

Meanwhile, in the case of parallel alignment, both upper and lower Ni slabs have the same direction of magnetic alignment. Thus, by supposing both upper and lower Ni slabs have magnetic alignment in the upward direction, we have the following relation:

$$m_A = m_B \rightarrow \langle n_{A\downarrow} \rangle = \langle n_{B\downarrow} \rangle > \langle n_{A\uparrow} \rangle = \langle n_{B\uparrow} \rangle. \quad (3.3)$$

The inequality above implies perseverance of the chiral symmetry of graphene. However, the Dirac cone of graphene is spin-polarized due to the net spin polarization. Thus, a closing graphene's MGDC with spin-polarized bandstructure is expected.

A similar explanation is expected for Ni/hBN-graphene-hBN/Ni and Ni/X-graphene-X/Ni (with X = H, O, P, S, F, N) nano-spin-valve structure. However, chemical bonding was not created between Ni and graphene for those two nano-spin-valve structures. Therefore, instead of inducing the magnetic moment of graphene through charge transfer as proposed in Ni/graphene/Ni, the induced magnetic moment is introduced through the magnetic proximity effect. The surface state of d_{z^2} -orbital of Ni atoms at the interface works on the p_z -orbital of C atoms or π -orbital of graphene. By changing the potential which comes from chemical bonding $\mathcal{V}_{\eta\sigma}$ into proximity effect of Ni surface state acts on C atoms $\nu_{\eta\sigma}$, the matrix in Eq. 3.1 can be rewritten as follows:

$$\mathcal{H}_{\mathbf{k},\sigma} = \begin{pmatrix} \nu_{A\uparrow} + I \langle n_{A\downarrow} \rangle & k_x - ik_y & 0 & 0 \\ k_x + ik_y & \nu_{B\uparrow} + I \langle n_{B\downarrow} \rangle & 0 & 0 \\ 0 & 0 & \nu_{A\downarrow} + I \langle n_{A\uparrow} \rangle & k_x - ik_y \\ 0 & 0 & k_x + ik_y & \nu_{B\downarrow} + I \langle n_{B\uparrow} \rangle \end{pmatrix}, \quad (3.4)$$

represents the effective Hamiltonian of graphene in Ni/hBN-graphene-hBN/Ni and Ni/X-gr-X/Ni nano-spin-valve structure.

Transmission probability calculation was done on Ni/graphene/Ni nano-spin-valve structure to understand the efficiency of controllable graphene's MGDC to its IMR ratio. The spin-dependent current was calculated using the Landauer-Buttiker given by:

$$I^{\uparrow(\downarrow)} = \frac{e}{h} \int_{\min\infty}^{\infty} T^{\uparrow(\downarrow)}(E) [f_L(E, \mu) - f_R(E, \mu)] dE \quad (3.5)$$

where $f_L(E, \mu)$ ($f_R(E, \mu)$) is the right (left) moving electron injected from the left (right) lead in the form of the Fermi-Dirac function. μ_L (μ_R) denotes the chemical potentials of the left (right) electrodes. Since zero-bias voltage was considered, thus $\mu_L = \mu_R = E_F$. In addition, the ballistic transmission T as a function of energy E is described with respect to the Green's function form as

$$T^{\uparrow(\downarrow)}(E) = \text{Tr} \left\{ \left[\Gamma_L G^R \Gamma_R G^A \right] \right\} \quad (3.6)$$

where Γ_L (Γ_R) is the coupling matrix of the left (right) electrode, G^R (G^A) is the retarded (advanced) Green's functions of the central region.

On the other hand, for the case of calculation of transmission probability

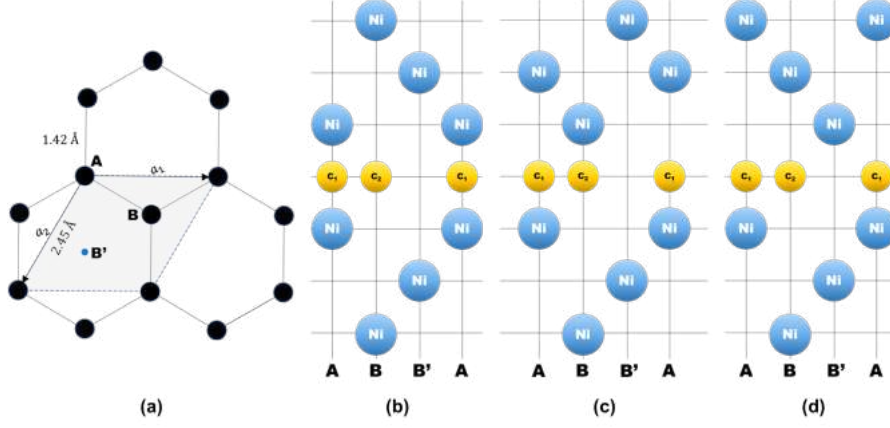


Figure 3.1: Model crystal structures of Ni/graphene/Ni systems. In the left panel (a), the top view of the graphene is depicted. While the proposed model crystal structures of the 3-layer Ni/graphene/3-layer Ni are shown in the (b) AA-stacking structure, (c) BA-stacking structure, and (d) B'A-stacking structure, where the stacking sequences from the graphene to the upper Ni slab are different from one another.

when CPP geometry is considered in chapter 6, the transmission matrix is described as follows:

$$T(E) = \sum_{\mathbf{k}_{\parallel}} \sum_{i,j} T_{i,j}(\mathbf{k}_{\parallel}, E), \quad (3.7)$$

where $T_{i,j}(\mathbf{k}_{\parallel}, E)$ is the probability of electrons with energy E and momentum k to move from the i -th Bloch state to the j -th Bloch state. $T(E)$ is obtained by summing over the 2D Brillouin zone and all incoming-outcoming states.

Finally, the MR ratio can be calculated by including the difference between the current in the APC and PC states and then dividing it by the current in the APC state as follows:

$$\text{MR ratio} = \frac{I_{PC} - I_{APC}}{I_{APC}} \times 100\%. \quad (3.8)$$

The computational approach and the structure model for each spin-valve structure will be explained in detail in the next section. The parameter and configuration for calculating transmission probability will also be introduced in the next section.

3.2 Model and Computational Strategy

3.2.1 Model of Ni/graphene/Ni spin-valve structure

The DFT-spin-GGA calculations were done using the Quantum ESPRESSO package [64]. Previous study reported that the original Perdew–Burke–Ernzerhof (PBE) [65] functional determines wrongly the interlayer distance between the graphene and the nickel layer at the interfaces in the most stable structure of Ni/graphene system [66]. Therefore, the revised Perdew–Burke–Ernzerhof functional, called the PBEsol [67] functional within the generalized gradient approximation (GGA), was used due to its consistency with experimental results in determining the interlayer distance. Ultrasoft pseudopotentials [61] were used to describe the electron–ion interaction. A kinetic energy cutoff of 50 Ry was used for wavefunctions to obtain a good convergence calculation. Since an appropriate k-point grid determined the convergence of the total energy calculation in this system, a k-point grid of $24 \times 24 \times 1$ was used for all calculations.

The adsorption of the graphene layer on the top of Ni(111) has four possible structural stacking arrangements: (i) top/fcc-stacking–carbon atoms of graphene are placed on top of the first and third layers of Ni(111), (ii) top/hcp stacking–carbon atoms of graphene are placed on top of the first and second layers of Ni(111), (iii) hollow-stacking–carbon atoms of graphene are placed on top of the second and third layers of Ni(111), while the hollow site of graphene is placed on top of the first layer of Ni(111), (iv) bridge-stacking–bridge-site between two carbon atoms is placed on top of the first layer of Ni(111) [68,69].

The consistency of the PBEsol functional in determining the most stable stacking arrangement and the interlayer distance between graphene and Ni(111) slab was verified by calculating the total energy of the Ni/graphene system using the four different stacking arrangements and compare the interlayer distance of the lowest total energy structure with previous experimental and theoretical studies. The result demonstrated that the top/fcc-stacking was the lowest energy state in comparison with the top/hcp-, hollow-, and bridge-stacking by 25.9, 122.0, and 226.4 meV, respectively. Meanwhile, the interlayer distance between graphene and Ni(111) slab of top/fcc-stacking was 2.08 Å. This result is in agreement with previous experimental and theoretical studies which reported top/fcc-stacking as the most stable structure with interlayer distance ~ 0.21 nm [66,68–70]. However, although the top/fcc-stacking is the most preferable structure, the difference between top/fcc and top/hcp is small

enough to allow both configurations to occur.

Furthermore, the necessity of using van der Waals interaction in the calculation was verified by calculating the interlayer distance of the most stable structure, i.e., top/fcc-stacking, and comparing it with the calculation done without the inclusion of the van der Waals interaction. It was found that the interlayer distance difference was only 0.02 Å, where the interlayer distances with the van der Waals interaction was 2.10 Å. Although the interlayer distance with the inclusion of the van der Waals interaction was closest to the previous experimental studies, the small interlayer distance difference implies that the bonding between the nickel slab and graphene mainly comes from pd hybridization. Therefore, the contribution of the van der Waals interaction is omitted in this study, and the main focus is placed on the covalent bond that comes from the pd hybridization of nickel atoms with carbon atoms.

The precise stacking arrangement of the Ni/graphene/Ni system has not yet been fully understood; the stacking of the Ni overlayer (slab) above the graphene must be verified. Since a relevant atomic configuration should usually be energetically lower than the others, this study proposes three different arrangements of structural stacking for the upper part of the Ni/graphene interface, while top/fcc-stacking is determined for the lower part of the Ni/graphene by considering the most stable structural arrangement as shown in Fig. 3.1. The three different stacking arrangements are (i) AA-stacking, for which the first (third) layer of the upper Ni slab is placed on top of the A-site (B-site) carbon atoms of graphene, (ii) B'A-stacking, for which the first (second) layer of the upper Ni slab is placed on top of the B-site (A-site) carbon atoms of graphene, and (iii) BA-stacking, for which the second (third) layer of the upper Ni slab is placed on top of the B-site (A-site) carbon atoms of graphene.

In the model structure, a vacuum space of at least 30 Å was inserted to avoid spurious interactions between the slab replicas. At first, the case of a three-layer nickel sandwich graphene layer was investigated. Then, the thickness of the nickel layers was varied from 1 to 6. To understand the magnetic configuration of the system, two initial magnetic configurations were set between the two nickel slabs: (i) anti-parallel configuration, for which the total magnetic moment of the upper and lower nickel slabs have an anti-parallel alignment, and (ii) parallel configuration, for which the total magnetic moment of the upper and lower nickel slabs have a parallel alignment. The total energies of the in-plane and out-of-plane magnetization directions were compared by adopting the noncollinear magnetism calculation with spin-orbit interac-

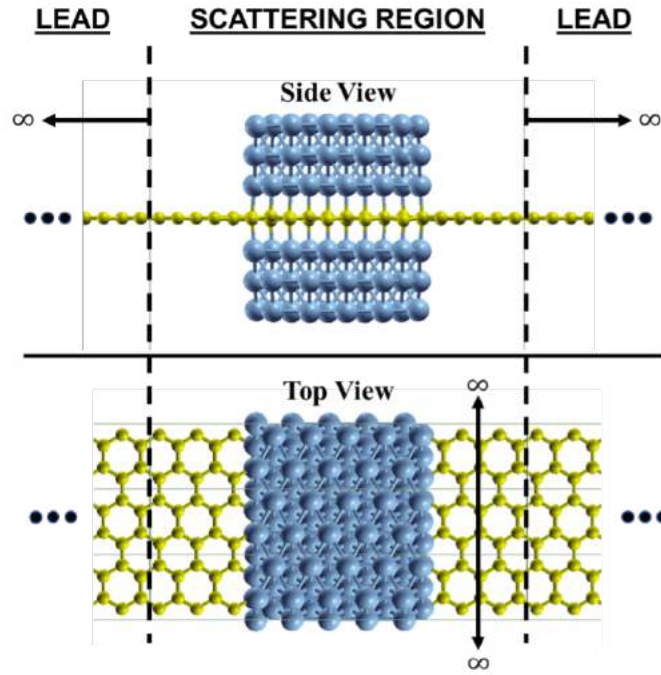


Figure 3.2: Proposed system of graphene where the middle part is sandwiched by Ni(111) nanostructures. The most stable stacking arrangement from our previous study was considered²⁴. The graphene is used as a buffer and electrode.

tion terms. The in-plane magnetization direction was found to have an energy lower by only 1 meV. However, since this study considers the functionality of in-plane conductance switching of graphene depending on the external magnetic field, the out-of-plane magnetization direction was chosen so that the anti-parallel and parallel of the Ni slabs could be controlled easily.

3.2.2 Model of Ni/graphene/Ni nano-spin-valve structure for IMR Calculation

For the calculation of in-plane conductance of graphene which is represented by transmission probability, Ni(111) nanostructures with three Ni atoms layer thickness and an atomic-scale width of $\sim 12.08 \text{ \AA}$ was considered, as shown in Figure 3.2. The three Ni atoms layer thickness of Ni (111) nanostructures is considered because later in chapter 4, it suggests that three Ni atoms layer thickness is representable enough for thicker Ni(111) nanostructure by exhibiting same physics at the interface. The finite size width of $\sim 12.08 \text{ \AA}$ for Ni(111) nanostructures was considered for understanding the effectiveness of the in-plane magnetoresistance of graphene created from the Ni/graphene/Ni magnetic junctions. Wider Ni(111) nanostructure, e.g., width in nanometer

scale, is expected to exhibit high performance. Here, graphene was used as the buffer layer and electrodes in the calculation. The most stable stacking arrangement which has determined later in chapter 4 is considered, where Ni atoms at the interfaces of the lower and upper Ni(111) slabs hybridized with C atoms in sublattices A and B, respectively. Both APC and PC were considered for Ni(111) nanostructures.

A spin-polarized plane-wave-based DFT calculations were performed using the Quantum ESPRESSO package [64] to obtain the structural equilibrium and spin-charge density properties of the proposed system. Furthermore, we described the electron-ion interaction using a revised Perdew-Burke-Ernzerhof functional for a densely packed solid surface (i.e., PBESol functional) [67] and ultrasoft pseudopotentials [61] within the generalized gradient approximation (GGA). From the result of studies in chapter 4, the PBESol pseudopotential is essential to successfully achieve the interlayer distance between Ni slabs and graphene, which is consistent regardless the thickness of Ni slabs and agrees with experimental study. This interlayer distance at the interface is important because it determine the electronic state at the interface. The atomic positions were relaxed, with a total force tolerance of $0.001 \text{ eV}/\text{\AA}$. A $45 \times 45 \times 1$ Monkhorst-Pack k-mesh was used for calculations. First-principles quantum transport calculations, which coupled DFT with the nonequilibrium Green's function, were performed using the Siesta and Transiesta packages [71–74] to calculate the transport properties at a zero-bias voltage.

For the transmission probability calculation, the PBESol functional and Troullier-Martins pseudopotential [75] were used within GGA. A double-zeta plus polarization basis set [76–78] was employed, and the temperature was set to 300 K. A perpendicular k-point of 1×901 with respect to the transmission direction was considered to obtain a good accuracy for the transmission probability.

3.2.3 Model of Ni/nhBN/Ni and Ni/hBN-graphene-hBN/Ni magnetic junctions

After successfully controlling the graphene's MGDC and getting colossal IMR ratio as discussed later in chapter 4 and 5, respectively, optimization to create a successful design of a graphene-based spin-valve structure spintronics device need to be performed. The optimization was needed for realization of the actual device and for ensuring a performance comparable to that predicted in this theoretical study. The chemical bonding between the Ni slabs and

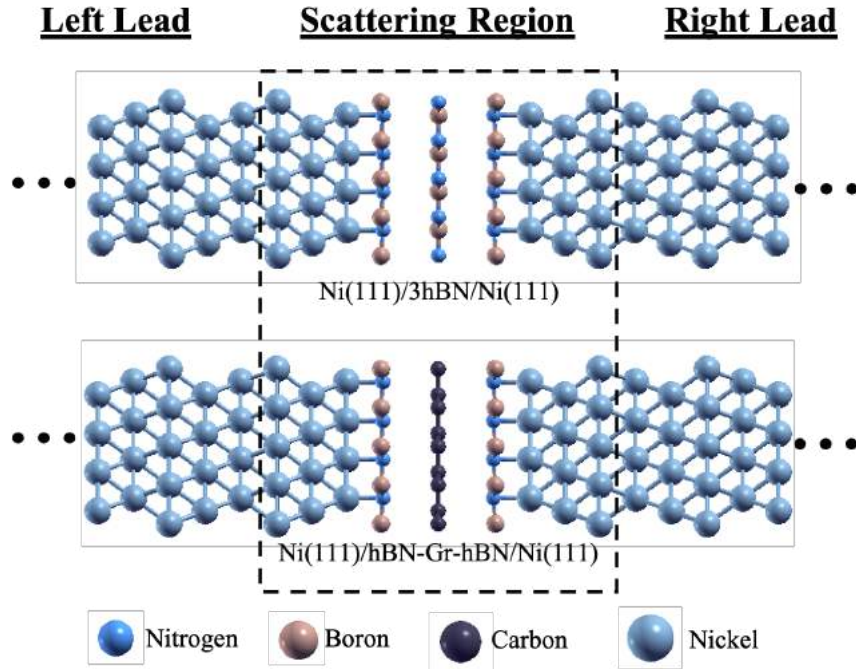


Figure 3.3: Side view of the supercell of Ni(111)/3hBN/Ni(111) (as representative of few-layer hBN MTJ) and Ni(111)/hBN-Gr-hBN/Ni(111) used to represent the scattering region and lead corresponding to model calculation for transmission probability calculation.

graphene in Ni/graphene/Ni needs to be perfect to get control on graphene's MGDC. This perfect surface can be realized experimentally; however, it is relatively difficult. Thus, to avoid a complete change in the IMR of graphene due to a defect at the Ni/graphene interface, a barrier is necessary to maintain the graphene Dirac cone, although some defect occurs on the Ni surface. Furthermore, the barrier will also optimize the controllability of graphene's Fermi energy.

For the above purpose, hBN layer can be introduced between the graphene layer and Ni slabs. However, when the hBN layer is introduced between Ni slabs and graphene, the controllable induced magnetic moment on graphene replaced from through charge transfer to through magnetic proximity effect. Thus, a theoretical study is conducted to understand the origin of the magnetic proximity effect. At first, Ni/nhBN/Ni magnetic junctions were investigated with $n = 2, 3, 4,$ and 5 . After that, the investigation was done on Ni/hBN-graphene-hBN/Ni magnetic junction.

For the investigation, spin-polarized plane wave-based density functional theory (DFT) calculations were performed using the Quantum ESPRESSO package [64, 79]. A revised Perdew-Burke-Ernzerhof (PBE) functional for a

densely packed solid surface, called the PBEsol functional [67], as well as ultrasoft pseudopotentials [61], within the generalized gradient approximation (GGA) were used to describe the electron-ion interaction. A kinetic energy cut-off of 50 Ry was used for the wavefunctions to reach a good convergence calculation. Since adopting an appropriate k-point grid can result in the convergence of the total energy calculation in this system, a k-point grid of $24 \times 24 \times 1$ was chosen for all calculations. Furthermore, the effect of the van der Waals interactions on the electronic structures was included by applying the most recent and accurate DFT-D3 corrections [80]. Taking into account the van der Waals interactions in the DFT calculations, the average interlayer distance of Ni-hBN and hBN-hBN are 2.05 Å and 3.13 Å, respectively. These results are close to experimental values, which is 1.87 ± 0.12 Å for Ni-hBN distance in hBN/Ni system [81] and 3.33 Å for hBN-hBN distance in hBN bulk [82].

The ballistic transmission probability calculations were performed using the Landauer-Buttiker formalism [83, 84]. The left lead, right lead, and scatterer regions were considered in the model calculation, as shown in Fig. 3.3 Ni(111) was considered for the left and right leads to reduce the computational cost without neglecting any important physics. However, the use of Au(111) as a lead carrying normal input/output currents for the Ni/hBN/Ni and Ni/hBN-Gr-hBN/Ni structure would be expected in an actual device. The transmission probability calculations were performed using the PWCOND [85] module of the Quantum ESPRESSO software. A perpendicular k-point of 50×50 with respect to the transmission direction was considered to obtain good accuracy of the transmission probability. The PWCOND module calculates the transmission probability at zero temperature.

3.2.4 Model of Ni/hBN-graphene-hBN/Ni spin-valve structure for investigating the possibility on controlling MGDC

After understanding the origin of proximity effect on the 2D materials tunnel barrier, further study was performed to understand the effectivity of proximity effect on controlling MGDC of graphene. Fig. 3.4 shows a graphene layer sandwiched with hBN and followed by Ni(111) slabs in this theoretical study. The most stable stacking configuration between Ni(111) and hBN was considered, with Ni atoms at the interface hybridizing with N atoms of hBN

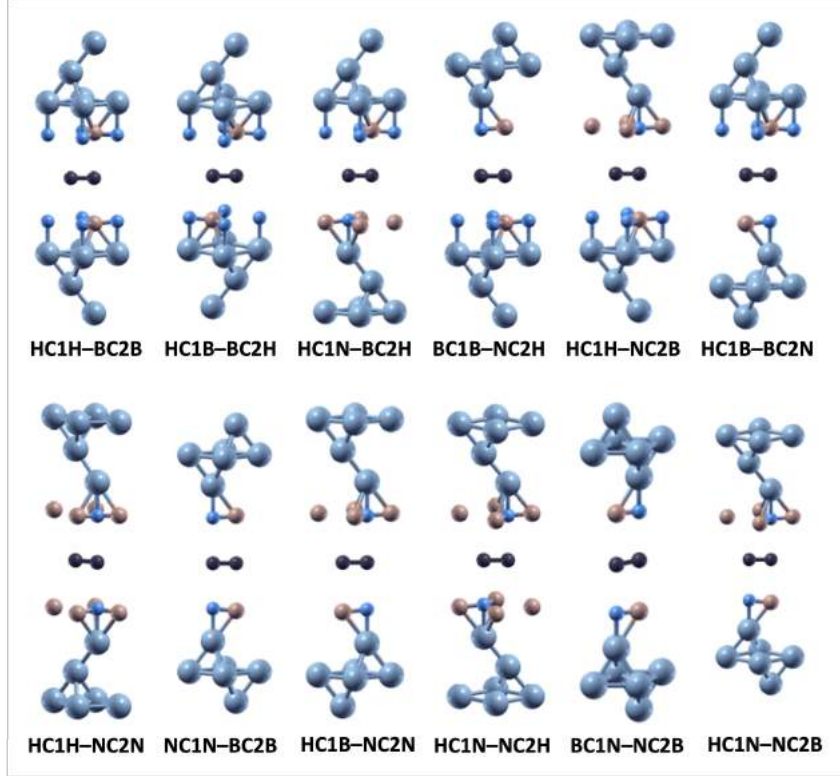


Figure 3.4: The proposed twelve stacking configuration of Ni(111)/hBN-Gr-hBN/Ni(111) with the stacking arrangement name.

and Ni (111) having a top-FCC stacking arrangement with the nearest Ni layer to hBN placed directly on the N-atoms site, the next Ni layer (second nearest Ni to hBN) placed on the hollow site of hBN, and the farthest Ni layer placed on the B-atoms site. As shown in Fig. 3.4, 12 possible stacking configurations between hBN layers and graphene are considered. C1 and C2 represent the carbon atoms in sublattices A and B, respectively. Here, the $aC1x-bC2y$ in Fig. 3.4 is the formula to explain the stacking configuration between the upper hBN, graphene, and lower hBN. The a (x) and b (y) symbols represent the upper (lower) hBN site, which is located directly above (below) C1 and C2, respectively. The H, B, and N represent the hollow, Boron, and Nitrogen site of hBN. For example, HC1B-BC2H means the upper (lower) hBN has the hollow site (B atoms) of hBN right above (below) the C1 and B atoms (hollow site) right above (below) the C2. Both APC and PC were considered for the upper and lower Ni(111) slabs.

The spin-polarized DFT calculations were performed using the SIESTA package [71, 72] to obtain the structural equilibrium, spin-charge density mapping, magnetic properties, band structures and local density of states (LDOS). Furthermore, we described the electron-ion interaction using a revised

Perdew–Burke–Ernzerhof (PBE) functional for a densely packed solid surface (i.e., PBEsol functional) [67] and Troullier–Martins pseudopotential [75] within the generalized gradient approximation. A double-zeta and polarization basis set [76–78] was employed. The atomic positions were relaxed, with a force tolerance of 0.001 eV/Å. A $121 \times 121 \times 1$ Monkhorst–Pack k-mesh was used for calculations. Mesh Cut-off of 800 Ry was used during the calculations. Furthermore, the van der Waals interactions between hBN and graphene is included by applying a dispersion potential of the Grimme type [86]

Chapter 4

Controllable Mass-gapped Dirac-cone of Graphene in Ni/Graphene/Ni Magnetic Junctions

4.1 Introduction

This chapter presents a theoretical study on the possible control of graphene MGDC in Ni/graphene/Ni nano-spin-valve structure through the magnetic alignment control, i.e., anti-parallel and parallel configuration, between the upper and lower Ni slabs. The controllability of the spin-dependent Dirac states in this hybrid structure was studied through graphene's magnetic properties and electronic structure. The spin-dependent charge density and magnetic moment of a Ni/graphene/Ni nanostructure and a band structure calculation were done to show the change in the Dirac cone characteristic.

4.2 Total energy and magnetic properties

The total energies of the Ni/graphene/Ni system for each of the stacking arrangements were considered in order to understand which of the three different stacking arrangements was the most energetically stable. Table 4.1 shows the total energy difference of 3-layer Ni/graphene/3-layer Ni relative to the lowest energy state for AA-stacking, B'A-stacking, and BA-stacking in the anti-parallel and parallel configurations. Among the three different stacking arrangements, B'A-stacking has the highest energy, both in the anti-parallel and

Table 4.1: Total energy difference for various stacking arrangements of 3Ni/graphene/3Ni. The total energy is expressed in meV relative to the ground state (highlighted in bold font). APC(PC) refers to the antiparallel (parallel) magnetic alignments between the upper and lower nickel slabs

Magnetic Configuration	Total Energy (meV)		
	AA-stacking	B'A-stacking	BA-stacking
APC	70.1	156.4	0.0
PC	75.6	154.0	10.5

parallel spin configurations. The highest energy state comes from the weakened bonds of the graphene layer with an upper Ni(111) slab. The weakened bond can be verified by observing the interlayer distance of the B'A stacking structure shown in Table 4.2.

Previous experimental and theoretical studies of graphene growth on top of Ni(111) slabs suggest that the bonding occurs between an A-site carbon atom and the nickel atom closest to it. Indeed, the interlayer distance from the graphene to the nearest Ni(111) slab was concluded to be ~ 0.21 nm [68–70]. In the case of the 3-layer Ni/graphene/3-layer Ni nanostructure in the B'A-stacking arrangement, the distance between the graphene layer and upper Ni(111) slabs becomes 3.28\AA (or 3.26\AA) for the anti-parallel (parallel) configuration, although the interlayer distance between the graphene layer and Ni(111) underlayer is 2.07\AA . This fact also indicates an anti-bonding characteristic because of the considerable increase in the interlayer distance from the typical distance of approximately 2.1\AA .

Furthermore, by comparing the bonding characteristics of the graphene and upper Ni(111) slabs in both the AA-stacking and BA-stacking structures with the anti-bonding nature of the B'A-stacking structure, it can be inferred that the construction of pd hybridization and chemical bonding between the carbon atoms in the graphene layer with the nickel atoms at the interface mainly come from the hybridization of the d_{z^2} orbital of nickel atoms with the p_z orbital of carbon atoms. Therefore, stacking the nickel layer on top of either sublattice A or sublattice B of carbon atoms in the graphene produces a stable Ni/graphene/Ni nanostructure.

Comparing the stable structures of the 3-layer Ni/graphene/3-layer Ni, it was found that BA-stacking has a slightly smaller interlayer distance than AA-stacking, indicating that BA-stacking has a stronger pd hybridization than AA-stacking. This difference shows that BA-stacking has the lowest energy among the three stacking arrangements. The strong pd hybridization between

Table 4.2: Interlayer distance between the Ni(111) slabs with graphene for three different stacking arrangements. APC(PC) refers to the antiparallel (parallel) magnetic alignment between the upper and lower nickel slabs

Layer	Interlayer distance (Å)					
	AA-stacking		B'A-stacking		BA-stacking	
	APC	PC	APC	PC	APC	PC
Graphene-Upper Ni slab	2.18	2.20	3.28	3.26	2.07	2.07
Graphene-Lower Ni slab	2.18	2.20	2.07	2.07	2.07	2.07

a carbon atom of the graphene layer with the upper or lower Ni(111) layer at the interface of BA-stacking leads to a charge transfer from the nickel layers to the graphene.

Further investigation on the most stable structure, BA-stacking, was done by comparing two possible structure arrangements of the second and third layer namely, B(top-hcp)A-stacking—the second (third) layer of upper Ni(111) slab on top of hollow- (B-) site of graphene (the initial proposed structure of BA-stacking) and B(top-fcc)A-stacking—the second (third) layer of upper Ni(111) slab on the top of B- (hollow-) site of graphene. The result showed that B(top/hcp)A-stacking has higher energy by 13.5 meV compare to B(top/fcc) stacking. Although B(top/fcc) stacking has lower energy than B(top/hcp)A-stacking, the difference was considerably small enough to allow both configurations to occur. It implied that the small different might not change the physical properties of the whole system.

Within the BA-stacking structure, the total energy of the anti-parallel configuration was lower than that of the parallel configuration by 10.5 meV. The anti-parallel configuration, which has a more stable energy state than the parallel configuration, is in agreement with experimental data reported by Mandal et al. [39]. This total energy difference mainly comes from the magnetic configuration within the graphene layer.

Spin-charge density mapping was created to understand the spin orientation of each atom in the 3-layer Ni/graphene/3-layer Ni. In Fig.4.1, the AFM configuration of the carbon atoms within the graphene layer, when the magnetic configuration between the upper and lower nickel slabs was anti-parallel, is shown. When the magnetic configuration between the upper and lower nickel slabs is parallel, a ferromagnetic (FM) configuration, which has a higher energy than AFM configuration, occurs within the graphene layer. AFM configuration is realized as the most stable state, except when an external magnetic field stabilizes FM configuration.

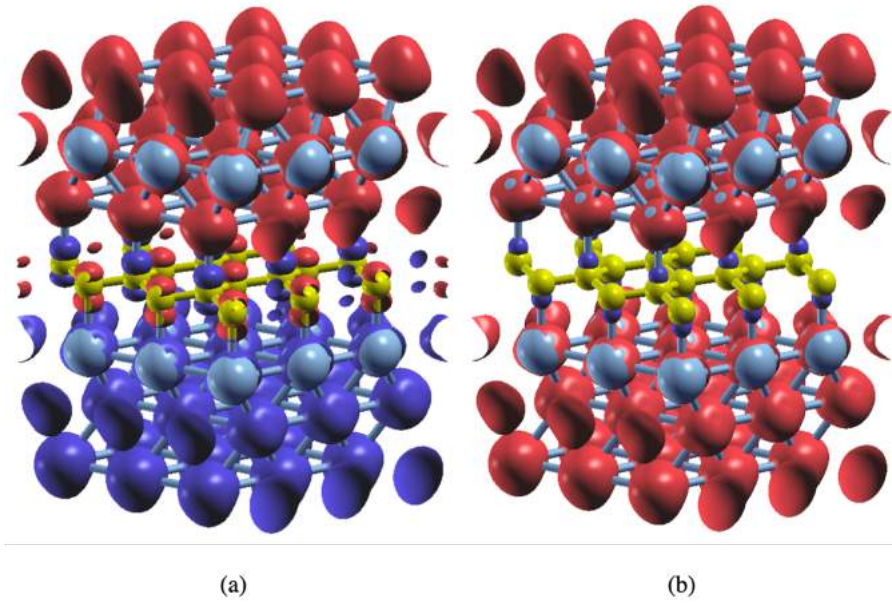


Figure 4.1: Spin-charge density of the 3-layer Ni/graphene/3-layer Ni in the (a) anti-parallel configuration (isovalue=0.00170) and (b) parallel configuration (isovalue=0.00168). The charge density in red represents spin-up electron density and that in blue represents spin-down electron density.

The different magnetic configurations of the carbon atoms in the sublattices A and B within the graphene layer comes from the magnetic interaction between the Ni layer and graphene. Carbon atoms in graphene tend to have an anti-parallel spin configuration with the neighboring nickel atoms. This rule is the most relevant rule for the energetics of Ni/graphene/Ni structures. As a result of the spin anti-parallel, *i.e.*, locally anti-ferromagnetic, alignment between each pair of Ni and carbon atoms, AFM (FM) configurations in the graphene plane happens for the anti-parallel (parallel) configuration of Ni slabs. The local AFM configuration between a carbon atom and nickel atom will be considered in the subsequent sections by analyzing the hybridization nature of electron orbitals.

In the present model, the upper Ni(111) slab was fixed in a spin-up configuration, whereas the lower slab could be controlled to have either a spin-up or spin-down configuration. The nickel atoms on the upper Ni/graphene interface hybridized with carbon atoms on sublattice B, and since the upper Ni(111) slab was fixed to have a spin-up alignment, the carbon atoms on the sublattice B of graphene had the spin-down configuration. By contrast, the lower Ni(111) slab was hybridized with carbon atoms in the sublattice A. Since the lower Ni(111) slab can be controlled between the spin-up and spin-down configurations, the induced magnetic moment of the carbon atoms in sublattice A can also be

Table 4.3: Magnetic moment for each atom of 3Ni/graphene/3Ni. AFM(FM) refers to the antiparallel (parallel) magnetic alignment between the upper and lower nickel slabs.

Atom	Magnetic Moment (μ_B)	
	AFM configuration	FM configuration
C (sub-lattice A)	0.0126	-0.0048
C (sub-lattice B)	-0.0128	-0.0047
Ni(top)-first layer	0.2898	0.2645
Ni(top)-second layer	0.6150	0.5958
Ni(top)-third layer	0.6785	0.6732
Ni(bottom)-first layer	-0.2770	0.2815
Ni(bottom)-second layer	-0.6213	0.6050
Ni(bottom)-third layer	-0.6763	0.6670

controlled.

The carbon atoms of sublattices A and B in graphene tend to have an antiferromagnetic (AFM) configuration due to the half-filled p_z orbital and Pauli's exclusion principle. This rule is often found in organic molecules in sp^2 hybridization or magnetic alternant hydro-carbon systems [87, 88]. The spin configuration of AFM is often considered as a realization of the spin-density-wave. Due to the nature of graphene, the carbon atoms of another sublattice will have the opposite alignment with the carbon atoms hybridizing with the nickel atoms. Therefore, the lowest energy state was found to be the anti-parallel configuration.

Interestingly, in the parallel configuration, FM spin alignment appears within the graphene layer. However, the appearance of the FM configuration within graphene, where the spin moment has the opposite direction to the Ni layers, was unexpected. In the case of the Ni/graphene interface, i.e., graphene on a Ni substrate, carbon atoms are placed in two different sites, A and B, where one of the sites were hybridized with Ni layer and the another not. The magnetic moment of carbon atoms that were not hybridized with Ni layer, which has a parallel spin to the nickel slab, was higher than the hybridized one, where the antiferromagnetic configuration in graphene appears as a whole. It implied that the Ni(111) slab and unhybridized carbon atoms had a stronger magnetic interaction. Oppositely, the FM configuration within graphene of Ni/graphene/Ni system implied another conclusion that the induced magnetic moment at the hybridized carbon atoms had a stronger magnetic interaction with the Ni(111) slabs than the unhybridized carbon atom. It was because the direction of the magnetic moment was reversed in the unhybridized carbon

Table 4.4: Total energy differences between various numbers of the nickel layer in the BA-stacking arrangement. The total energy is expressed in meV relative to the ground state (highlighted in bold font). APC(PC) refers to the antiparallel (parallel) magnetic alignment between the upper and lower nickel slabs.

Number of Nickel Layers	Total Energy (meV)	
	APC	PC
1	total energy same (non-magnetic)	
2	0.0	9.9
3	0.0	10.4
4	0.0	1.3
5	0.0	7.6
6	0.0	6.1

atoms. Therefore, a stronger magnetic interaction and the anti-parallel configuration between the hybridized carbon atom and the Ni layer were concluded.

The magnetic configuration, which is initiated by the magnetic interaction of carbon and nickel atoms at the interface, within the graphene layer leads to the tunable magnetic moment configuration between the carbon atoms in sublattices A and B of graphene. The tunable induced magnetic moment between the AFM and FM configurations provides a new insight into the electronic structure of graphene, since the previous studies have only reported that the induced magnetic moment of graphene is either in the AFM configuration [89] or FM configuration [90]. An additional remarkable point is that the total energy difference between the anti-parallel and parallel configurations is in the order of meV, which implies that the magnetic configuration change does not require an extremely high external magnetic field.

The total energy was calculated for various thicknesses to show the consistency of the most stable magnetic configuration and the orientation of the Ni/graphene/Ni nanostructure's magnetic moment. Table 4.4 shows the total energy for all variations of the number of Ni layers from 1 to 6 in the anti-parallel and parallel configurations. For the 1-layer Ni structure at both sides of the graphene, the lowest state is a non-magnetic state. The variation of the number of Ni layers from 2 to 6 implies that the anti-parallel configuration has the lowest energy, although the total energy difference between the anti-parallel and parallel configurations is different for each number of layers. The charge-spin density mapping also shows the magnetic configuration of Ni/graphene/Ni.

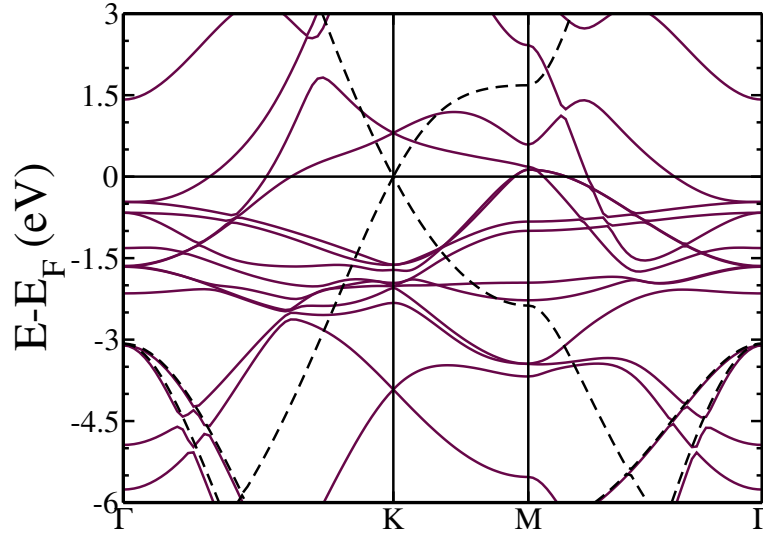


Figure 4.2: Electronic band structure of 1-layer Ni/graphene/1-layer Ni in a non-magnetic state. The black dashed line is the band structure of pristine graphene, to be used as reference. The Dirac cone characteristic can be seen around the K-point high-symmetry and near the Fermi energy as well as around -4 eV.

4.3 Analysis of electron orbitals for Ni/graphene/Ni with 1-layer Ni slabs

As shown in the last section, in the case of 1-layer Ni growth on both sides of graphene, the Ni/graphene/ Ni nanostructure becomes non-magnetic. The non-magnetic property of the 1-layer Ni/graphene/1-layer Ni occurred due to the charge transfer from the d_{z^2} orbital of Ni atoms within 1-layer Ni to the p_z orbital of carbon atoms, either for sublattices A or B within graphene, which fully filled the p_z orbitals of the carbon atoms and caused the net magnetic moment to become zero.

The electronic band structure of 1-layer Ni/graphene/1-layer Ni is shown in Fig. 4.2. This band structure implies relevant orbital natures in Ni/graphene/Ni structures. Here, every band around the Fermi level was characterized.

Eight bands from Ni $3d$ branches can be seen just below the Fermi level at $E_F = 0$, i.e., at the Γ point. Other two bands of $3d$ go down to approximately -5eV or below. This energy is even below the top of the sp^2 - σ bands appearing at -3 eV. At the Γ point, the π band of graphene, which has an energy of around -7.5eV in the pristine graphene, is rather stabilized. This is attributed to the pd hybridization. Since the flat graphene becomes deformed with staggered modification, the orbital nature of π becomes a little closer to that of the sp^3 -

hybridized orbital. This is the secondary reason why such an apparent drop is observed in the π band. Roughly speaking, the eight $3d$ bands of Ni run nearly horizontally across the whole Brillouin zone. Meanwhile, the remaining two branches coming from the d_{z^2} bands suffer strongly from the pd hybridization.

Local Wannier orbitals of p_z and d_{z^2} symmetries were defined at each carbon site and nickel atom, respectively. These orbitals are represented by $\phi_{p_z,\eta}(\mathbf{r} - \mathbf{R}_i)$ and $\varphi_{z^2,\zeta}(\mathbf{r} - \mathbf{R}_i)$. Here, the orbitals are defined for each unit cell indexed by i . The vector \mathbf{R}_i represents the position of the i -th unit cell. The index η denotes the sublattice site A or B of graphene. ζ denotes the sublattice sites for the upper and lower Ni layers. However, by limiting the argument to the BA-stacking, ζ is identified as η , since every Ni atom is just on (or below) a carbon atom at the A (or B) site. Therefore, it is enough to consider simplified notations $\phi_{i,p_z,\eta}$ and $\varphi_{i,z^2,\eta}$.

For graphene, the Dirac points appear at the special points of K and K'. Since the three-fold rotational symmetry, glide-reflection symmetry, and chiral symmetry of the original graphene is preserved for the AB stacking of the 1-layer Ni/graphene/1-layer Ni, the Dirac point is maintained in this hybrid structure. More precisely, Dirac cones were doubled in the band structure of Fig. 4.2. At the K point, around $E - E_F \sim -4\text{eV}$, there are lower Dirac cones. There are also more upper Dirac cones above the Fermi level. The lower (upper) cone consists of the bonding (anti-bonding) level of $\phi_{i,p_z,\eta}$ and $\varphi_{i,z^2,\eta}$.

The orbital energy of p_z is much lower than that of nickel d_{z^2} . Therefore, the charge transfer is from nickel to carbon. The magnetic moment of carbon is not easily induced in this sense. The anti-bonding nature of the upper Dirac cone close to the Fermi level is important for the induced magnetism of graphene attached to nickel slabs.

Here, it should be noted that the effective potential at each sublattice is the same as the effective potential for the non-magnetic solution as far as the Ni /graphene/Ni system maintains the structural symmetry. Topologically, the arrangement of the effective Wannier orbital $\tilde{\phi}_{i,\eta,\pm}$ for both the upper and lower Dirac cones is the honeycomb lattice. Therefore, no gap opening happens for two Dirac cones in Fig. 4.2.

When spin-density distribution causes a staggered contribution in a spin-dependent effective potential, a gap opening phenomenon occurs. This point is relevant for the discussion in the next section.

4.4 Effect of magnetic configuration on the electronic structure and in-plane conductance

The appearance of the induced magnetic moment on graphene and strong pd hybridization between the nickel and carbon atoms on graphene cause the Dirac cone characteristics of the graphene band structure to change.

The opening gap of the Dirac cone has been reported by previous theoretical studies of the Ni/graphene interface, where the gap size between the spin majority and spin minority channels is different due to the induced magnetic moment difference between sublattices A (carbon atoms with pd hybridization with nickel atoms) and B. The magnetic moment of carbon atoms can be also expressed as the spin-charge density difference between spin-up and spin-down ($n_{\uparrow}(\mathbf{r}) - n_{\downarrow}(\mathbf{r})$). The charge density difference between spin-up and spin-down is proportional to the Stoner gap formed on the energy level difference between spin-up and spin-down. In the Ni/graphene interface case, the magnetic moment of carbon atoms on sublattice A is smaller than that of sublattice B; the Stoner gap in the carbon atoms on sublattice A is also smaller compare to that of sublattice B.

A relevant question here is whether not the Ni/graphene/Ni structures show any qualitatively different features from a single Ni/graphene interface.

Figure 4.3 shows the band structure of 3-Ni layer /graphene/3-Ni layer spin-valve-like structure. The strong hybridization between the carbon p_z orbital with nickel d_{z^2} on the top and bottom is shown as the creation of bonding and anti-bonding Dirac cones and several level anti-crossing points in the band structure. Although the band structure of the carbon p_z orbital changes quite significantly, the characteristics of Dirac cones on high symmetry K-points can still be recognized for both the anti-parallel and parallel configurations. Here, two Dirac cones are seen near the Fermi energy and around -4eV below the Fermi energy.

For the case of anti-parallel configuration, Table 4.3 shows that the induced magnetic moment of the carbon atoms on sublattice A is in the opposite configuration to that on sublattice B. The magnetic moment of carbon atoms on sublattice A has a spin-up configuration, which means that the spin-up charge density is higher than the spin-down charge density ($n_{A\uparrow}$), while carbon atoms on sublattice B have the opposite configuration.

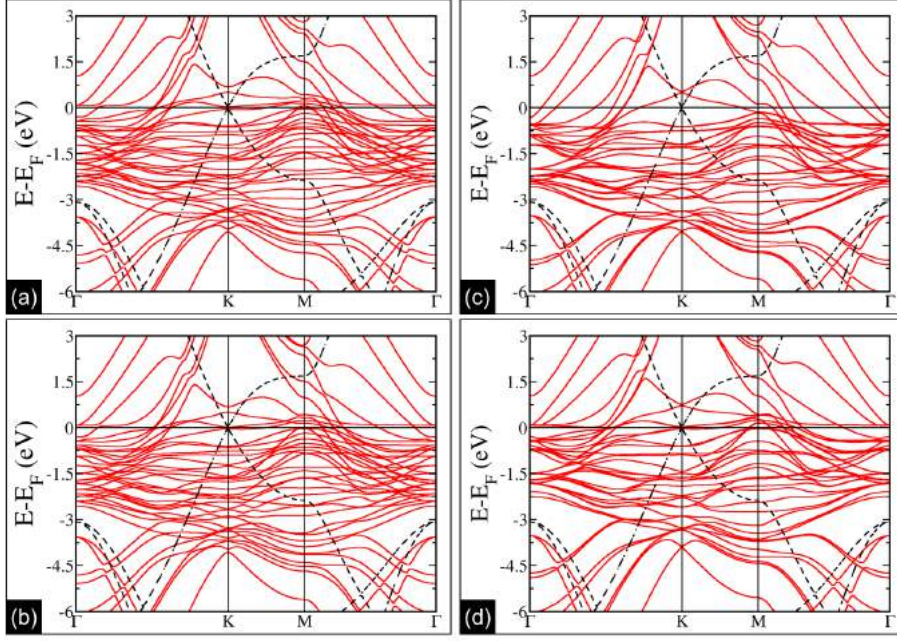


Figure 4.3: 3-layer Ni/graphene/3-layer Ni band structure in the anti-parallel configuration for the (a) spin majority channel and (b) spin minority channel, and in parallel configuration for the (c) spin majority channel and (d) spin minority channel. The black dashed line is the band structure of the pristine graphene to be used as reference. The Dirac cone characteristic can be seen around the K-point high-symmetry and near the Fermi energy.

An integrated spin-charge density $n_{\eta,\uparrow}$, and $n_{\eta,\downarrow}$ was introduced, where η is either A or B. The value of $n_{\eta,\sigma}$ is assumed to be obtained by integrating $n_{\sigma}(\mathbf{r})$ within an ionic radius of the carbon atom, where $\sigma = \uparrow$ or \downarrow . Table 4.3 also shows that the magnetic moment between the carbon atoms on sublattices A and B are comparably equal in the anti-parallel configuration. Therefore,

$$n_{A,\downarrow} = n_{B,\uparrow} > n_{A,\uparrow} = n_{B,\downarrow}.$$

The spin-GGA effective potential has a contribution approximately proportional to the spin moment, or the spin density, $n_{\eta,\uparrow} - n_{\eta,\downarrow}$. This spin-dependent potential is lowered for the majority spin when the local spin density is given by the majority, while the minority spin feels higher energy. In other words, the energy of the up-electron decreases when the up-spin density increases, but increases when the down-spin density increases around the given point.

Therefore, the up-spin and down-spin suffer from different effective potentials $v_{\text{eff},\sigma}(\mathbf{r})$ in the anti-parallel configuration. Taking a spin-dependent Wannier function, $\tilde{\phi}_{i,\eta,-,\sigma}(\mathbf{r})$, created similar to that in the last section, a simple rule can be derived for an averaged spin-dependent contribution for the

potential $\langle \tilde{\phi}_{i,\eta,-,\sigma} | \bar{v}_{\text{eff},\sigma} | \tilde{\phi}_{i,\eta,-,\sigma} \rangle$ with respect to the Wannier basis.

$$\langle \tilde{\phi}_{i,A,-,\uparrow} | \bar{v}_{\text{eff},\uparrow} | \tilde{\phi}_{i,A,-,\uparrow} \rangle > \langle \tilde{\phi}_{i,B,-,\uparrow} | \bar{v}_{\text{eff},\uparrow} | \tilde{\phi}_{i,B,-,\uparrow} \rangle, \quad (4.1)$$

$$\langle \tilde{\phi}_{i,A,-,\downarrow} | \bar{v}_{\text{eff},\downarrow} | \tilde{\phi}_{i,A,-,\downarrow} \rangle < \langle \tilde{\phi}_{i,B,-,\downarrow} | \bar{v}_{\text{eff},\downarrow} | \tilde{\phi}_{i,B,-,\downarrow} \rangle, \quad (4.2)$$

$$\langle \tilde{\phi}_{i,A,-,\uparrow} | \bar{v}_{\text{eff},\uparrow} | \tilde{\phi}_{i,A,-,\uparrow} \rangle = \langle \tilde{\phi}_{i,B,-,\downarrow} | \bar{v}_{\text{eff},\downarrow} | \tilde{\phi}_{i,B,-,\downarrow} \rangle, \quad (4.3)$$

$$\langle \tilde{\phi}_{i,B,-,\uparrow} | \bar{v}_{\text{eff},\uparrow} | \tilde{\phi}_{i,B,-,\uparrow} \rangle, = \langle \tilde{\phi}_{i,A,-,\downarrow} | \bar{v}_{\text{eff},\downarrow} | \tilde{\phi}_{i,A,-,\downarrow} \rangle. \quad (4.4)$$

Eqs. (4.1) and (4.2) conclude that a gap opens at the Dirac point due to the broken chiral symmetry. From Eqs. (4.3) and (4.4), it can be said that the gap size is the same for both the up and down spins. Therefore, the Stoner gap size formed on the spin majority and minority channels are equal, as shown in Fig. 4.3(a) and (b).

Consider a realistic device by taking the attachment of pristine graphene as leads of the Ni/graphene/Ni structure. From this perspective, the momentum of electron in the graphene layer can be conserved by considering the specular reflection effect on the edge of the Ni layer. Looking closely at the K-point near the Dirac cone, separation of Dirac bands from the Ni S-band in the first Brillouin zone happens. Assume that the edge of the Ni layer perpendicular to the current path is periodic, sharply cut with no impurities, and the specular reflection of electron on graphene occurs. If the wavefunction of electron is larger than the atomic distance between the nickel on the edge perpendicular to the current path, the momentum of the Dirac band electrons will conserve.

In contrast, Fig. 4.3(c) and (d) show the band structure of 3-layer Ni/graphene/ 3-layer Ni in the parallel configuration, where it satisfied an equality and inequality as follows

$$\langle \tilde{\phi}_{i,A,-,\uparrow} | \bar{v}_{\text{eff},\uparrow} | \tilde{\phi}_{i,A,-,\uparrow} \rangle = \langle \tilde{\phi}_{i,B,-,\uparrow} | \bar{v}_{\text{eff},\uparrow} | \tilde{\phi}_{i,B,-,\uparrow} \rangle, \quad (4.5)$$

$$\langle \tilde{\phi}_{i,A,-,\downarrow} | \bar{v}_{\text{eff},\downarrow} | \tilde{\phi}_{i,A,-,\downarrow} \rangle = \langle \tilde{\phi}_{i,B,-,\downarrow} | \bar{v}_{\text{eff},\downarrow} | \tilde{\phi}_{i,B,-,\downarrow} \rangle, \quad (4.6)$$

$$\langle \tilde{\phi}_{i,A,-,\uparrow} | \bar{v}_{\text{eff},\uparrow} | \tilde{\phi}_{i,A,-,\uparrow} \rangle > \langle \tilde{\phi}_{i,A,-,\downarrow} | \bar{v}_{\text{eff},\downarrow} | \tilde{\phi}_{i,A,-,\downarrow} \rangle, \quad (4.7)$$

Although the Dirac cone still survives, the energy level between the Dirac cone on the spin majority channel is lower than the Dirac cone on the spin minority channel because of the characteristics of the ferromagnetic material. Note that the above discussion does not directly reveal the relations between the orbital energies of the Wannier basis. This is because the orbital energy is determined by the whole character of $v_{\text{eff}}(\mathbf{r})$, where the majority spin gains energy by the large spin moment at the Ni atoms.

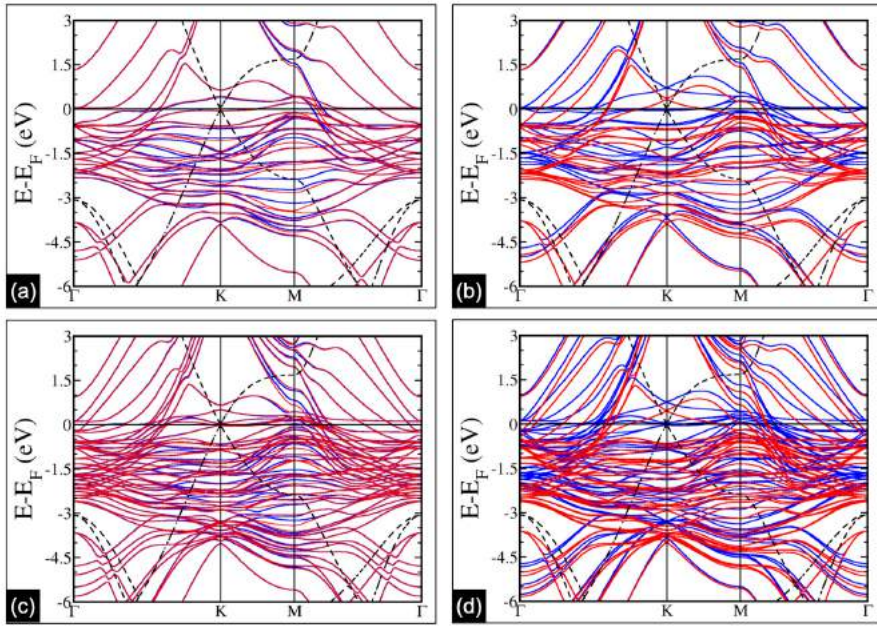


Figure 4.4: Bandstructure of 2-layer Ni/graphene/2-layer Ni in the (a) anti-parallel configuration and (b) parallel configuration; and 4-layer Ni/graphene/4-layer Ni in the (c) anti-parallel configuration and (d) parallel configuration. In (a), (b), (c), and (d), red represents the spin-majority channel, whereas blue represents the spin-minority channel. The black dashed line is the bandstructure of the pristine graphene, taken as a reference.

The opened gap of the Dirac electrons at the high symmetry K-point in the spin-majority and -minority channels for the anti-parallel spin configuration implies an increase of resistance on the in-plane conductance of the graphene layer compared to the pristine graphene. In contrast, the survival of the Dirac cone for the parallel magnetic configuration of the Ni(111) layers implies that the in-plane conductance via the K-point contribution will give lower resistivity compared to that in the anti-parallel spin configuration.

Since the anti-parallel configuration is the lowest state, we can start from the high resistance state having the opened gap at the Dirac cone. Using an external magnetic field, the spin moment direction can be reversed. In the parallel configuration, the gap is closed in both majority and minority channels. Thus, the structure can act as a field-induced switch for the electron current.

In case of unbalanced spin moments below and above the Graphene layer, the applied field may reverse one of the spin directions, maintaining the other stronger spin moment undisturbed. After switching off the field, the system can return to an energetically stabler anti-parallel spin configuration than the par-

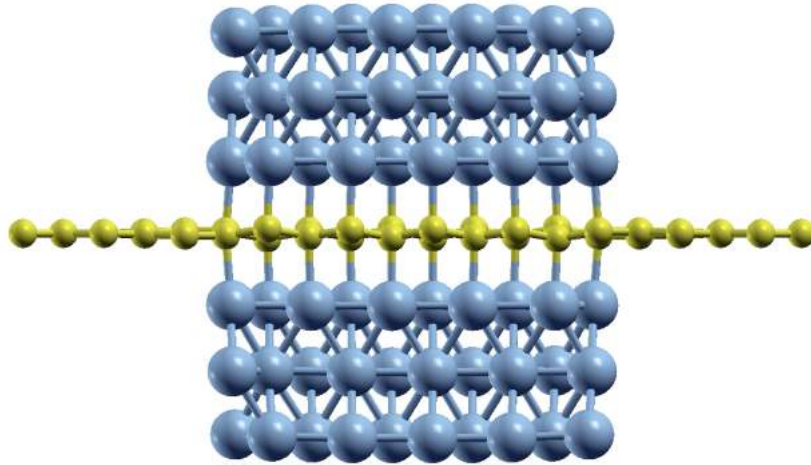


Figure 4.5: Scattering region of Ni/Graphene/Ni nano-spin-valve-like structure created on the part of a graphene plane.

allel configuration. Alternatively, even when a residual spin moment remains for the zero fields, the weakly locked moment can be reversed by applying a magnetic field in the opposite direction. This controllability is essential to consider an application of this system.

The opening gap of the Dirac cone in the anti-parallel configuration and the survival of the Dirac cone in the parallel configuration are consistent for 2-layer and 4-layer nickel, as shown in figure 4.4. For the number of Ni layers more than four, the band-structure becomes extremely complex, making recognizing the Dirac cone characteristics difficult. However, owing to a preserved symmetry, we can expect the same physics.

4.5 Discussion on the possible application for spin-electronic device

To start the discussion on the possible application for spin-electronic device, a junction system is proposed here. Figure 4.5 shows a Ni/Graphene/Ni nano-spin-valve-like structure created on the part of a graphene plane. The local Ni structures above and below graphene are optimized by DFT simulations. This magnetic region gives scattering of electron waves. Pristine graphene parts at both sides are used as the electrodes. Through the one-dimensional device structure, we consider a current path from the left to right electrodes for both spins.

As shown in Fig. 4.5, the edges of the Ni(111) layers are atomically sharp.

In case of a long Ni part in the perpendicular direction for the current path, the specular reflection/transmission for electron waves can be obtained. The Dirac cone characteristic is dependent on the Ni spin configuration. Therefore, change in the in-plane conductance along the graphene layer across the scattering region is expected.

The Fermi energy (the chemical potential) can be slightly shifted from the charge neutrality point. Note that, in the anti-parallel spin configuration, net spin current is not observed even when the current path is via the Ni(111) layers; in contrast, in the parallel configuration, the spin-majority and -minority channels created by Ni structures have different scattering processes. In the graphene layer, a closed gap phenomenon is observed, which allows the spin majority channel for the spin alignment to be less resistive than in the anti-parallel spin configuration. In addition, owing to the spin blockade effect for current paths via the Ni(111) layers, a stronger conduction is observed for a selective spin direction only. Thus, we can easily create a spin-current switching.

At low temperatures, when coherent transmission becomes dominant for the current conduction, where a lateral element of the momentum along the edge is conserved, the spin filtering phenomenon is expected to be enhanced. Consider a wider Ni(111) layer region along the one-dimensional conduction path. Dirac electrons tunnel via states in the window opened in the Brillouin zone around the K-point. In the anti-parallel configuration, when only coherent tunneling paths along the structure determine the transmission probability, the current conduction is effectively blocked. This is because the gap is open and the Dirac electrons are blocked. Since transmission probability depends on the electronic structure at the scattering region, we can conclude a spin-configuration dependent tunneling phenomenon in this junction structure. This effect will lead to a spin filtering effect of electron current in the graphene electrode. In the anti-parallel configuration, this junction system also leads to a spin Hall effect [91] owing to the spin-orbit interaction originating in the Ni layers.

The opened gap structure at the Ni(111)/graphene/Ni(111) interface suggests a moment-direction-dependent characteristic for the lateral conductance with a perpendicular current path. In this conventional use for a Ni-based spin valve, the gap opening effect should be considered properly. The determination of the transmission probability is future work for the present study.

4.6 Summary

In this study, DFT (spin-GGA) calculation on 3-layer Ni/graphene/3-layer Ni shows that among the three stacking arrangements, the BA-stacking is the stablest stacking structure, and within BA-stacking, the anti-parallel configuration of upper and lower Ni(111) slabs has lower energy than the parallel configuration. This finding is in agreement with the previous experimental study. The two magnetic arrangements of Ni(111) slabs affect the configuration of the induced magnetic moment of graphene.

In case of the anti-parallel configuration between Ni(111) slabs, carbon atom sublattices A and B of graphene have an AFM configuration. By contrast, in case of the parallel configuration between two Ni(111) slabs, the configuration of sublattices A and B of graphene have an FM configuration. The AFM configuration of graphene's carbon atoms leads to the gap opening on the Dirac cone of the graphene bandstructure; meanwhile, the FM configuration bandstructure shows the survival of the Dirac cone both for spin-majority and -minority channels.

The opening and survival of the Dirac cone will affect the in-plane conductance of graphene in which the open gap Dirac cone configuration will have a higher resistance than the close gap Dirac cone configuration. Further conductivity calculation must be conducted to understand how much does the opening and closing of the gap due to induced magnetic moment on graphene's carbon atoms affect the conductivity of the graphene layer.

This page intentionally left blank

Chapter 5

Colossal In-plane Magnetoresistance Ratio of Graphene Sandwiched with Ni Nanostructures

5.1 Introduction

This chapter presents a theoretical study on the in-plane conductance and magnetoresistance of graphene partially sandwiched between Ni(111) nanostructures. Here, investigation was done on the effectiveness of a controllable Dirac cone on graphene conductance to realize a high MR ratio. For that purpose, a system consisting of Ni(111) nanostructures with a finite size and atomic-scale width of 12.08 Å sandwiched the middle part of graphene was proposed. Both the APC and PC states of the upper and lower Ni(111) structures are considered. First-principles quantum transport calculations, which coupled density functional theory (DFT) with the nonequilibrium Green's function, were performed. Our calculation results observed a high and colossal in-plane MR ratio of graphene about 284% and 3100%. A higher MR ratio beyond 3100% can be obtained when the width of the Ni(111) structures on a nanometer scale are considered.

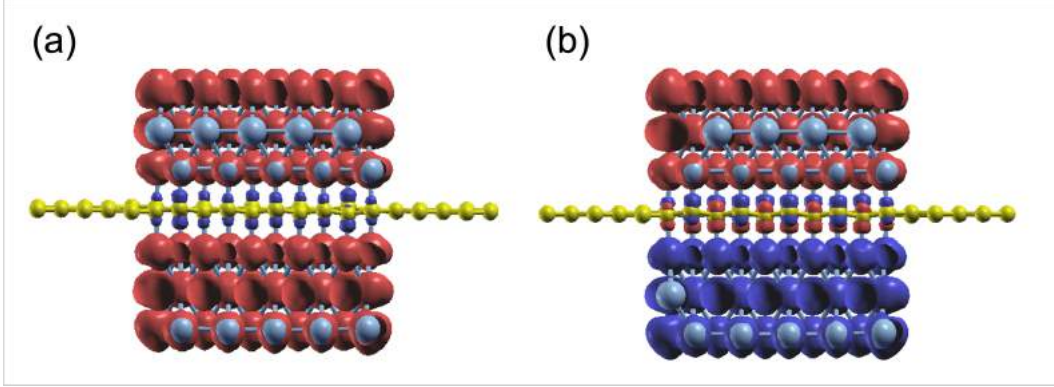


Figure 5.1: Spin-charge density mapping of the proposed system when the Ni(111) nanostructures are in (a) PC and (b) APC states (red: spin-up charge density; blue: spin-down charge density).

5.2 Characteristics of Induced Magnetic Moment of Graphene

We investigated the characteristics of the induced magnetic moment on graphene, which is sandwiched between the Ni(111) nanostructures. Particularly we focused on the boundaries between the bare and sandwiched graphene. Mapping of the spin-charge density, as shown in Figure 5.1, indicates that the magnetic moment was induced only on graphene sandwiched by Ni(111) nanostructures up to the boundaries. However, the details of the induced magnetic moment profile, shown in Figure 5.2, indicate that the magnetic moment was damped to a small value on the bare graphene part near the boundaries for a few C atoms before reaching zero. This damping corresponds to wave function matching at the boundaries between sandwiched and bare graphene.

The C atoms of the bare graphene far from the boundaries have no induced magnetic moment, as shown in Figure 5.1 and Figure 5.2. Here, the Dirac cone of the graphene is similar to that of the pristine graphene because the chiral symmetry was preserved: $n_{A\sigma} = n_{B\sigma}$ with $\sigma = \uparrow$ or \downarrow . Meanwhile, the sandwiched graphene has an induced magnetic moment depending on the magnetic alignment of the Ni(111) nanostructures. For the Ni(111) nanostructures in APC state, Figure 5.2(a) indicates that the induced magnetic moments on the C_A and C_B atoms of the sandwiched graphene have an antiferromagnetic order. Thus,

$$n_{A\downarrow} = n_{B\uparrow} > n_{A\uparrow} = n_{B\downarrow}, \quad (5.1)$$

which implies that the chiral symmetry is broken, and the mass gap of the Dirac

cone is open. However, for Ni(111) nanostructures in PC state, the induced magnetic moments in the C_A and C_B atoms of the sandwiched graphene have the same magnetic orientation and almost the same value (Figure 5.2(b)). Thus,

$$n_{A\uparrow} = n_{B\uparrow} > n_{A\downarrow} = n_{B\downarrow}, \quad (5.2)$$

This means that the equipotential between the C_A and C_B preserves the Dirac cone. However, due to the induced magnetic moment on sandwiched graphene, the Dirac cone on the spin majority channel is lower than that on the spin minority channel, which is a characteristic of ferromagnetic materials.

The magnetic moment characteristics of the C_A and C_B atoms in the sandwiched graphene agree with the findings of a previous chapter 4. Interestingly, the characteristics of the induced magnetic moments in the sandwiched graphene part were different in the APC and PC states. In the APC state, the amplitude of the induced magnetic moment decreased from the center of the sandwiched graphene to the boundary direction. The magnetic moment amplitude of the C atoms at the center of the sandwiched graphene agrees well with the magnetic moment of the C atoms of Ni/graphene/Ni MTJ (a Ni/graphene/Ni system with periodic boundary conditions on the x- and y-axes), which is $\sim 0.04 \mu_B$. This means that the decrease in the magnetic moment amplitude along the boundary direction corresponds to the characteristics found in the finite size of the Ni nanostructures. From the structure of the system, this decrease is attributed to the coordination of Ni(111) nanostructures, which compresses their shape toward the center but maintains their bond with C atoms at the interfaces. An edged shape was formed on the Ni(111) nanostructures at the boundaries, which increases the lattice mismatch between the Ni layer at the interfaces and the graphene layer, and in turn, decreases the charge transfer from Ni atoms to C atoms. Thus, the reduced charge transfer from the Ni atoms to the C atoms at the interface decreases the induced magnetic moment on the C atoms. Since the lattice mismatch increases along the direction of the boundary, the induced magnetic moment also decreases along the same direction. However, the profile of the induced magnetic moment on sandwiched graphene is unique in PC. The induced magnetic moment initially decreases from the center of the sandwich to the boundaries. However, it then increases even higher than that of the center part before finally decreasing again near the boundaries. The magnetic moment of the C atoms in the center of the sandwiched graphene was approximately equal to the induced magnetic moment of the C atoms of

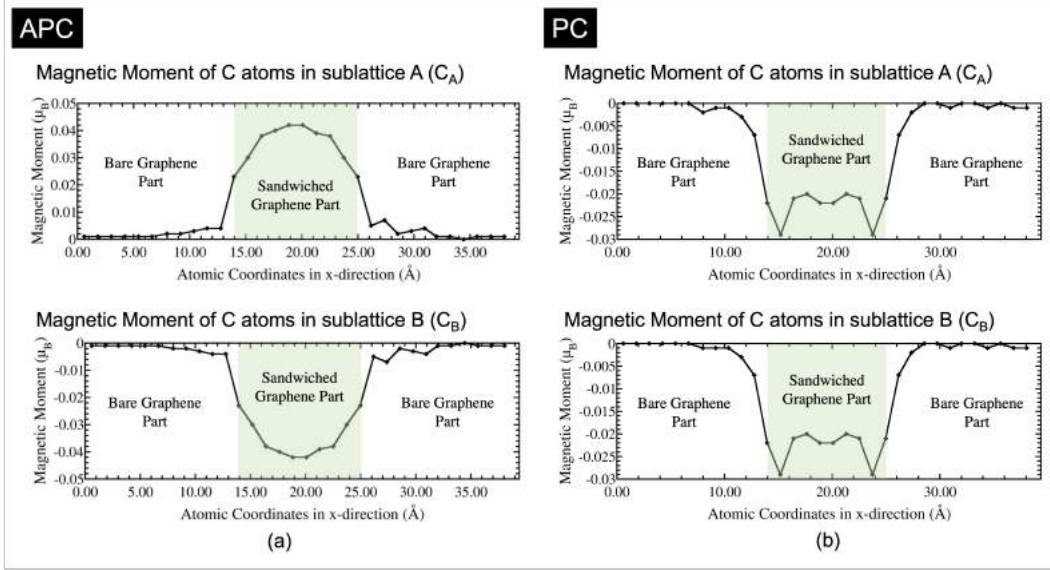


Figure 5.2: The induced magnetic moment of graphene of the proposed system when the Ni(111) nanostructures are in (a) APC and (b) PC states.

the Ni/graphene/Ni MTJ, which was $\sim 0.022 \mu_B$. Furthermore, the decrease in the induced magnetic moment on the neighboring C atoms, which shifted from the center of the sandwich graphene to the boundary, corresponds to the increasing lattice mismatch, similar to the case of APC. Additionally, the amplitude of the magnetic moment on the C atoms increased even more than that in the center part at the boundaries due to the reduction in the antiferromagnetic configuration between sublattices A and B near the boundary. In the periodic system of Ni/graphene/Ni MTJ, we obtained higher amplitude of the induced magnetic moment of C atoms in APC is higher than that in PC since the carbon atoms of sublattices A and B in graphene had to have an antiferromagnetic (AFM) configuration because of the half-filled p_z -orbital and Pauli's exclusion principle. This rule is often found in organic molecules in sp^2 -hybridization or magnetic alternant hydrocarbon systems [88]. The contribution of the antiferromagnetic alignment between the hybridized C and Ni atoms near the boundaries is more dominant than that of the AFM alignment between the C atom sublattices A and B, leading to the increased induced magnetic moment. Finally, at the boundaries, the induced magnetic moment of the C atoms in the sandwiched part decreases again, indicating increased lattice mismatch.

These changes in the induced magnetic moment on sandwiched graphene affect the Dirac cone and mass-gapped Dirac-cone characteristics. For the Ni(111) nanostructures in the APC, the decreasing induced magnetic moment

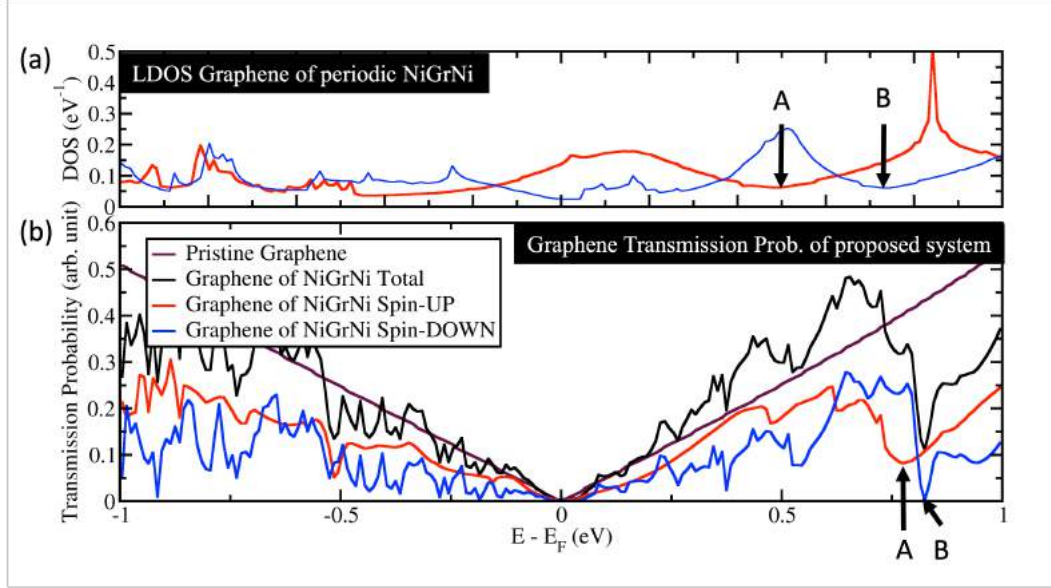


Figure 5.3: The transmission probability of graphene from the proposed system when Ni(111) nanostructures in PC state.

of the sandwiched graphene toward the boundary reduces the size of the mass-gapped Dirac cone. This implies that the Dirac cone mass-gapped is smaller at the boundaries of the sandwiched graphene than at the center. For Ni(111) nanostructures in the PC state, the changes in the induced magnetic moment affect the size of the Stoner gap between the spin majority and spin minority channels. These characteristics are discussed in detail in the next section.

5.3 Colossal In-Plane Magnetoresistance of Graphene

Figure 5.3 and Figure 5.4(c) show the transmission probability of electrons through sandwiched graphene from our proposed system when the Ni(111) nanostructures are in the PC and APC states, respectively. When the Ni(111) nanostructures were in the PC state, the transmission probability profile for the proposed system is similar to that of the pristine graphene, as shown in Figure 5.3. The typical transmission probability of the pristine graphene originates from the Dirac cone of graphene, where the transmission probability results in zero conductance at the Fermi energy and increases linearly with energy. The slight increase in the total transmission probability comes from spin-up electrons that transmit through graphene and Ni(111) nanostructures. Thus, spin-up electrons have a higher transmission probability than the spin-

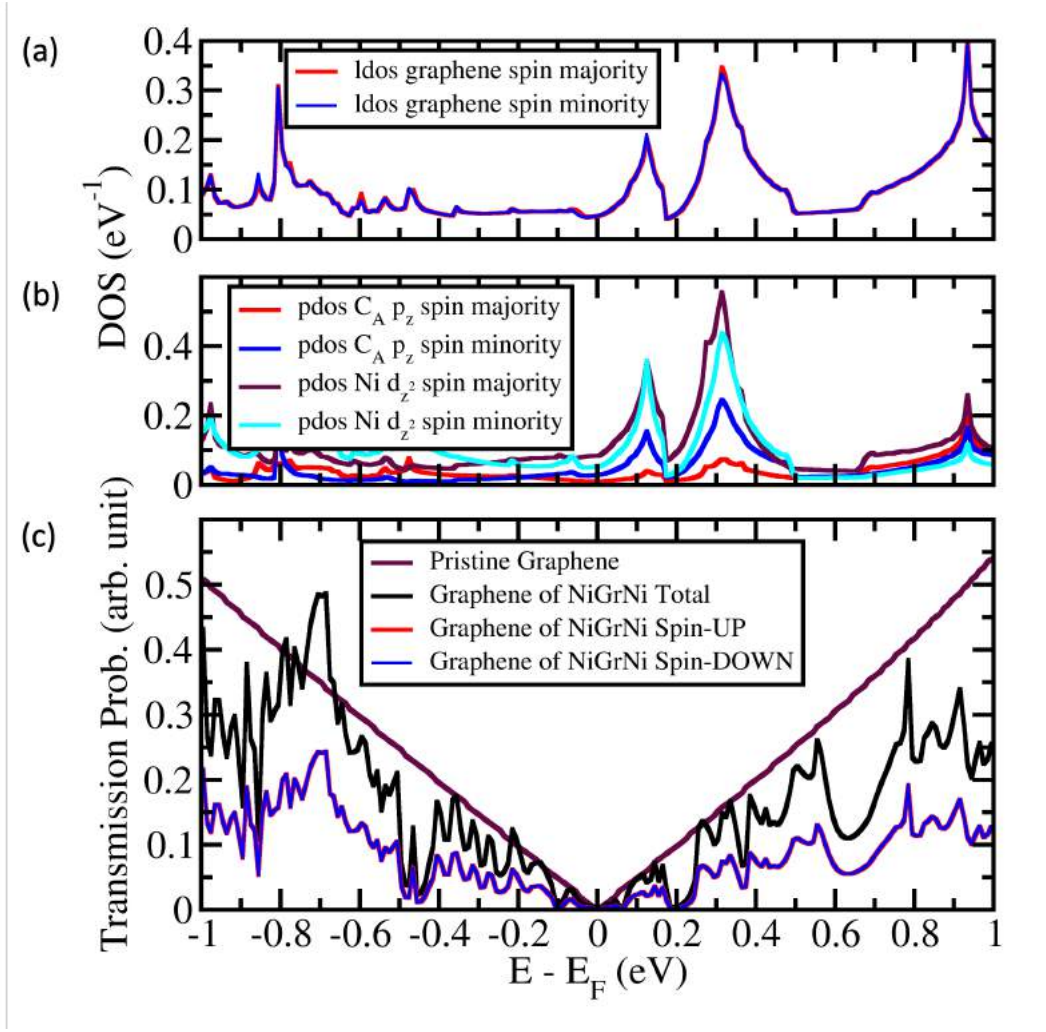


Figure 5.4: (a) The local density of states (LDOS) of graphene in Ni/graphene/Ni MTJ, (b) projected density of states (PDOS) of C_A and Ni at interface hybridized with C_A , and (c) the transmission probability of graphene from the proposed system when Ni(111) nanostructure in APC state.

down electrons.

Further, a profile similar to that of the pristine graphene was observed when the Ni (111) nanostructures were in the APC state, as shown in Figure 5.4(c). However, a unique gap-like transmission probability was found at $E - E_F = 0.18 - 0.22$ eV and $0.58 - 0.78$ eV, with its lowest transmission probability at $E - E_F = 0.2$ and 0.65 eV, respectively. To understand the origin of the gap-like transmission, local density of states (LDOS) and projected density of states (PDOS) calculations were performed on the Ni/graphene/Ni MTJ, which represents the sandwiched part of the proposed system. The LDOS of graphene, shown in Figure 5.4(a), suggests that the Dirac-cone-like density of states (DOS) which was observed at $E - E_F = 0.2$ eV corresponds to the

gap-like transmission probability found at $E - E_F = 0.2$ eV . This relation was observed in the spin majority and minority channel. This Dirac-cone-like DOS is originated from the hybridization between d_{z^2} -orbital of Ni atoms at the interface and p_z -orbital of C atoms (Figure 5.4(b)). The Dirac-cone-like DOS profile at $E - E_F = 0.2$ eV, which was observed in LDOS of graphene, was also found in both the PDOS of p_z -orbital of CA atoms and d_{z^2} -orbital of Ni atoms below CA atoms, implying the characteristics of hybridization (Figure. 5(b)).

The gap-like transmission probability at $E - E_F = 0.65$ eV results from the opening mass-gapped Dirac cone of graphene (Figure 5.4(a)). However, compared to the mass-gapped Dirac cone of graphene shown in Figure 5.4(a), the width of the transmission probability gap of the proposed system is smaller. Furthermore, the transmission probability at $E - E_F = 0.65$ eV is considerably high, unlike the LDOS of graphene in Figure 5.4(a); the DOS at $E - E_F = 0.65$ eV is almost zero similar to DOS at $E - E_F = 0.2$ eV. This difference is because the induced magnetic moment differs between the C atoms at the boundaries and center of the sandwiched graphene, thereby leading to different mass-gapped size and a parabolic transmission probability gap with smaller gap size. Moreover, the small width of Ni (111) nanostructure does not optimize the induced magnetic moment on graphene and a constant value is not achieved, thereby resulting considerably high conductance at $E - E_F = 0.65$ eV. However, this also implies that, when a width of Ni(111) nanostructures is considered in the nanometer scale, the transmission probability at $E - E_F = 0.65$ eV will be as low as at $E - E_F = 0.2$ eV.

By comparing the transmission probability of electrons of the Ni(111) nanostructures in APC and PC states, a high and colossal in-plane MR ratio of up to 3100% and 284% was observed at $E - E_F = 0.2$ and 0.65 eV, respectively(Figure 5.5(a)). Applying a gate voltage to the proposed system shifts the Fermi energy^{39,40} to $E - E_F = 0.2$ eV resulting in a colossal in-plane MR ratio (Figure. 6(b)). Interestingly, this high in-plane MR ratio can be achieved just by sandwiching graphene with Ni(111) nanostructures with an atom-scale width of 12.08 Å. By increasing the width of Ni(111) nanostructure to the nanometer scale, a colossal MR ratio of > 3100% can be expected at $E - E_F = 0.65$ eV because in APC state the gap-like transmission will be nearly zero similar to that at $E - E_F = 0.2$ eV; however, the transmission probability is higher than that at $E - E_F = 0.2$ eV when PC state is considered.

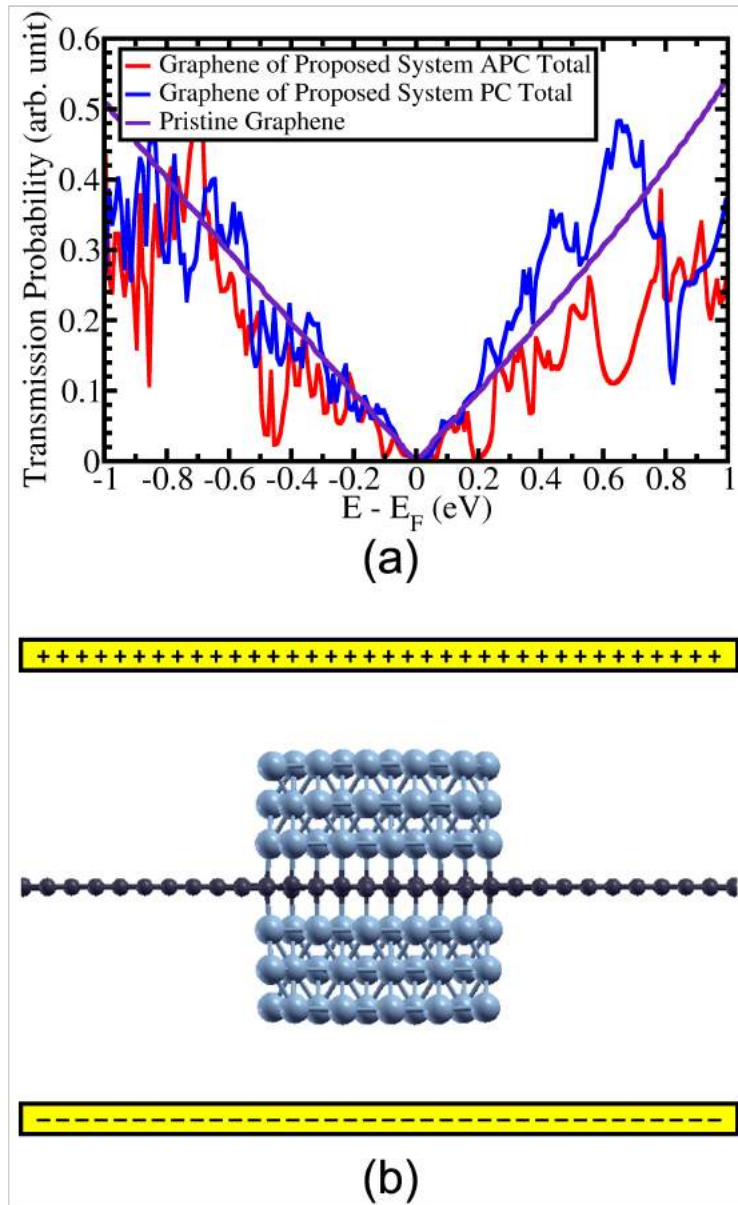


Figure 5.5: (a) The comparison of transmission probability of graphene from the proposed system between APC and PC states. (b) The configuration of gate voltage on the proposed system to shifting the Fermi energy.

5.4 Summary

In this study, we investigated the in-plane conductance of graphene, where the Ni(111) nanostructures with a width of 12.08 Å are sandwiched in the center of the graphene. Both the APC and PC states of the Ni(111) nanostructures were considered. The induced magnetic moment was observed on the sandwiched graphene and could be controlled using the magnetic alignment of the Ni(111) nanostructures. When APC (PC) state is considered, we observed that the carbon atoms of sublattices A and B of the sandwiched graphene had an antiferromagnetic (ferromagnetic) order. Both spin configurations lead to a controllable mass-gapped Dirac cone in the sandwiched graphene. The mass-gapped Dirac cone is open (closed) for APC (PC) state due to the modulated (equi-) potential between the C_A and C_B of the sandwiched graphene.

When the Ni(111) nanostructures were in the PC state, the transmission probability of the proposed system produces a profile similar to that of the pristine graphene. Furthermore, a slight increase in the total transmission probability was observed from spin-up electrons that transmit through graphene and the Ni(111) nanostructures. Thus, spin-up electrons have a higher transmission probability than the spin-down electrons.

However, for the Ni (111) nanostructures in the APC state, a unique gap-like transmission probability was observed from $E - E_F = 0.18-0.22$ eV and $0.58-0.78$ eV with the lowest transmission probability at $E - E_F = 0.2$ and 0.65 eV, respectively. The gap-like transmission probability at $E - E_F = 0.2$ eV comes from the Dirac-cone-like DOS shown in the local density of sandwiched graphene due to the hybridization property between the d_{z^2} -orbital of Ni atoms at the interface and p_z -orbital of C atoms. On the other hand, the gap-like transmission probability at $E - E_F = 0.65$ eV comes from the opening mass-gapped Dirac cone of graphene. However, the gap-like transmission probability was smaller than that found in the LDOS of graphene in Ni/graphene/Ni MTJ. This is because the induced magnetic moment decayed from the center part of the sandwiched graphene toward the boundary, leading to a parabolic shape for the transmission probability gap.

Finally, high and colossal in-plane MR ratios of up to 3100% and 284% were observed at $E - E_F = 0.2$ and 0.65 eV. By applying a gate voltage, the Fermi energy can be controlled resulting in a colossal in-plane MR ratio. Furthermore, by increasing the width of the Ni(111) nanostructure to the nanometer scale, a colossal MR ratio $>3100\%$ can be expected because the gap-like transmission is nearly zero at $E - E_F = 0.65$ eV in the APC state but

having higher the transmission probability than that at $E - E_F = 0.2$ eV in the PC state.

Chapter 6

The Importance of Proximity Effect in 2D Materials-based Magnetic Junctions and Its Relation to Tunneling Magnetoresistance

6.1 Introduction

A successful control on the graphene's MGDC and getting colossal IMR ratio has been discussed previously in chapter 4 and 5, respectively. Thus, an optimization to create a successful design of a graphene-based spin-valve structure spintronics device need to be performed. The optimization was needed for realization of the actual device and for ensuring a performance comparable to that predicted in this theoretical study. The chemical bonding between the Ni slabs and graphene in Ni/graphene/Ni needs to be perfect to get control on graphene's MGDC. This perfect surface can be realized experimentally; however, it is relatively difficult. Thus, to avoid a complete change in the IMR of graphene due to a defect at the Ni/graphene interface, a barrier is necessary to maintain the graphene Dirac cone, although some defect occurs on the Ni surface. Furthermore, when the chemical bonding between Ni and graphene lead to difficult control of graphene's Fermi Energy. By creating the barrier, an easier controllability of graphene's Fermi energy will be expected, as shown in Fig. 6.1 . Prior to further investigation on the effectivity of proximity effect on controlling MGDC of graphene, understanding how the Ni(111) surface

state as evanescent wave work on graphene created magnetic proximity effect is necessary.

Prior to further investigation on the effectivity of proximity effect on controlling MGDC of graphene, understanding how the Ni(111) surface state as evanescent wave work on graphene created magnetic proximity effect is necessary. In this chapter, a theoretical study is conducted to understand the origin of the magnetic proximity effect in 2D material which was sandwiched with ferromagnetic metal. In this study, a Ni/*n*hBN/Ni magnetic junctions with $n = 2, 3, 4,$ and 5 were considered. The study will show that the proximity effect has a close relation to the tunneling transport of Ni/*n*hBN/Ni magnetic junctions when CPP scheme is considered. The study will also answer the reason why the TMR ratio of 2D materials-based MTJ is reducing when the thickness of 2D materials is increased and why 2D materials-based MTJ give such a low TMR ratio.

At first, a study on Ni/2hBN/Ni magnetic junctions will show that the Ni's surface state (111) is the main contribution to the tunneling transmission of the electrons when electrons flow from one Ni slab to another through two hBN layers. When the number of hBN is increased to three, the Ni(111) slabs' surface state still survives, giving a magnetic proximity effect on middle hBN. However, the magnetic proximity effect on middle hBN is weak enough since the d_{z^2} -orbital of the Ni(111) surface state works on unfilled p_z -orbital of B atoms. However, the d_{z^2} -orbital of the Ni(111) surface state works significantly on the graphene layer since it works on π -orbital of graphene. Further study was performed to understand the effectivity of proximity effect on controlling MGDC of graphene.

6.2 Transmission Mechanism of Ni/hBN/Ni MTJs with Different Numbers of hBN Layers

The pd-hybridizations at both the upper and lower interfaces between the Ni slabs and hBN stabilize the system. This chemical property between Ni and hBN is also based on the unique electron transmission phenomenon appearing in hBN-based junctions. A large amount of evidence supporting this idea is presented below.

Fig. 6.2 shows the TMR ratio of 2D material-based MTJs as a function

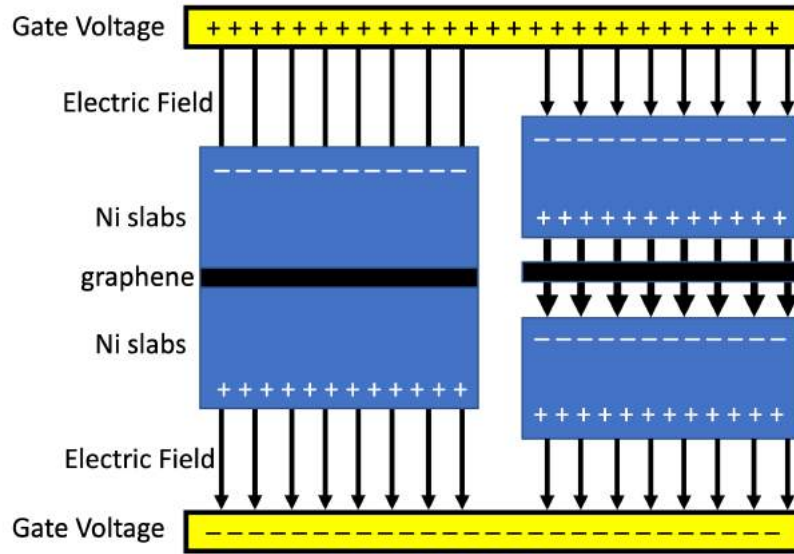


Figure 6.1: The possible charges response when electric field is introduced to the chemical bonding-based interface found in Ni/graphene/Ni MJ (left) and van der Waals-based interface found in Ni/hBN-graphene-hBN/Ni MJ (right).

of the number of 2D material layers as an insulator barrier. The black line shows the TMR values, which were taken at the Fermi energy, namely the zero-bias limit, for various numbers of hBN layers. The TMR ratio profile is in good agreement with a previous theoretical study [44] and is consistent with several experimental studies [54]. When a double-hBN layer with two stacked hBN planes (2hBN) is considered as a tunnel barrier, the TMR ratio increases compared with a monolayer of hBN. This increase was due to the difference in the transmission process of the electrons. When a monolayer of hBN is considered as a tunnel barrier, due to pd-hybridizations from both upper and lower Ni slabs coupled with N atoms, charge transfer occurs, leading to the hBN layer becoming metallic [92]. Thus, the propagating wave electrons become the dominant contributor to the transmission between the two Ni(111) electrodes.

In addition, when 2hBN is used as a tunnel barrier, because of the weak van der Waals interaction between the two hBN layers, electrons are transmitted through the tunnel barrier via the Ni(111) surface state at the interface. This transmission process can be observed from the transmission probability profile of the Ni/2hBN/Ni system, as shown in Fig. 6.3(a). In the case of the Ni/hBN/Ni MTJ, the high transmission peak in the minority spin channel, which is observed when the system in the PC state is located at the Fermi energy [92]. However, for the Ni/2hBN/Ni MTJ, as shown in Fig. 6.3(a),

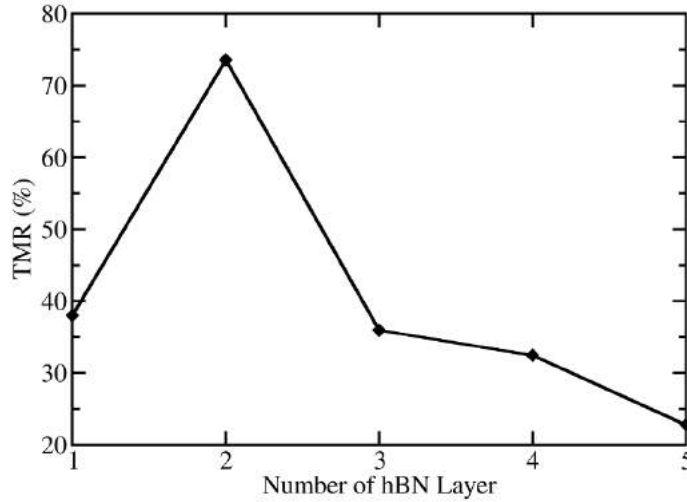


Figure 6.2: The TMR ratio vs the number of 2D materials layers as tunnel barrier at two different energies; $E - E_F = 0$ eV (the zero-bias limit) and 0.34 eV (the highest peak of spin-down electrons transmission probability in PC state started from $n = 3$).

the high transmission peak in the minority spin channel is shifted toward an energy higher than the Fermi energy by 0.28 eV.

On the other hand, the local density of states (LDOS) of hBN at the interfaces in Fig. 6.3(b) shows newly created states at the insulator gap of hBN. Furthermore, the LDOS of those states shows a correlation with the profile of the transmission probability of the system, whereby an increase in the density of states at an energy higher than the Fermi energy in the spin minority channel corresponds to a high transmission peak in the spin minority channel. Therefore, these states are the dominant contributors to electron transmission through the insulator barrier. The projected band structure in Fig. 6.3(c) shows that these states originate from the Ni(111) surface state with major d-components. The high transmission peak observed at an energy higher than the Fermi energy in the spin minority channel corresponds to the d_{z^2} -orbital of Ni(111) at the interfaces that hybridize with the p_z -orbital of the N atoms. Simultaneously, the flat and broad states in Fig. 6.3(b) correspond to the s-orbital of Ni(111) at the interface. The relatively larger components in the d_{z^2} -orbitals compared with the p_z -orbitals suggest that the wavefunction is indeed in a tunnel regime, where 2hBN behaves as a potential barrier for the Ni d -electrons.

When the number of hBN layers is increased further, for example, 3hBN, the contribution from these surface states at the Fermi energy is quenched. The surface states of Ni(111), which are derived from the s-orbital of the sys-

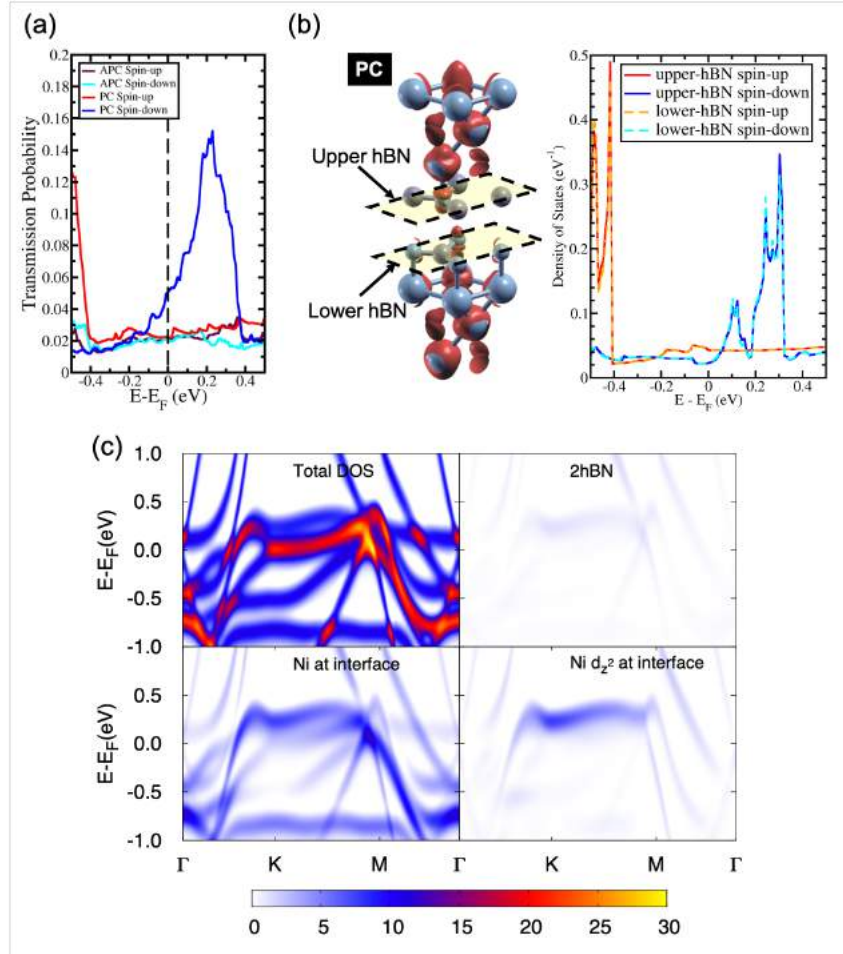


Figure 6.3: (a) The transmission probability of Ni/2hBN/Ni, (b) The spin- charge density mapping (red color represent spin-up charge density mapping) and LDOS of 2hBN insulator barrier in Ni/2hBN/Ni system in PC state, (c) The projected bandstructure of Ni/2hBN/Ni for spin minority channel.

tem with more than two hBN layers, became weaker around the Fermi energy, as shown in Fig. 6.4(b). This quenching leads to a decrease in the transmission probability of electrons in the spin minority channel of the PC state at the Fermi energy, which is approximately equivalent to the transmission probability of electrons in the APC state, as shown in Fig. 6.4(a). This result reduces the TMR ratio of the system at the Fermi energy, which is lower than that observed for Ni/2hBN/Ni. Furthermore, when the number of hBN layers is further increased to 4hBN and 5hBN, a monotonic decrease in the TMR ratio with respect to the increasing number of hBN layers is expected just around the Fermi energy.

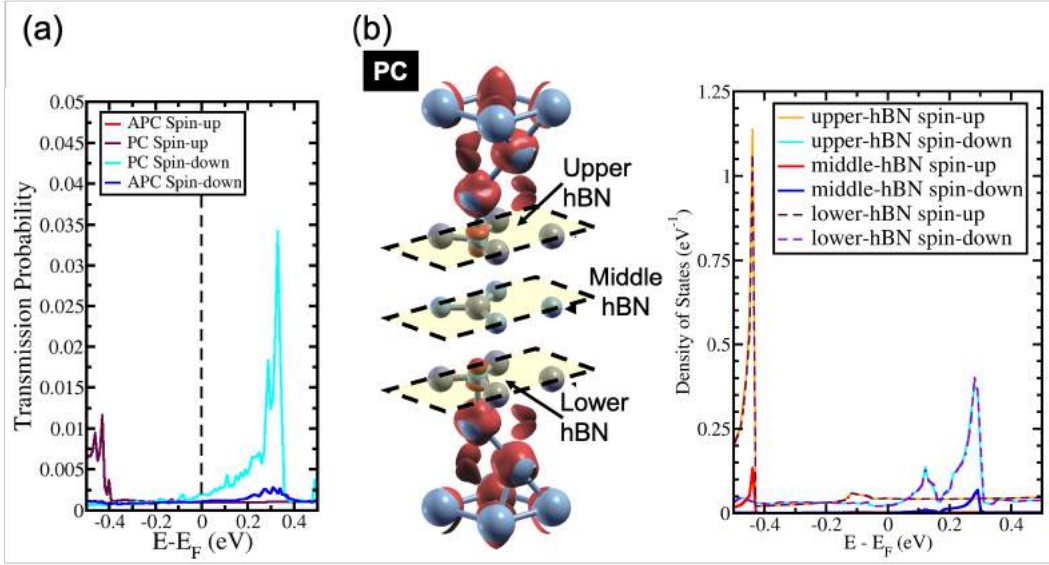


Figure 6.4: (a) The transmission probability of Ni/3hBN/Ni and (b) The spin charge density mapping of Ni/3hBN/Ni in PC state (red color represent spin-up charge density mapping) and LDOS of 3hBN insulator barrier in Ni/3hBN/Ni system in PC state.

6.3 High Transmission Magnetoresistance on the Excited State and Influence of the Proximity Effect

In the last section, the presence of a peak in the transmission probability is discussed. As shown in Fig. 6.3 and Fig. 6.4, The high transmission peak of electrons in the spin minority channel, when the MTJ is in the PC state, was observed at an energy slightly higher than Fermi energy ($E - E_F = 0.28$ eV for Ni/2hBN/Ni and $E - E_F = 0.34$ eV for Ni/3hBN/Ni). Interestingly, this high transmission peak of electrons is still present upon further increasing the number of hBN layers. From the transmission probability of electrons of Ni/ n hBN/Ni with $n = 4$ and 5, the peak of the high transmission probability of electrons in the spin minority channel, when the MTJ is in the PC state, was also observed at an energy of 0.34 eV higher than the Fermi energy, as shown in Fig. 6.4 (a) and (c), which is the same as Ni/3hBN/Ni. Interestingly, it was found that, at $E - E_F = 0.34$ eV for Ni/ n hBN/Ni with $n = 1 - 4$, a high and increasing TMR ratio is observed, but decrease when $n = 5$ as shown by red line in Fig. 6.2. To understand this behavior, further investigation was performed on the electronic state of the insulator barrier for the Ni/ n hBN/Ni system with $n = 4$ and 5.

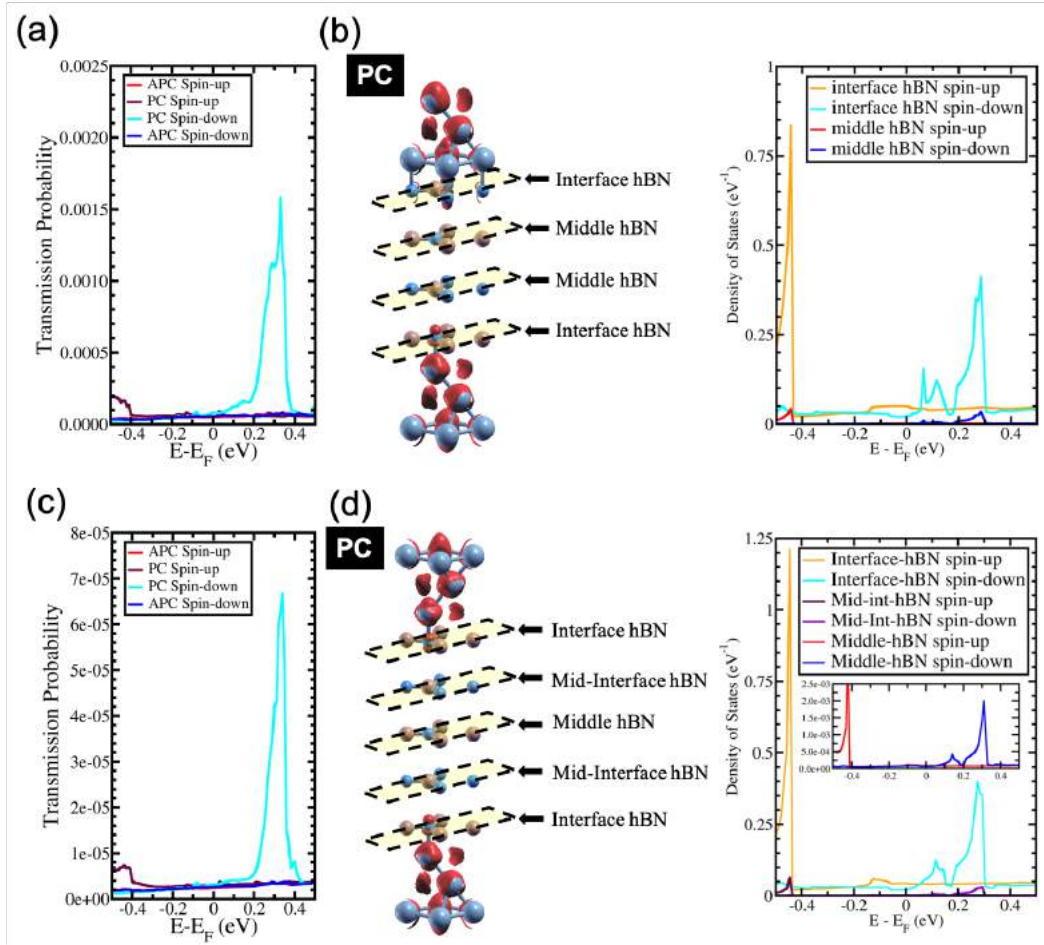


Figure 6.5: (a) The transmission probability of Ni/4hBN/Ni, (b) The charge density mapping of Ni/4hBN/Ni (red color represent spin-up charge density mapping) and the LDOS of 4hBN insulator barrier of Ni/4hBN/Ni system in PC state, (c) The transmission probability of Ni/5hBN/Ni, and (d) The charge density mapping of Ni/5hBN/Ni (red color represent spin-up charge density mapping) and the LDOS of 5hBN insulator barrier of Ni/5hBN/Ni system in PC state (insert: magnified LDOS of middle hBN of Ni/5hBN/Ni system).

The LDOS of the hBN layer in the insulator barrier for the Ni/nhBN/Ni system with $n = 4$ and 5 are shown in Fig. 6.5 (b) and (d), respectively. Looking on the LDOS of hBN in insulator barrier for $n = 3, 4,$ and 5 , a typical behavior corresponding to the presence of the magnetic proximity effect, which is the penetration depth of the spin polarization of a magnetic metal (Ni) into a nonmagnetic material (hBN), is observed. This proximity effect, which causes an evanescent wave, or a dumping mode inside hBN, is found as an LDOS of hBN layer, at $E - E_F = 0.34$ eV, gradually decrease when hBN become far from interface. However, the LDOS at $E - E_F = 0.34$ eV still survives even for middle hBN in the Ni/5hBN/Ni system. Sharp dumping is observed because the proximity effect of d_{z^2} acts on the p_z orbital of B, which is unoccupied.

At an energy close to the Fermi energy, because the energy gap of hBN does exist, no real propagating modes in the hBN slab are expected. On the other hand, at $E - E_F = 0.34$ eV, because a small LDOS is still observed through all hBN in the tunnel barrier, propagating modes in the hBN slab are expected. Thus, for the case of Ni/nhBN/Ni with $n > 2$, the proximity effect becomes the main contribution for the transmission of electron with energy around 0.34 eV through the hBN tunnel barrier

This tunneling behavior causes an interesting filtering effect. When the energy range is 0.34 eV higher than the Fermi energy, in the PC state, the minor-spin channel exhibits a high transmission probability. In contrast, for the major-spin channel, the transmission is significantly reduced. The high transmission for the minor-spin channel originates from the d-orbital nature, because a large pd-hybridization causes a spin-split LDOS with a large peak at the corresponding energy. Thus, except for the d channel, a lower transmission can only be expected. Therefore, the major spin component exhibited reduced transmission. As a result, the ratio of the minority-spin transmission and majority-spin transmission should become more prominent as n increases. This large transmission probability is found only when a parallel-spin configuration is selected, with the pd-hybridization occurring on both sides of the hBN.

In the case of APC, a blocking behavior was observed. An optimum blocking behavior was observed when 4hBN or more was used as an insulator barrier. On Ni/3hBN/Ni, in the APC state, the spin majority and spin minority still show a small transmission probability (but still higher than the transmission probability of spin majority in the PC state). This result is due to the fact that the middle hBN is not spin polarized owing to the opposite proximity effect acting on it from the lower and upper Ni/hBN interfaces. Thus, the blocking behavior is not perfect and leads to a small number of electrons passing through the insulator barrier for both the spin minority and majority. However, in the case of Ni/4hBN/Ni, two middle hBN have oppositely spin polarized each other, making the blocking behavior much stronger and resulting in a lower electron transmission probability for both spin majority and minority, which shows similar transmission probability value as spin majority in the PC state. Together with electrons high transmission of spin minority channel in PC state, as a result, the TMR ratio also becomes significant at a sharp LDOS position of 0.34 eV above the Fermi energy.

When adding more hBN as an insulator barrier to 5hBN, the transmission probability at an energy of 0.34 eV is reduced, as shown by the red line in

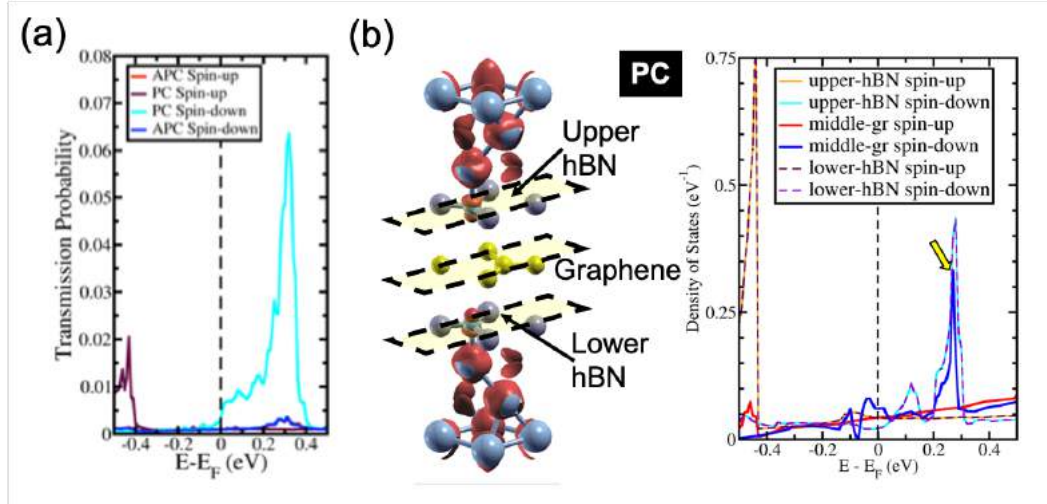


Figure 6.6: (a) The transmission probability of Ni/hBN-Gr-hBN/Ni and (b) The spin charge density mapping of Ni/hBN-Gr-hBN/Ni (red color represent spin-up charge density mapping) and LDOS of hBN-Gr-hBN insulator barrier of Ni/hBN-Gr-hBN/Ni system in PC state.

Fig. 6.2. This is because, although the blocking effect has become stronger since 4hBN is used as an insulator barrier, when 5hBN is considered, the proximity effect found in the middle hBN becomes weaker. This is clearly shown in Fig. 6.5(d), where the LDOS of the middle hBN at $E - E_F = 0.34$ eV become much smaller than that of the middle-interface and interface hBN. This smaller LDOS leads to a significant reduction in the peak transmission of minority spin electrons in the PC state compared to that in the Ni/4hBN/Ni system. Therefore, the TMR ratio was reduced and became smaller than that of the Ni/4hBN/Ni system.

Interestingly, the effect of proximity can be magnified when the hBN layer is replaced with a graphene layer. For example, by replacing the unhybridized hBN layer of the Ni/3hBN/Ni MTJ with graphene, Ni/hBN-Gr-hBN/Ni was formed, as shown in Fig. 6.6 (b). The interface connection from Ni to hBN was found very similar between Ni/3hBN/Ni and Ni/hBN-Gr-hBN/Ni junctions, since Ni-N interlayer distance is 2.05 \AA for both of junctions. The LDOS of the hBN-Gr-hBN insulator barrier is shown in Fig. 6.6 (b). The LDOS of hBN at the interface in Fig. 6.6 (b) is very similar to that of the upper (or lower) hBN in Ni/3hBN/Ni. However, there is a clear difference in the LDOS of graphene from the middle hBN of Ni/3hBN/Ni. Fig. 6.6(b) shows a 6-times higher electronic density of states on graphene at $E - E_F = 0.34$ eV compared to the center hBN in Ni/3hBN/Ni MTJ for the spin-down channel. Thus, these states lead to a higher transmission probability for the corresponding

energy. As shown in Fig. 6.6 (a), a high magnetoresistance ratio of 1200% was observed for the Ni/hBN-Gr-hBN/Ni MTJ at $E - E_F = 0.34$ eV. This high magnetoresistance ratio is higher than that of the Ni/4hBN/Ni MTJ, as shown in Fig. 6.2 but has a similar thickness to Ni/3hBN/Ni. The high performance and unique characteristics of the Ni/hBN-Gr-hBN/Ni MTJ could provide novel functionalities, such as optically induced MTJs, which are introduced in the following section.

6.4 Proposed Design and Mechanism of Optically Induced MTJs

The proposed idea of using a Ni/hBN-Gr-hBN/Ni MTJ as an optically induced MTJ is shown in Fig. 7. The process of reading and writing data in memory using light irradiation was considered here. For the writing process, as discussed in a previous study, optical demagnetization using a circularly polarized femtosecond or sub-picosecond laser and field-assisted magnetic switching can change the magnetic orientation of the free Ni(111) ferromagnetic layer [93]. The high performance and unique characteristics of the Ni/hBN-Gr-hBN/Ni MTJ are primarily used in the reading process. Two Au electrodes were used to flow the current into the proposed MTJ device. A small bias voltage was applied. First, the current flowed from the Au electrode to the transparent electrode on top of the Ni/hBN-Gr-hBN/Ni MTJ. Without any light irradiation onto the system, the reading process cannot be optimally carried out because the current passing through the MTJ is relatively small in both APC and PC states. This is because at the Fermi energy, the electron transmission for the APC and PC states is low, as explained in the previous section. Reading conditions 1 and 2 are shown in Fig. 7 (b). When linearly polarized light, for example, infrared or visible light, is used on the upper Ni slabs to excite electrons below the Fermi energy to an energy of 0.34 eV higher than the Fermi energy, the optimal reading process is observed. The condition 3. Fig. 7 (b) shows that a high transmission occurs in the PC state, resulting in the flow of current through the MTJ towards the lower Au electrode. In addition, condition 4 shows that the MTJ is in the APC state, thus explaining the observed low transmission.

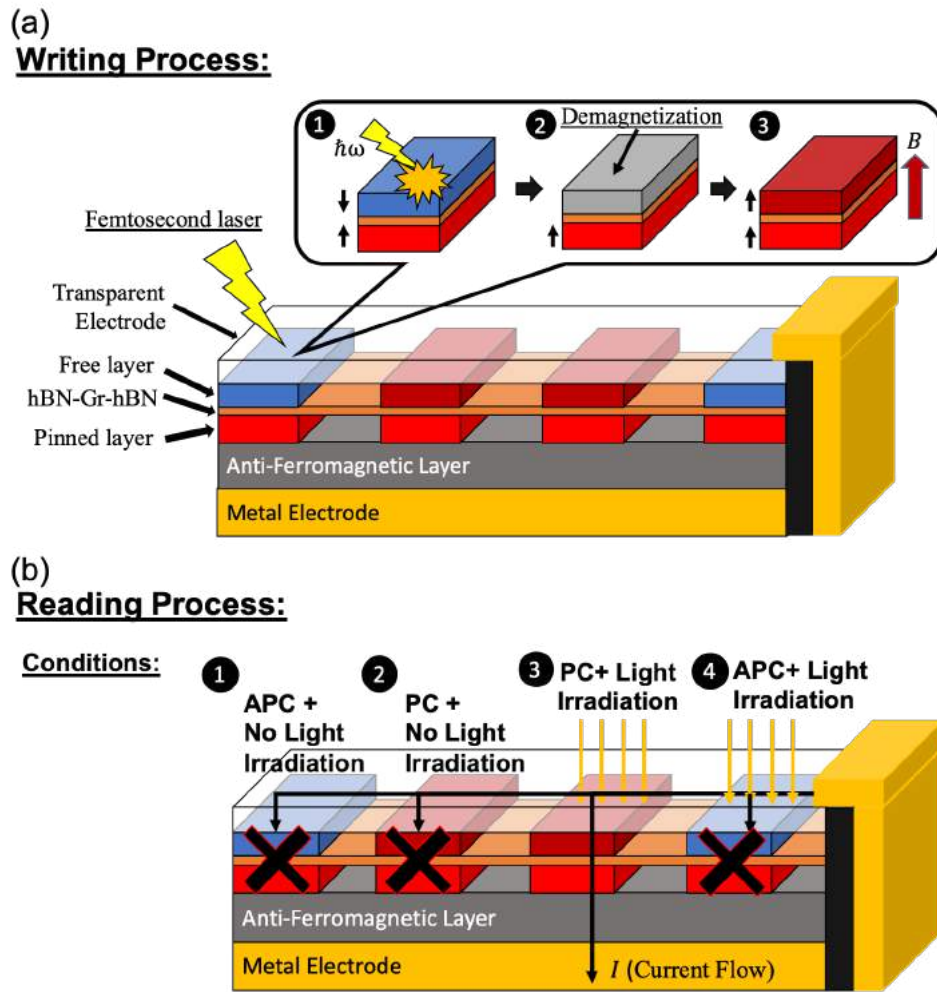


Figure 6.7: (a) The writing and (b) the reading process of Ni/hBN-Gr-hBN/Ni proposed MTJ device with light irradiation.

6.5 Summary

The Ni/nhBN/Ni MTJs were investigated by increasing the number of hBN layers in the tunnel barrier. Owing to the electron transmission through the surface states, an increasing TMR ratio was observed when considering 2hBN as the tunnel barrier compared with the case of a monolayer hBN. However, a monotonic decrease in TMR was observed when more than two hBN layers were considered. This behavior is attributed to the quenched surface states of Ni(111) at the Fermi energy, which occur at the insulator gap of hBN.

On the other hand, it was found that the Ni/nhBN/Ni MTJ exhibited a slight shift in the highest transmission peak toward an energy higher than the Fermi energy. This result is attributed to electron transmission through Ni d_{z^2} which hybridized with N p_z . Interestingly, a high and increasing TMR ratio

was observed at the energy where the high transmission peak was located. These results are due to the proximity effect of the unhybridized hBN layer. The effect of proximity can be magnified when the hBN layer is replaced with a graphene layer. When Ni/3hBN/Ni was considered and the unhybridized hBN layer in Ni/3hBN/Ni was replaced with a graphene layer, a stronger proximity effect became evident through the higher electronic density of states at the corresponding energy for the LDOS of graphene. Thus, these states lead to a higher transmission probability for the corresponding energy. A high magnetoresistance ratio of 1200% was observed for the Ni/hBN-Gr-hBN/Ni MTJ at an energy of 0.34 eV.

The high performance and unique characteristics of this Ni/hBN-Gr-hBN/Ni MTJ make it possible to exploit a novel device functionality, namely, that of an optically induced MTJ. The process of reading and writing in the proposed MTJ is expected to be conducted by light irradiation. Optical demagnetization and field-assisted magnetic switching are expected to change the magnetic orientation of the free Ni(111) ferromagnetic layer. This process represents the writing process of the proposed device. On the other hand, the unique characteristics of the Ni/hBN-Gr-hBN/Ni MTJ would mainly contribute to the reading process. The linear polarization of light was applied to induce the transmission to occur at energies higher than the Fermi energy by 0.34 eV. This process was used to read the magnetic alignment of the Ni/hBN-Gr-hBN/Ni MTJ.

Chapter 7

Effect of interface on the graphene Dirac cone control in a Ni/hBN-graphene-hBN/Ni magnetic junction

7.1 Introduction

After understanding the origin of proximity effect on the 2D materials tunnel barrier in the previous chapter 6, further study was performed to understand the effectivity of proximity effect on controlling MGDC of graphene. In this chapter, a study in which the magnetic proximity effect of the Ni surface state was used to control the pseudospin of graphene is presented. This study presents a theoretical study on the Ni/hBN–Graphene interface of Ni/hBN–Gr–hBN/Ni system in controlling mass gapped Dirac cone (MGDC) of graphene. The MGDC of graphene is controlled through its pseudospin term, similar to the previous Ni/graphene/Ni system which has been discussed in chapter 4. However, in this study, the magnetic proximity effect controlled the potential of graphene’s carbon atom sublattice A (C1) and B (C2). The graphene layer was sandwiched between monolayer hBN and followed by Ni(111) nanostructures to introduce the magnetic proximity effect on the graphene layer. At the interface, 12 stacking configurations of hBN layers and graphene were considered. The calculation was performed when Ni(111) slabs were both in APC and PC state. In this study, we investigate the influence of Ni(111) ’s surface state as an evanescent wave that works on different sites of graphene on the electronic structure of graphene. Our

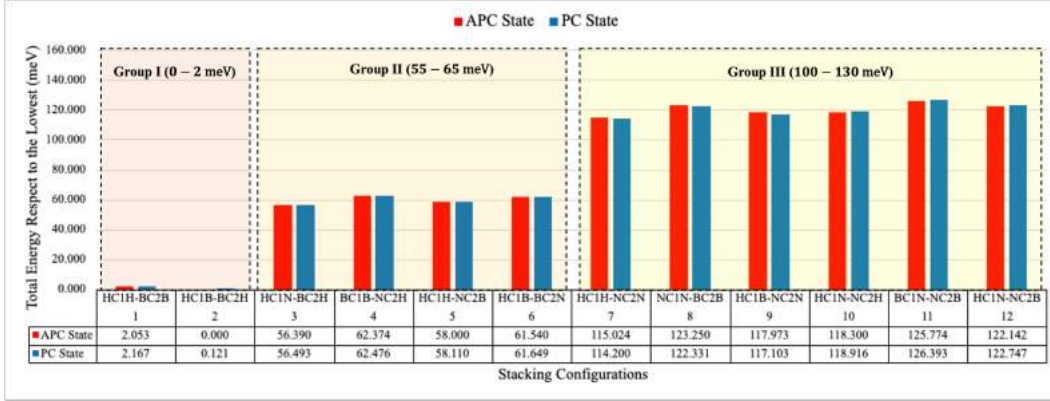


Figure 7.1: The relative total energy respect to lowest energy for all proposed stacking configuration and its classification into three groups.

results suggested that the 12 stacking configurations can be categorized into three groups, each corresponding to van der Waals interaction between hBN and graphene based on the relative total energy. Each group shows unique characteristics in controlling graphene mass gapped. The magnetic proximity effect and weak hybridization from the Ni(111) surface state as an evanescent wave plays a major role in determining the characteristics of MGDC. Finally, a device that can move the upper and lower Ni(111)/hBN slabs translationally is proposed as a possible application of the Ni/hBN–Gr–hBN/Ni magnetic junctions as a spin-mechatronics device.

7.2 Total energy and magnetic properties of Ni/hBN–graphene–hBN/Ni

Fig. 7.1 shows the relative total energy of all 12 stacking configurations in the APC and PC states to the lowest total energy. The lowest total energy was shown by the HC1B–BC2H stacking configuration. From Fig. 7.1, based on the relative total energy range to the lowest energy, the 12 stacking configurations can be classified into three categories. The first category (group I) is the stacking configurations with a relative total energy range of 0–2 meV. This category consists of HC1H–BC2B and HC1B–BC2H stacking configurations. The second category (group II) is the stacking configurations with a relative total energy range of 55–65 meV, i.e., HC1N–BC2H, BC1B–NC2H, HC1H–NC2B, and HC1B–NC2N. Finally, the third category (group III) is the stacking configurations with a relative total energy range of 100–130 meV, i.e., NC1N–HC2H, NC1N–BC2B, HC1B–NC2N, HC1N–NC2H, BC1N–NC2B, and

No.	Stacking Arrangement Name	Interlayer distance (Å)			
		N-Gr		B-Gr	
		upper	lower	upper	lower
1	HC1H-BC2B	2.71	2.71	2.85	2.85
2	HC1B-BC2H	2.71	2.71	2.85	2.85
3	HC1N -BC2H	2.74	2.76	2.88	2.90
4	BC1B-NC2H	2.77	2.76	2.91	2.89
5	HC1H- NC2B	2.76	2.75	2.90	2.88
6	HC1B- BC2N	2.76	2.78	2.89	2.92
7	HC1H- NC2N	2.79	2.79	2.93	2.93
8	NC1N -BC2B	2.81	2.81	2.95	2.95
9	HC1B- NC2N	2.80	2.81	2.94	2.94
10	HC1N-NC2H	2.80	2.80	2.94	2.94
11	BC1N-NC2B	2.83	2.83	2.96	2.96
12	HC1N-NC2B	2.81	2.82	2.95	2.95

Table 7.1: The interlayer distance between upper/lower hBN with graphene for all stacking configurations.

HC1N–NC2B. The stacking configurations are classified into three groups corresponding to van der Waals bonding interactions between hBN and graphene layers.

Tabel 7.1 shows the interlayer distance between the hBN and graphene for both upper and lower hBN. Tabel 7.1 shows that group I, has the shortest interlayer distance between hBN and graphene compared to other groups, although it has the lowest relative total energy range. This is because of the interaction between the localized electron density of hBN on N atoms and the π -orbital of graphene. The van der Waals bonding between hBN and graphene is the strongest when N atoms are not placed on the top or below the C atoms of graphene because the repulsive electron screening interaction between C atoms of graphene and N atoms of hBN was reduced. Furthermore, when N atoms of hBN are placed on the top or below C atoms of graphene, the relative total energy increases. This increase because the repulsive electron screening

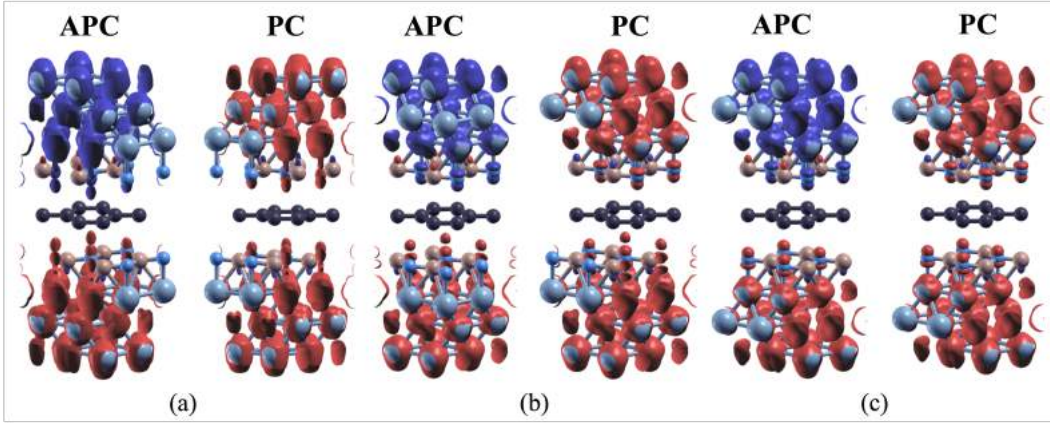


Figure 7.2: Spin charge density mapping of Ni/hBN-Gr-hBN/Ni magnetic junctions in (a)HC1B-BC2H, (b)BC1B-NC2H, and (c)BC1N-NC2B stacking configurations for APC and PC states. (Red color represent spin-up charge density and blue color represent spin-down charge density)

interaction becomes stronger and leads to the weaker van der Waals bonding, resulting in a bigger interlayer distance between hBN and graphene layers. The interlayer distance of the stacking configuration in group II, is shown in Tabel 7.1. When one of the hBN layers (either lower or upper) placed the N atoms on the top or below C atoms, the interlayer distance between that hBN and graphene became greater than group I. When both upper and lower hBN layers place the N atoms on the top and below the C atoms of graphene, as shown in group III, the relative total energy increases even more. The increase in the relative energy corresponds to the bigger interlayer distance between hBN and graphene. This result agrees with the study on hBN–graphene–hBN stacking in previous shapter 6. However, in this case, the charge transfer from Ni atoms at the interface to N atoms of hBN results in additional electron screening at the interface. It strengthens the electron screening repulsion between hBN and graphene, categorizing the 12 stacking configurations into three groups becomes more clearer than in the previous study.

Furthermore, the total energy difference between the APC and PC states is relatively small for all 12 stacking configurations. Suggesting that the magnetic coupling between two Ni slabs is relatively weak. Fig. 3 shows the spin-charge density mapping for each group represented by BC1H–HC2B (group I), BC1B–NC2H (group II), and BC1N–NC2B (group III). The induced magnetic moment occurred on hBN layers is consistent with the studies discussed in chapter 6 in which the hybridized N atoms have induced magnetic moment with the same spin direction as Ni atoms. This characteristic is true for all stacking configurations. For the case of graphene, the induced magnetic

No.	Stacking Arrangement Name	Magnetic Moment (μ_B)			
		APC		PC	
		C1	C2	C1	C2
1	HC1H-BC2B	0.000	0.000	0.002	0.003
2	HC1B-BC2H	0.001	-0.001	0.002	0.002
3	HC1N-BC2H	-0.006	0.005	-0.004	0.006
4	BC1B-NC2H	-0.005	0.006	0.006	-0.003
5	HC1H-NC2B	-0.004	0.005	0.007	-0.002
6	HC1B-BC2N	0.004	-0.004	0.007	-0.002
7	HC1H-NC2N	0.000	0.000	-0.011	0.015
8	NC1N-BC2B	0.000	0.000	-0.014	0.015
9	HC1B-NC2N	0.000	0.001	0.015	-0.012
10	HC1N-NC2H	0.012	-0.012	0.002	0.002
11	BC1N-NC2B	-0.010	0.010	0.003	0.003
12	HC1N-NC2B	-0.011	0.011	0.002	0.002

Table 7.2: The induced magnetic moment on C atoms in sublattice A (C1) and sublattice B (C2) of graphene in both APC and PC states.

moment is unclear (Fig. 7.2). However, Table 7.2 shows that a small but non-negligible induced magnetic moment was observed on graphene. Interestingly, the induced magnetic moment on graphene is based on the stacking configuration. Therefore, the total energy difference between APC and PC states might come from the induced magnetic moment configuration, which occurs on C atoms of graphene layers due to the proximity effect of Ni surface states.

Table 7.2 shows the induced magnetic moment on C atoms in sublattice A (C1) and sublattice B (C2). For group I, the proximity effect only works on π -orbital of graphene since the Ni atoms at interface hybridized with N atoms of hBN and N atoms was placed on top and below of hollow site of graphene. This means that the Ni surface state as the evanescent wave does not directly affect the spin-charge density of C atoms. Therefore, when the PC state is considered, a small but non-negligible induced magnetic moment on C atoms is observed, as shown in Table 7.2. However, there is a slightly different characteristic between HC1H-BC2B and HC1B-BC2H stacking configurations. In HC1H-BC2B, the magnetic moment of C2 atoms is higher than that of C1 atoms. This resulted from B atoms being located on top and below C2 atoms and the induced magnetic moment on B atoms slightly induced a magnetic moment on C2 atoms by giving an additional $0.001 \mu_B$ higher than that of C1 atoms. This reason also explains the equal magnetic moment on HC1B-BC2H

since upper and lower B atoms are located below or above different graphene sublattices. However, when the APC state is considered, different behavior of induced magnetic moment between HC1H–BC2B and HC1B–BC2H stacking configurations is observed. In both stacking configurations, since the position of N atoms of upper and lower hBN is symmetric to graphene, the proximity effect is canceled out on the π -orbital of graphene. For the case of HC1H–BC2B, the induced magnetic moment, which comes from B atoms proximity effect, is also canceled out since both upper and lower the B atoms are located above and below C2 atoms. However, for the case of HC1B–BC2H, since B atoms are located on different sublattices, thus a small induced magnetic moment of $0.001 \mu_B$ is observed on C1 and C2 with having antiferromagnetic order.

When the stacking configuration of group II is considered, one of two hBN layers, either the lower or upper, has the N atoms, which hybridized with Ni atoms at the interface, placed in line with C atoms. Here, the proximity effect from one of the hBN/Ni slabs perturbs the electrons of C atoms directly. When the PC state is considered a larger induced magnetic moment on C atoms affected by the surface state of hybridized Ni was observed compared to that found in the stacking configuration of group I. In the case of APC state, since the position of N atoms is not symmetric, *i.e.*, one placed on the top/below of C atoms and another placed on top and below hollow site, an obvious induced magnetic moment on graphene was observed. The antiferromagnetic (AFM) order on the induced magnetic moment of C1 and C2 but having the same amplitude comes from the half-filled p_z -orbital and Pauli exclusion principles are often found in organic molecules in sp^2 hybridization or magnetic alternant hydrocarbon system [88]

For the stacking configuration in group III, the induced magnetic moment on graphene depends on the position of N atoms in the upper and lower hBN, *i.e.*, symmetric or asymmetric. In group III, the N atoms of hBN layers were placed on top and below of C atoms. Thus, it is considered symmetric when N atoms of the upper and lower hBN layer agrees one-C atom of graphene. However, it is considered asymmetric when N atoms of the upper and lower hBN layer agree with different sublattices of C atoms, *e.g.*, upper hBN in line with C1 and lower hBN in line with C2. The most significant induced magnetic moment was observed upon symmetric stacking configurations and PC state compared with other stacking configurations. The proximity effect from the Ni slabs upper and lower were summed up on one of the C atoms and created an antiferromagnetic order of induced magnetic moment between C1

and C2 atoms. However, when the APC state was considered, the proximity effect from upper and lower Ni slabs canceled out, resulting in zero induced magnetic moment on graphene. When asymmetric stacking configurations were considered, the induced magnetic moment of graphene is also significant when the system is in the APC state. This characteristic comes from the proximity effect of upper and lower Ni slabs working on different C atoms of graphene. Since the upper and lower Ni slabs have an opposite direction and graphene prefers to have antiferromagnetic order; thus, the induced magnetic moment of C1 and C2 atoms reinforce each other. However, when the system is in a PC state, the proximity effect creates ferromagnetic order induced magnetic moment on C atoms, but near to zero since the effect is reduced due to the antiferromagnetic nature of C atoms of graphene.

7.3 Controllable Dirac cone of graphene due to tunable pseudospin term of graphene

Table 7.3 shows the predicted spin-charge density $n_{\eta,\sigma}$ where η is either C1 or C2 and σ is either spin-up (\uparrow) or spin-down (\downarrow). The value of $n_{\eta,\sigma}$ is assumed to be determined by integrating $n_{\sigma}(r)$ within an ionic radius of the carbon atom. This spin-charge density contributes to determining the potential of C1 and C2 atoms, corresponding to Dirac cone perseverance. Both HC1H–BC2B and HC1B–BC2H stacking configurations have N atoms above and below the hollow site of the graphene layer for the group I stack configurations. However, where HC1H–BC2B (HC1B–BC2H) are symmetrically positioned (asymmetrically), the location of B atoms is different. This difference affects the spin-charge density on C1 and C2. In HC1H–BC2B stacking configuration, since upper and lower B atoms are located on top and below of C2 atoms, a modulated spin-charge density between C1 and C2 is expected. From Table 7.3, it shows that upon the system in APC state,

$$n_{C2,\uparrow} = n_{C2,\downarrow} > n_{C1,\uparrow} = n_{C1,\downarrow}. \quad (7.1)$$

The difference found between $n_{C2,\sigma}$ and $n_{C1,\sigma}$ comes from the van der Waals interaction between the C2 and B atoms. From Equation 7.1, the potentials between C1 and C2 atoms are modulated, resulting in an open gapped Dirac cone, as shown in Fig. 7.3(a). Since the spin-charge density difference between spin-up and spin-down electrons is the same, thus the band structure of spin-

No.	Stacking Arrangement Name	Integrated spin charge density ($n_{\eta\sigma}$)											
		APC						PC					
		C1		C2		C1-C2		C1		C2		C1-C2	
		spin-up	spin-down	spin-up	spin-down	spin-up	spin-down	spin-up	spin-down	spin-up	spin-down	spin-up	spin-down
1	HC1H-BC2B	1.997	1.997	1.964	1.964	0.033	0.033	1.998	1.996	1.965	1.962	0.033	0.034
2	HC1B-BC2H	1.979	1.978	1.978	1.979	0.001	-0.001	1.980	1.978	1.980	1.978	0.000	0.000

Table 7.3: The integrated spin-charge density of C1 and C2 in APC and PC states for HC1H-BC2B and HC1B-BC2H stacking configurations.

No.	Stacking Arrangement Name	Integrated spin charge density											
		APC						PC					
		C1		C2		C1-C2		C1		C2		C1-C2	
		spin-up	spin-down	spin-up	spin-down	spin-up	spin-down	spin-up	spin-down	spin-up	spin-down	spin-up	spin-down
3	HC1N-BC2H	1.975	1.981	1.991	1.986	-0.016	-0.005	1.976	1.980	1.991	1.985	-0.015	-0.005
4	BC1B-NC2H	1.992	1.997	1.973	1.967	0.019	0.030	1.997	1.991	1.969	1.972	0.028	0.019
5	HC1H-NC2B	1.970	1.974	1.997	1.992	-0.027	-0.018	1.976	1.969	1.993	1.995	-0.017	-0.026
6	HC1B-BC2N	1.979	1.975	1.985	1.989	-0.006	-0.014	1.981	1.974	1.986	1.988	-0.005	-0.014

Table 7.4: The integrated spin-charge density of C1 and C2 in APC and PC states for HC1N-BC2H, BC1B-NC2H, HC1H-NC2B and HC1B-BC2N stacking configurations.

No.	Stacking Arrangement Name	Integrated spin charge density											
		APC						PC					
		C1		C2		C1-C2		C1		C2		C1-C2	
		spin-up	spin-down	spin-up	spin-down	spin-up	spin-down	spin-up	spin-down	spin-up	spin-down	spin-up	spin-down
7	NC1N-HC2H	1.994	1.994	1.980	1.980	0.014	0.014	1.988	1.999	1.988	1.973	0.000	0.026
8	NC1N-BC2B	1.976	1.976	1.993	1.993	-0.017	-0.017	1.969	1.983	2.000	1.985	-0.031	0.000
9	HC1B-NC2N	1.986	1.986	1.986	1.985	0.000	0.001	1.994	1.979	1.979	1.991	0.015	-0.012
10	HC1N-NC2H	1.993	1.981	1.981	1.993	0.012	-0.012	1.988	1.986	1.988	1.986	0.000	0.000
11	BC1N-NC2B	1.980	1.990	1.990	1.980	-0.010	0.010	1.986	1.983	1.986	1.983	0.000	0.000
12	HC1N-NC2B	1.974	1.985	1.997	1.986	-0.023	-0.001	1.981	1.979	1.993	1.991	-0.012	-0.012

Table 7.5: The integrated spin-charge density of C1 and C2 in APC and PC states for NC1N-HC2H, NC1N-BC2B, HC1B-NC2N, HC1N-NC2H, BC1N-NC2B and HC1N-NC2B stacking configurations.

majority and minority channels is overlapped. However, when the PC state is considered,

$$n_{C2,\uparrow} > n_{C2,\downarrow} > n_{C1,\uparrow} > n_{C1,\downarrow}. \quad (7.2)$$

showing induced magnetic moment was observed on C1 and C2 atoms. Equation 7.2 indicates that the potentials between C1 and C2 atoms are modulated and spin-polarized, resulting in gapped Dirac cone being open and spin-polarized, as shown in Fig. 7.3(b).

For the case of HC1B–BC2H, in the APC state, the van der Waals interaction between B and C atoms occurs on C1 and C2 atoms. However, a magnetic moment occurs on C atoms which were induced by the magnetic moment on B atoms, resulting in modulated spin-charge density as follows:

$$n_{C1,\uparrow} = n_{C2,\downarrow} > n_{C1,\downarrow} = n_{C2,\uparrow}. \quad (7.3)$$

Equation 7.3 shows that the potentials between C1 and C2 atoms are modulated, and the spin-charge density difference between spin-up and spin-down electrons is the same. Therefore, the gapped Dirac cone is open with spin-majority and minority channel overlap, as shown in Figure. 5(a). However, in the PC state, unlike the HC1H–BC2B stacking configuration showing the gapped Dirac cone is open, HC1B–BC2H shows a closed Dirac cone. This characteristic comes from the asymmetric position of B atoms, which induced the same magnetic moment on C atoms creating an equivalent spin-charge density between C1 and C2 as follows:

$$n_{C1,\uparrow} = n_{C2,\uparrow} > n_{C1,\downarrow} = n_{C2,\downarrow}. \quad (7.4)$$

Thus, the equipotential was expected, preserving a chiral symmetry creating a closed gapped Dirac cone. Further, the spin-charge density between spin-up and spin-down electrons creates the closed Dirac cone polarized, as shown in Fig. 5(b). Finally, the opening and closing of the gapped Dirac cone on HC1B–BC2H stacking configuration, which is the most stable one, show the controllable Dirac cone, which comes from the controllable induced magnetic moment of graphene. Although the gap found in the APC state is relatively small, in the following two sections, the influence of weak hybridization between Ni and C atoms through damped Ni d_{z^2} surface state and C p_z is introduced to widen the gap of the Dirac cone.

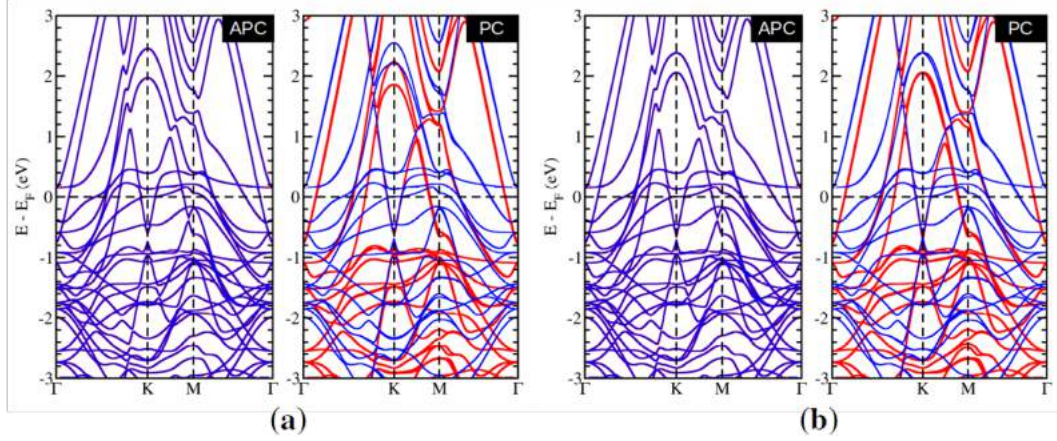


Figure 7.3: The band structure of Ni(111)/hBN-Gr-hBN/Ni(111) in (a) HC1H-BC2B and (b) HC1B-BC2H stacking configurations in both APC and PC states. (Red line represent spin majority channel and blue line represent spin minority channel)

7.4 Influence of the surface state of Ni works directly on C atoms in the gapped Dirac cone

When the N atoms of one of the hBN layers, either upper or lower hBN layer, are in the APC or PC state, a different induced magnetic moment is observed between C1 and C2, as shown in Table 7.4. Thus, a MGDC is observed for both APC and PC state cases, as shown in Fig. 7.4. However, interestingly, the gap size for spin majority and spin minority channels is different and rather significant. For instance, it can be seen on the band structure of HC1N-BC2H. For both APC and PC cases, the spin majority channel has a large bandgap greater than 200 meV, while oppositely, the spin minority has a bandgap smaller than 100 meV. This characteristic can be explained by referring to the integrated spin-charge density for the stacking configuration in group II shown in Table 7.4.

For the case of HC1N-BC2H, when the APC state is considered, the spin-charge density difference of spin-up electrons is almost three times that of spin-down electrons. Therefore, the MGDC is more prominent in the spin majority channel than the spin-minority channel. This significant difference was also found when the PC state was considered. The high difference in spin-up electrons resulted from the Ni surface states' direct influence on C1 atoms. The lower Ni slab has a spin-up direction of the magnetic moment. Thus, the C1 has a spin-down direction of an induced magnetic moment since graphene

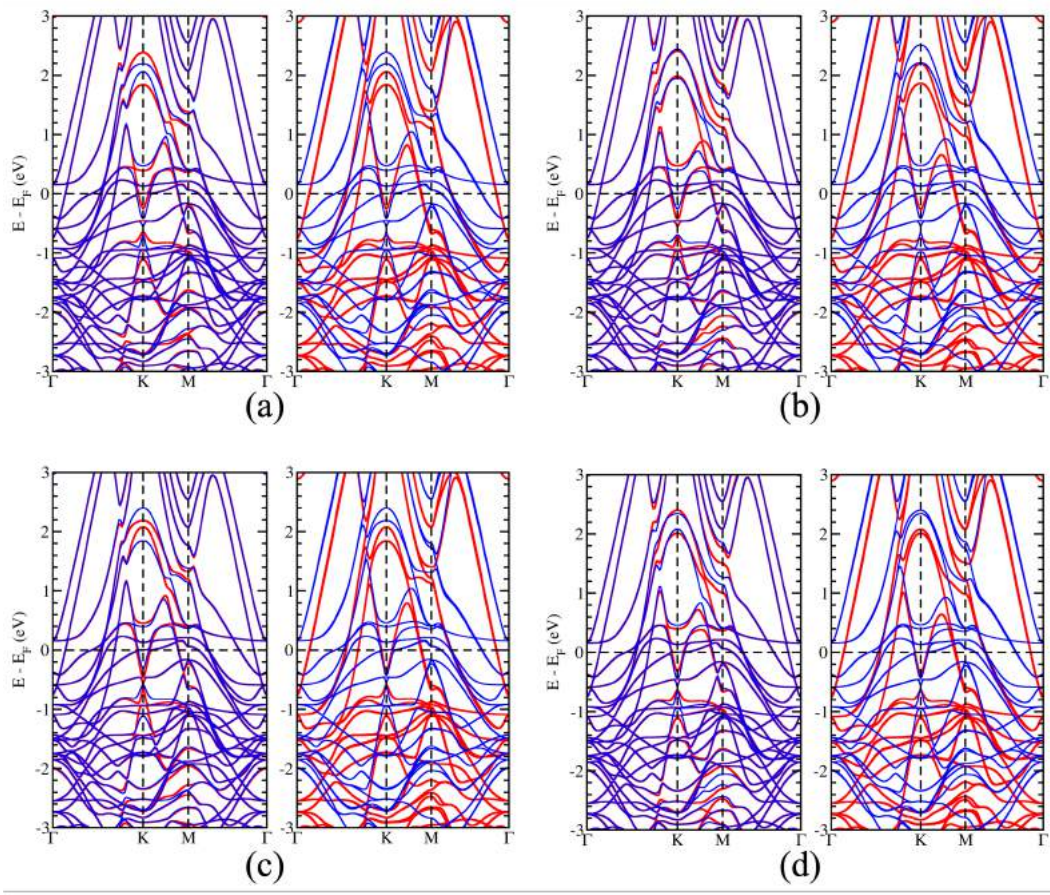


Figure 7.4: The band structure of Ni(111)/hBN-Gr-hBN/Ni(111) in (a)HC1N-BC2H, (b)BC1B-NC2H, (c)HC1H-NC2B and (d)HC1B-BC2N stacking configurations in both APC and PC states.(Red line represent spin majority channel and blue line represent spin minority channel)

prefers to have antiferromagnetic order with the magnetic moment direction of Ni slabs, as shown in Table 7.2. The spin-up electron density is suppressed to be lower than the spin-down electron density, resulting in a big difference in spin-up electron density between C1 and C2.

7.5 Controllable mas-gapped Dirac-cone through Ni surface state influence on C atoms

Both upper and lower Ni slab surface states work on C atoms in group III stacking configuration. The proximity effect of upper and lower Ni slabs on the C atom can be categorized into two: symmetrically (asymmetrically),

in which the surface state works on one-C-atoms sublattice (two different C atoms sublattice). The NC1N–HC2H, NC1N–BC2B, and HC1B–NC2N are symmetric, while HC1N–NC2H, BC1N–NC2B, and HC1N–NC2B are categorized as asymmetric. The symmetric and asymmetric influences give different characteristics on the spin-charge density of graphene; thus, the MGDC.

The symmetric case, e.g., NC1N–HC2H stacking configuration, has zero induced magnetic moment on graphene in the APC state but larger induced magnetic moment than group II in PC state. However, although the induced magnetic moment on graphene is zero in the APC state, Fig. 7.5(a) shows the mass gapped Dirac in the spin majority and minority channel. This result can be explained by looking at Table 7.5. The surface state of Ni influences the spin-charge density of C atoms of graphene, generating different spin-charge density mapping between C1 and C2, although the magnetic proximity effect is canceled out on graphene. Since both upper and lower stacking configuration is symmetric, thus the spin-up and spin-down electron density difference are the same resulting in overlap MGDC on spin majority and minority channel.

For the case of PC, the induced magnetic moments found in C1 and C2 are different. However, the spin-charge density difference between spin-up and spin-down electrons is rather different. For instance, it can be seen in the NC1N–HC2H stacking configuration. It shows that a prominent difference between C1 and C2 electron density is observed for the spin-down electron density. However, for the case of spin-up electron density, a small electron densities difference between C1 and C2 was found instead. This characteristic comes from the magnetic response of C1 atoms, which tend to have anti-ferromagnetic order with Ni atoms. Thus, the spin-down charge density of C1 atoms become larger than the spin-up charge density, while for the C2, the spin-down electron becomes smaller. Thus, the MGDC for spin majority channel is slightly open, while the MGDC in spin minority channel is prominent and bigger than group II, as shown in Fig. 7.5(a). This characteristic is found for all the stacking configurations in group III, which has the asymmetric influence of the proximity effect.

However, for the asymmetric influence of the proximity effect, a similar characteristic as our previous study is observed.²⁴ When the APC state is considered, the surface state of upper-lower Ni slabs works on different graphene sublattices. Thus, different induced magnetic moments on C1 and C2 are observed. This difference led to the chiral symmetry breaking, resulting in mass gapped open on graphene’s Dirac cone for both spin majority and minority

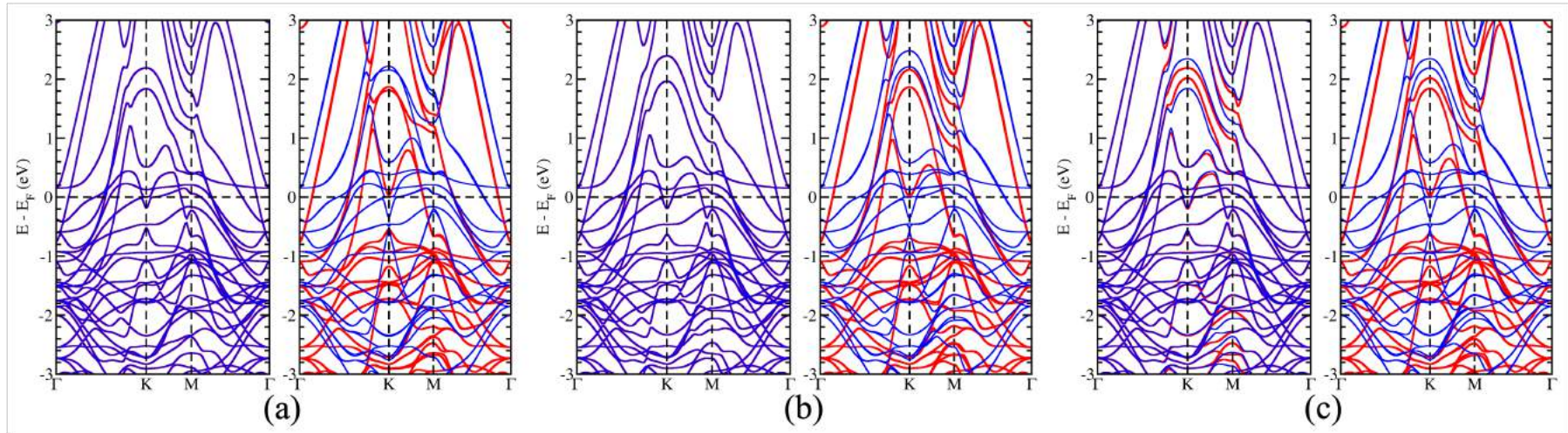


Figure 7.5: The band structure of Ni(111)/hBN-Gr-hBN/Ni(111) in (a)NC1N-HC2H, (b)NC1N-BC2B, and (c)HC1B-NC2N stacking configurations in both APC and PC states.(Red line represent spin majority channel and blue line represent spin minority channel)

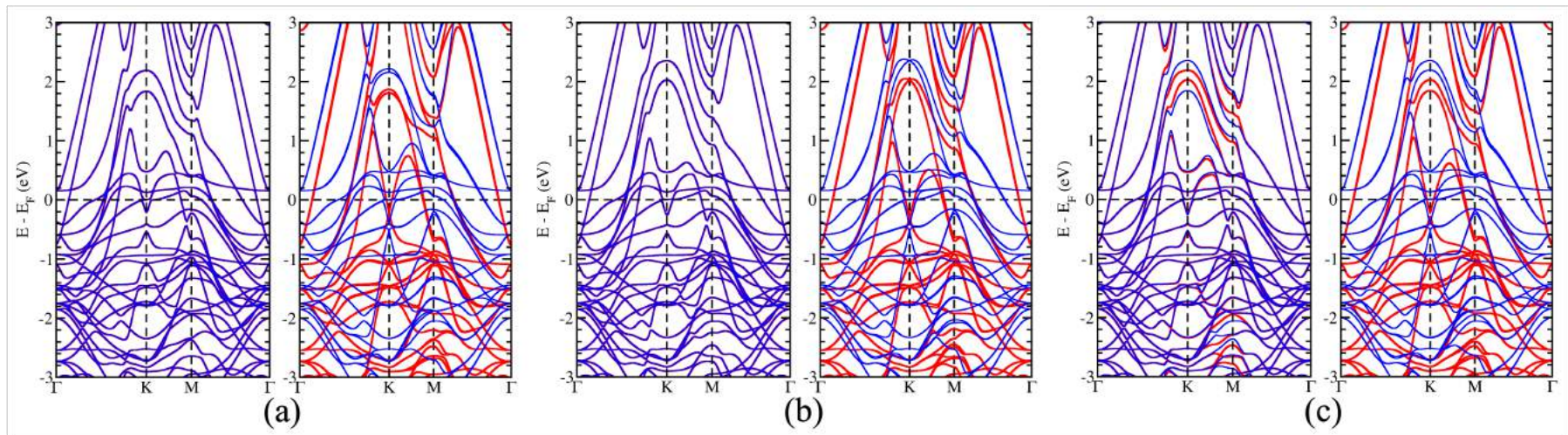


Figure 7.6: The band structure of Ni(111)/hBN-Gr-hBN/Ni(111) in (a)HC1N-NC2H, (b)BC1N-NC2B, and (c)HC1N-NC2B stacking configurations in both APC and PC states.(Red line represent spin majority channel and blue line represent spin minority channel)

channels, as shown in Fig. 7.6. It is in a rather similar case as found in an HC1B–BC2H stacking configuration, but the proximity effect is more prominent since it works directly on C atoms. It can be seen from Table 7.5 that the spin-charge density difference in group III asymmetric is much bigger than that in HC1B–BC2H.

Interestingly, the gap size is comparable to Ni/graphene/Ni magnetic junctions as discussed in chapter 4. Finally, for the case of PC state, the induced magnetic moment on C1 and C2 has the same direction and value. Therefore, a spin-polarized Dirac cone is expected to be observed in Fig. 7.6.

7.6 Possible application on the spin mechatronic valve

The unique characteristics of mass gapped Dirac cone of graphene of Ni/hBN–Gr–hBN/Ni, which depends on the stacking configuration (that can be categorized into three), can be proposed as a device where a controllable MGDC is tuned by using mechanical motion. This is because the van der Waals interaction between hBN and graphene is weak enough so that the hBN can be mechanically translated to create another stacking configuration. Recently, tilting two layers of graphene to have particular angle is experimentally possible, thus, a translation motion can also be expected. Such a device can be proposed by considering APC state on Ni/hBN–Gr–hBN/Ni with the device structure which is shown in Fig. 7.7(a). From the most stable stacking configuration, HC1B–BC2H, the upper slab of Ni/hBN can be shifted to get BC1B–NC2H stacking configuration. Afterwards the lower Ni/hBN slab can be shifted to get BC1N–NC2B stacking configuration. The change of in-plane conductance at energy $E - E_F = -0.3$ eV can be expected by looking on the LDOS of graphene in Fig. 7.7(b) for spin-majority channel and Fig. 7.7(c) for spin-minority channel. At $E - E_F = -0.3$ eV, for spin-up electrons, mass gapped was observed only on BC1N–NC2B stacking configuration, while the other having stacking configuration does not exhibit mass gapped. However, for spin-down electrons, both BC1B–NC2H and BC1N–NC2B stacking configurations exhibit mass gapped, while only HC1B–BC2H does not have mass gapped Dirac cone (MGDC). Therefore, three different non-volatile memory states can occur by changing the stacking configuration from HC1B–BC2H to BC1N–NC2B. Further investigation was necessary to comprehend all the processes and calculate the in-plane transmission probability of the system.

7.7 Summary

This paper investigated the influence of Ni/hBN–Graphene interface of Ni/hBN–Gr–hBN/Ni magnetic junctions in controlling MGDC through proximity effect. The 12 possible stacking configurations were proposed. Both the APC and PC states of the upper and lower Ni slabs were considered for all the 12 stacking configurations. The 12 possible stacking configurations of Ni/hBN–Gr–hBN/Ni magnetic junctions can be categorized into three groups based on the relative total energy to the lowest, which corresponds to the site of graphene the upper-lower Ni surface state work. The first category (group I) is the stacking configurations with a relative total energy range of 0–2 meV. This category consists of HC1B–BC2H, which has the lowest total energy from the 12 stacking configurations, and HC1H–BC2B stacking configurations. The second category (group II) is the stacking configurations with a relative total energy range of 55–65 meV, i.e., HC1N–BC2H, BC1B–NC2H, HC1H–NC2B, and HC1B–NC2N. Finally, the third category (group III) is the stacking configurations with a relative total energy range of 100–130 meV, i.e., NC1N–HC2H, NC1N–BC2B, HC1B–NC2N, HC1N–NC2H, BC1N–NC2B, and HC1N–NC2B.

In group, I, the position of the upper and lower B atoms determines the characteristics of mass gapped Dirac-cone of graphene. When it is symmetric, which is found in a BC1B-HC2H stacking configuration, mas gapped Dirac cone was found open for both APC and PC states with a gap size less than 50 meV. However, when the position of upper and lower B atoms is asymmetric, the mas gapped Dirac-cone is open (close) when APC (PC) state is considered. The gapped mass size found in the APC state is less than 25 meV. This means the magnetic proximity effect from the B atom can preserve or break the chiral symmetry of graphene, although the contribution is rather weak.

For group II, the influence of Ni surface state on mass-gapped Dirac cone of graphene is introduced by either upper or lower Ni slabs, which works directly on the C1 or C2 atom. This configuration led to the opening of mass-gapped Dirac cone with one spin majority channel had big mass-gapped while the other had small mass-gapped for both APC and PC states. The surface state as an evanescent wave works directly on C atoms, creating bigger mass gaps.

For group III, both upper and lower Ni slabs surface states act on C atoms of graphene. The proximity, in this case, is categorized into symmetric when the surface state works only on one sublattice C atoms and the asymmetric when the surface state works on two different sublattices of C atoms. A prominent mass gap is observed in the APC state, and the spin majority and minority

channel overlap for the symmetric one. When the PC state is considered, one of the spin channels has mass-gapped, larger than group II, while the other has considerably small mass-gapped. However, a prominent mass-gapped is observed in the APC state with a spin majority, and a minority channel overlaps for the asymmetric case. The chiral symmetry is preserved in the PC state, resulting in a spin-polarized Dirac-cone.

The unique characteristics of each group in controlling the mass-gapped Dirac cone of graphene can be used for a possible application in the spin-mechatronics device. By fixing the magnetic junctions in the APC state, moving the upper and lower Ni/hBN slabs translationally from HC1B–BC2H to BC1B–NC2H and finally becoming NC1B–BC2N, three different conductance is expected at energy $E - E_F = -0.3$ eV . Thus, a magnetic junction with three non-volatile memory states can be realized.

This page intentionally left blank

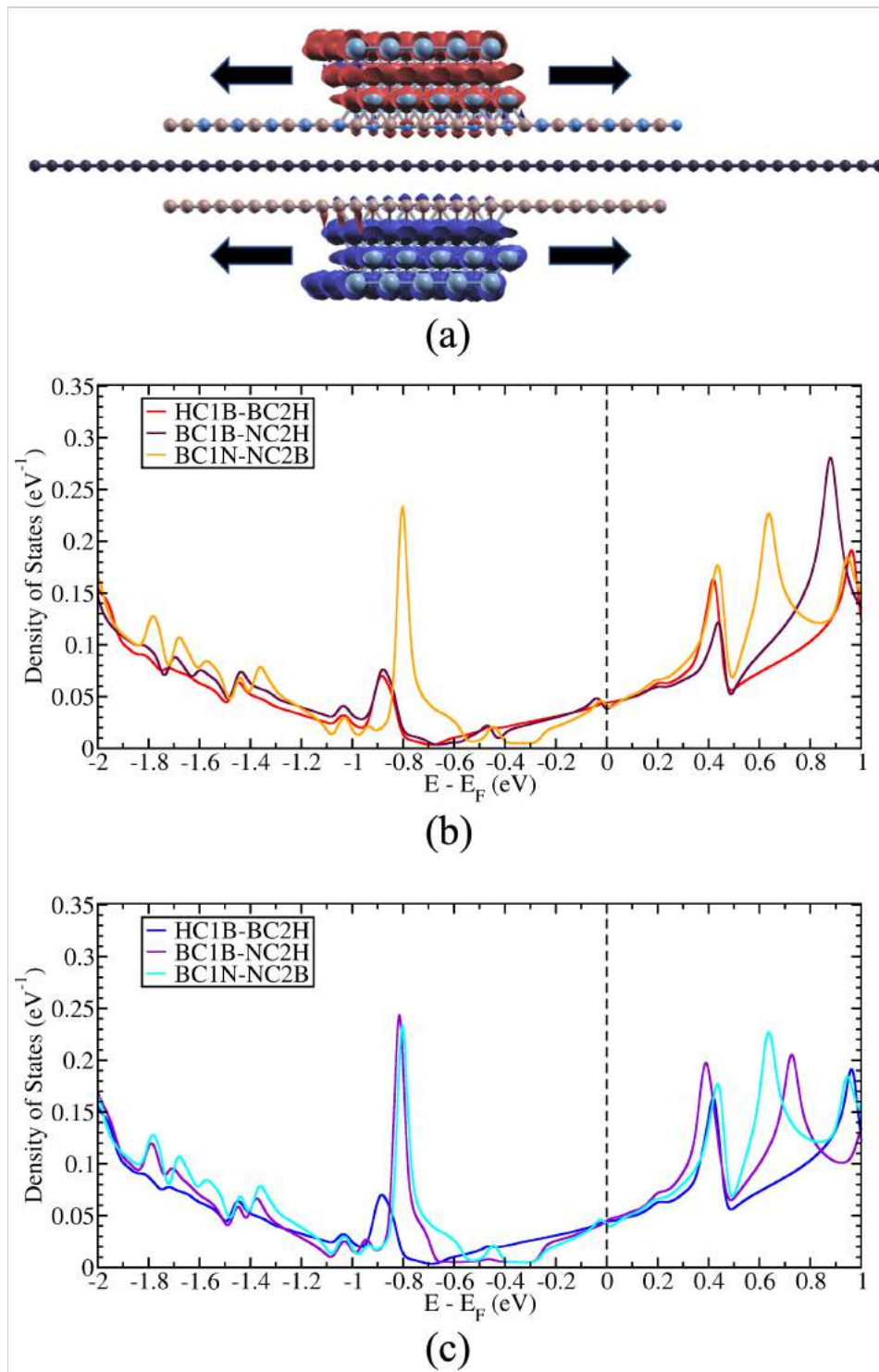


Figure 7.7: The device structure for the proposed application in controlling Dirac cone through mechanical motion. The LDOS of graphene for (a) spin-up and (b) spin-down electrons when Ni/hBN-Gr-hBN/Ni system having HC1B-BC2H, BC1B-NC2H, and BC1N-NC2B stacking configurations.

Chapter 8

CONCLUSIONS

The in-plane conductance of graphene is related to its Dirac cone energy band characteristics, making the electrons in graphene behave peculiarly, having the same velocity and no inertia. The Dirac cone of graphene comes from the perseverance of chiral symmetry of the C atoms in sublattices A and B by having equal potential between two sublattices. Once the potential difference arises between C atoms of sublattices A and B, the chiral symmetry will be broken, and the Dirac cone will create a mass gap. When the Dirac cone of graphene creates a mass gap, low in-plane conductance of graphene is to be expected. Starting from the above facts, this thesis suggests a successful design of a graphene-based spintronic device with high performance by proposing a perspective of in-plane conductivity change of graphene by controlling the Dirac cone of graphene in a non-volatile way.

The design proposed in this thesis to control the Dirac cone of graphene in a non-volatile way is by creating a nano-spin-valve structure of graphene sandwiched by ferromagnetic metal Ni(111) slabs. In this structure, the control of the graphene's Dirac cone characteristics is considered by changing the magnetic alignment of upper and lower Ni slabs, i.e., antiparallel and parallel configuration. It was discussed in 4, that the controllable MGDC of graphene was successfully done. When the magnetic moments of the upper and lower Ni(111) slabs have an antiparallel configuration (APC), the MGDC is open. However, the MGDC is closed in parallel configuration (PC). This unique characteristic is because the most stable arrangement of the Ni/graphene/Ni heterostructure occurs when Ni atoms of the upper and lower Ni(111) slabs at the interfaces are hybridized with different graphene sublattices. In other words, Ni atoms from the lower Ni(111) slab hybridized with C atoms in sublattice A (i.e., C_A), and Ni atoms from the upper Ni(111) slab hybridized with

C atoms in sublattice B (i.e., C_B). Although the C atoms of graphene bond with the Ni atoms, this special hybridization preserves the equipotential between sublattices A and B. Meanwhile, a magnetic moment is induced on the graphene layer by charge transfer from the Ni to C atoms. Therefore, the induced magnetic moments of the CA and CB atoms depended on the magnetic alignment of the Ni(111) slabs. Moreover, the induced magnetic moments in APC and PC between the CA and CB atoms exhibit antiferromagnetic and ferromagnetic orders. This characteristic implies that the pseudospin between sublattices A and B can be controlled to preserve or break the chiral symmetry, making the MGDC controllable.

After the controllable MGDC of graphene was found, the efficiency of this control on the in-plane magnetoresistance of graphene was investigated. From the discussion in chapter 5, the controllable MGDC creates a colossal in-plane magnetoresistance (IMR) ratio for graphene. When an atomic scale width of Ni slabs is considered ($\sim 12.08 \text{ \AA}$) sandwiching some parts of graphene, a colossal IMR up to 3100% was observed at $E - E_F = 0.2 \text{ eV}$. This colossal IMR comes from the electronic states created from pd-hybridization between graphene and Ni slabs. Its characteristics depend on Ni slabs' magnetic alignment; a high (low) density of states is created when the PC (APC) state is considered. On the other hand, when the nanometer scale width of Ni slabs is considered, a colossal IMR beyond 3100% was expected at $E - E_F = 0.65 \text{ eV}$, which corresponds to the controllable MGDC of graphene.

Successful control of the graphene's MGDC and a colossal IMR ratio have been discovered. However, an optimization to create a successful graphene-based spin-valve structure spintronics device needs to be performed. The optimization was needed to realize the actual device and ensure a performance comparable to that predicted in this theoretical study. The chemical bonding between the Ni slabs and graphene in Ni/graphene/Ni needs to be perfect to control graphene's MGDC. This perfect surface can be realized experimentally; however, it is relatively difficult. Thus, to avoid a complete change in the IMR of graphene due to a defect at the Ni/graphene interface, a barrier is necessary to maintain the graphene Dirac cone. Furthermore, the chemical bonding between Ni and graphene leads to difficult control of graphene's Fermi Energy. By creating the barrier, easier controllability of graphene's Fermi energy will be expected. However, prior to further investigation on the effectivity of proximity effect on controlling MGDC of graphene, understanding how the Ni(111) surface state as evanescent wave work on graphene created magnetic

proximity effect is necessary.

Prior to further investigation on the effectivity of proximity effect on controlling MGDC of graphene, understanding how the Ni(111) surface state acts as evanescent wave work on graphene created magnetic proximity effect is necessary. A theoretical study was conducted to understand the origin of the magnetic proximity effect in 2D material, which was sandwiched with ferromagnetic metal. The first investigation was done on a Ni/nhBN/Ni magnetic junctions with $n = 2, 3, 4,$ and 5 . The study shows that the magnetic proximity effect on the hBN layer in the insulator barrier originated from the Ni surface state at the interface, which acts as an evanescent wave works on the hBN layer. The evanescent wave created a new state at the bandgap of hBN, creating an induced magnetic moment. This new state at the bandgap of hBN became the main contribution to the tunneling transport of Ni/nhBN/Ni magnetic junctions when the CPP scheme was considered. The study also answers that the TMR ratio of 2D materials-based MTJ is reduced when the thickness of 2D materials increases due to the damping nature of the Ni surface state. The study also answers that 2D materials-based MTJ gives such a low TMR ratio because the main transmission contribution is from Ni's surface state. The pd -hybridization at the interface leads the surface state of Ni to create a bonding and antibonding nature. Thus, the high MR ratio was not observed on Fermi energy but rather at energy higher and lower than Fermi energy. However, the magnetic proximity effect on middle hBN was weak enough since the d_z^2 -orbital of the Ni(111) surface state works on the unfilled p_z -orbital of B atoms. Thus, replacing the middle hBN in Ni/3hBN/Ni with graphene, a significant induced magnetic moment and proximity state was observed because the d_z^2 -orbital of the Ni(111) surface state works on π -orbital of graphene.

After understanding the origin of the proximity effect on the 2D materials tunnel barrier, further study was performed to understand the effectivity of proximity effect on controlling MGDC of graphene. The controllable induced magnetic moment on graphene is replaced through charge transfer to magnetic proximity effect. The van der Waals interactions between graphene and hBN layers led to easy controllability of graphene Fermi energy by using gate voltage. Furthermore, controlling the induced magnetic moment on graphene can lead to controllable MGDC size. One of the methods is introducing a translational mechanical motion of Ni/hBN slabs. This method leads the system to exhibit three memory states. It opens the opportunity by creating 2D materials-based magnetic junctions to have a memory state of more than two

beyond the conventional magnetic tunnel junctions (MTJs).

Furthermore, it was also discovered that the position of graphene's MGDC (above or below Fermi energy) was related to the bonding at the interface by comparing the position of graphene's MGDC between Ni/graphene/Ni and Ni/hBN-graphene-hBN/Ni nano-spin-valve structures. The difference in charge doping characteristics of graphene's MGDC was found. In the case of Ni/graphene/Ni nano-spin-valve structure, the Fermi energy is located below the graphene's MGDC. This characteristic implies that the graphene is positively charged doped. However, the position of the Fermi energy below the MGDC comes from the creation bonding and antibonding state due to pd -hybridization between C and Ni atoms at the interface. This fact can be proved by looking at the Fig. 4.2, where the Dirac-cone was observed below and above Fermi energy, indicating bonding and antibonding states, respectively.

On the other hand, in Ni/hBN-graphene-hBN/Ni case, the Fermi energy is located above the graphene's MGDC. This characteristic implies that the graphene is negatively charged doped. Moreover, unlike Ni/graphene/Ni junction, Ni/hBN-graphene-hBN/Ni does not have strong pd -hybridization between C and Ni atoms. Thus, no bonding-antibonding Dirac-cone was observed on all 12 stacking configurations of Ni/hBN-graphene-hBN/Ni in chapter 7. This negatively charged graphene originated from electrical polarization on hBN at the Ni/hBN interface, where the hBN is positively charged. The positively charged hBN comes from its pyramidal structure at the interface [92]. Due to its pyramidal structure, the B atoms have a negative dipole moment while N atoms have a positive dipole moment. Since N atoms are much closer to graphene, thus graphene becomes slightly negatively charged.

Understanding the chemical and physical properties of the interface in graphene-based magnetic junctions becomes a foundation for realizing a spintronic device based on graphene in-plane conductance. The findings of possible control of graphene MGDC through two different characteristics of the interface (chemical bonding and physical bonding) and the observed colossal IMR ratio presented in this thesis become a significant development in realizing high-performance 2D materials-based spintronic device having high performance. Furthermore, the new findings on the functionality beyond the conventional spintronic device open insight into the novel device of spintronic device.

Bibliography

- [1] M. N. Baibich, J. M. Broto, A. Fert, F. Nguyen Van Dau, F. Petroff, P. Etienne, G. Creuzet, A. Friederich, and J. Chazelas. Giant magnetoresistance of (001)fe/(001)cr magnetic superlattices. *Phys. Rev. Lett.*, 61:2472–2475, Nov 1988.
- [2] G. Binasch, P. Grünberg, F. Saurenbach, and W. Zinn. Enhanced magnetoresistance in layered magnetic structures with antiferromagnetic interlayer exchange. *Phys. Rev. B*, 39:4828–4830, Mar 1989.
- [3] Candid Reig, Susana Cardoso, and Subhas Chandra Mukhopadhyay. *Giant Magnetoresistance (GMR) Sensors: From Basis to State-of-the-Art Applications*. Springer, Berlin, Heidelberg, 1 edition, 2013.
- [4] M. Julliere. Tunneling between ferromagnetic films. *Physics Letters A*, 54(3):225–226, 1975.
- [5] S. Maekawa and U. Gafvert. Electron tunneling between ferromagnetic films. *IEEE Transactions on Magnetics*, 18(2):707–708, 1982.
- [6] Claude Chappert, Albert Fert, and Frédéric Nguyen Van Dau. The emergence of spin electronics in data storage. *Nature Materials*, 6:813 EP –, 2007.
- [7] H. Dery, P. Dalal, Ł. Cywiński, and L. J. Sham. Spin-based logic in semiconductors for reconfigurable large-scale circuits. *Nature*, 447:573 EP –, 05 2007.
- [8] Jian-Gang (Jimmy) Zhu and Chando Park. Magnetic tunnel junctions. *Materials Today*, 9(11):36–45, 2006.
- [9] Jeffrey R. Childress and Robert E. Fontana. Magnetic recording read head sensor technology. *Comptes Rendus Physique*, 6(9):997–1012, 2005.

- [10] E. Chen, D. Apalkov, Z. Diao, A. Driskill-Smith, D. Druist, D. Lottis, V. Nikitin, X. Tang, S. Watts, S. Wang, S. A. Wolf, A. W. Ghosh, J. W. Lu, S. J. Poon, M. Stan, W. H. Butler, S. Gupta, C. K. A. Mewes, T. Mewes, and P. B. Visscher. Advances and future prospects of spin-transfer torque random access memory. *IEEE Transactions on Magnetism*, 46(6):1873–1878, 2010.
- [11] Muhammad Iqbal, Nabeel Qureshi, and Ghulam Khan. *Recent Advancements in 2D-Materials Interface Based Magnetic Junctions for Spintronics*, volume 457. Elsevier, 02 2018.
- [12] J Bass and W.P Pratt. Current-perpendicular (cpp) magnetoresistance in magnetic metallic multilayers. *Journal of Magnetism and Magnetic Materials*, 200(1):274–289, 1999.
- [13] A. B. Granovsky, M. Ilyn, A. Zhukov, V. Zhukova, and J. Gonzalez. Giant magnetoresistance of granular microwires: Spin-dependent scattering in intergranular spacers. *Physics of the Solid State*, 53(2):320–322, 2011.
- [14] T. Miyazaki and N. Tezuka. Giant magnetic tunneling effect in fe/al₂o₃/fe junction. *Journal of Magnetism and Magnetic Materials*, 139(3):L231–L234, 1995.
- [15] J. S. Moodera, Lisa R. Kinder, Terrilyn M. Wong, and R. Meservey. Large magnetoresistance at room temperature in ferromagnetic thin film tunnel junctions. *Phys. Rev. Lett.*, 74:3273–3276, Apr 1995.
- [16] W. H. Butler, X.-G. Zhang, T. C. Schulthess, and J. M. MacLaren. Spin-dependent tunneling conductance of Fe|MgO|Fe sandwiches. *Phys. Rev. B*, 63:054416, Jan 2001.
- [17] M. Bowen, V. Cros, F. Petroff, A. Fert, C. Martinez Boubeta, J. L. Costa-Krämer, J. V. Anguita, A. Cebollada, F. Briones, J. M. de Teresa, L. Morellón, M. R. Ibarra, F. Güell, F. Peiró, and A. Cornet. Large magnetoresistance in fe/mgo/feco(001) epitaxial tunnel junctions on gaas(001). *Applied Physics Letters*, 79(11):1655–1657, 2022/05/10 2001.
- [18] Shinji Yuasa, Taro Nagahama, Akio Fukushima, Yoshishige Suzuki, and Koji Ando. Giant room-temperature magnetoresistance in single-crystal fe/mgo/fe magnetic tunnel junctions. *Nature Materials*, 3(12):868–871, 2004.

- [19] Stuart S. P. Parkin, Christian Kaiser, Alex Panchula, Philip M. Rice, Brian Hughes, Mahesh Samant, and See-Hun Yang. Giant tunnelling magnetoresistance at room temperature with mgo (100) tunnel barriers. *Nature Materials*, 3(12):862–867, 2004.
- [20] S. Ikeda, J. Hayakawa, Y. Ashizawa, Y. M. Lee, K. Miura, H. Hasegawa, M. Tsunoda, F. Matsukura, and H. Ohno. Tunnel magnetoresistance of 604% at 300k by suppression of ta diffusion in cofeb/mgo/cofeb pseudo-spin-valves annealed at high temperature. *Applied Physics Letters*, 93(8):082508, 2022/05/07 2008.
- [21] Metal Spintronics Team AIST, Spintronics Research Center. Development of mgo-mtj devices. [https://unit.aist.go.jp/src/cie/en_teams/en_teams_metal.html; accessed on 2022-05-08].
- [22] J. C. LEUTENANTSMEYER, M. WALTER, V. ZBARSKY, M. MÜNZENBERG, R. GAREEV, K. ROTT, A. THOMAS, G. REISS, P. PERETZKI, H. SCHUHMANN, M. SEIBT, M. CZERNER, and C. HEILIGER. Parameter space for thermal spin-transfer torque. *SPIN*, 03(01):1350002, 2022/05/11 2013.
- [23] A. K. Geim and K. S. Novoselov. The rise of graphene. *Nature Materials*, 6:183–191, 2007.
- [24] K. S. Novoselov, A. K. Geim, S. V. Morozov, D. Jiang, M. I. Katsnelson, I. V. Grigorieva, S. V. Dubonos, and A. A. Firsov. Two-dimensional gas of massless dirac fermions in graphene. *Nature*, 438:197–200, 11 2005.
- [25] S. V. Morozov, K. S. Novoselov, M. I. Katsnelson, F. Schedin, D. C. Elias, J. A. Jaszczak, and A. K. Geim. Giant intrinsic carrier mobilities in graphene and its bilayer. *Phys. Rev. Lett.*, 100:016602–016606, 2008.
- [26] F. Schedin, A. K. Geim, S. V. Morozov, E. W. Hill, P. Blake, M. I. Katsnelson, and K. S. Novoselov. Detection of individual gas molecules adsorbed on graphene. *Nature Materials*, 6:652–655, 07 2007.
- [27] A.M Shikin, D Farías, V.K Adamchuk, and K.-H Rieder. Surface phonon dispersion of a graphite monolayer adsorbed on ni(111) and its modification caused by intercalation of yb, la and cu layers. *Surface Science*, 424(1):155 – 167, 1999.

- [28] Keun Soo Kim, Yue Zhao, Houk Jang, Sang Yoon Lee, Jong Min Kim, Kwang S. Kim, Jong-Hyun Ahn, Philip Kim, Jae-Young Choi, and Byung Hee Hong. Large-scale pattern growth of graphene films for stretchable transparent electrodes. *Nature*, 457:706–710, 01 2009.
- [29] K. S. Novoselov, A. K. Geim, S. V. Morozov, D. Jiang, Y. Zhang, S. V. Dubonos, I. V. Grigorieva, and A. A. Firsov. Electric field effect in atomically thin carbon films. *Science*, 306(5696):666–669, 2004.
- [30] M.-B. Martin, B. Dlubak, R. S. Weatherup, M. Piquemal-Banci, H. Yang, R. Blume, R. Schloegl, S. Collin, F. Petroff, S. Hofmann, J. Robertson, A. Anane, A. Fert, and P. Seneor. Protecting nickel with graphene spin-filtering membranes: A single layer is enough. *Applied Physics Letters*, 107(1):012408, 2015.
- [31] P U Asshoff, J L Sambricio, A P Rooney, S Slizovskiy, A Mishchenko, A M Rakowski, E W Hill, A K Geim, S J Haigh, V I Fal’ko, I J Vera-Marun, and I V Grigorieva. Magnetoresistance of vertical co-graphene-ni junctions controlled by charge transfer and proximity-induced spin splitting in graphene. *2D Materials*, 4(3):031004, 2017.
- [32] Shiro Entani, Takeshi Seki, Yuya Sakuraba, Tatsuya Yamamoto, Saburo Takahashi, Hiroshi Naramoto, Koki Takanashi, and Seiji Sakai. Magnetoresistance effect in $\text{fe}_2\text{0ni}_8\text{0}$ /graphene/ $\text{fe}_2\text{0ni}_8\text{0}$ vertical spin valves. *Applied Physics Letters*, 109(8):082406, 2019/03/06 2016.
- [33] T. M. G. Mohiuddin, E. Hill, D. Elias, A. Zhukov, K. Novoselov, and A. Geim. Graphene in multilayered cpp spin valves. *IEEE Transactions on Magnetics*, 44(11):2624–2627, Nov 2008.
- [34] Muhammad Zahir Iqbal, Muhammad Waqas Iqbal, Jae Hong Lee, Yong Seung Kim, Seung-Hyun Chun, and Jonghwa Eom. Spin valve effect of nife/graphene/nife junctions. *Nano Research*, 6(5):373–380, May 2013.
- [35] M. Z. Iqbal, M. W. Iqbal, Xiaozhan Jin, Changyong Hwang, and Jonghwa Eom. Interlayer dependent polarity of magnetoresistance in graphene spin valves. *J. Mater. Chem. C*, 3:298–302, 2015.
- [36] Feng Li, Tian Li, and Xinyi Guo. Vertical graphene spin valves based on $\text{la}_2/3\text{sr}_1/3\text{mno}_3$ electrodes. *ACS Applied Materials & Interfaces*, 6(2):1187–1192, Jan 2014.

- [37] Wan Li, Lin Xue, H. D. Abruña, and D. C. Ralph. Magnetic tunnel junctions with single-layer-graphene tunnel barriers. *Phys. Rev. B*, 89:184418, May 2014.
- [38] Jing-Jing Chen, Jie Meng, Yang-Bo Zhou, Han-Chun Wu, Ya-Qing Bie, Zhi-Min Liao, and Da-Peng Yu. Layer-by-layer assembly of vertically conducting graphene devices. *Nature Communications*, 4:1921, May 2013. Article.
- [39] S. Mandal and S. K. Saha. Ni/graphene/ni nanostructures for spintronic applications. *Nanoscale*, 4:986–990, 2012.
- [40] Enrique D. Cobas, Olaf M. J. van 't Erve, Shu-Fan Cheng, James C. Culbertson, Glenn G. Jernigan, Konrad Bussman, and Berend T. Jonker. Room-temperature spin filtering in metallic ferromagnet–multilayer graphene–ferromagnet junctions. *ACS Nano*, 10(11):10357–10365, 2016.
- [41] Iqbal Muhammad Zahir, Siddique Salma, and Hussain Ghulam. Spin valve effect of 2d-materials based magnetic junctions. *Advanced Engineering Materials*, 20(5):1700692, 2018.
- [42] Muhammad Zahir Iqbal, Salma Siddique, Ghulam Hussain, and Muhammad Waqas Iqbal. Room temperature spin valve effect in the nife/gr–hbn/co magnetic tunnel junction. *J. Mater. Chem. C*, 4:8711–8715, 2016.
- [43] M. Piquemal-Banci, R. Galceran, S. Caneva, M.-B. Martin, R. S. Weatherup, P. R. Kidambi, K. Bouzehouane, S. Xavier, A. Anane, F. Petroff, A. Fert, J. Robertson, S. Hofmann, B. Dlubak, and P. Seneor. Magnetic tunnel junctions with monolayer hexagonal boron nitride tunnel barriers. *Applied Physics Letters*, 108(10):102404, 2016.
- [44] V. M. Karpan, P. A. Khomyakov, G. Giovannetti, A. A. Starikov, and P. J. Kelly. Ni(111)|graphene|h–bn junctions as ideal spin injectors. *Physical Review B*, 84(15):153406–, 10 2011.
- [45] Yeonchoo Cho, Young Cheol Choi, and Kwang S. Kim. Graphene spin-valve device grown epitaxially on the ni(111) substrate: A first principles study. *The Journal of Physical Chemistry C*, 115(13):6019–6023, 04 2011.

- [46] Tesfaye Abtew, Bi-Ching Shih, Sarbajit Banerjee, and Peihong Zhang. Graphene–ferromagnet interfaces: hybridization, magnetization and charge transfer. *Nanoscale*, 5:1902–1909, 2013.
- [47] Brian J. Schultz, Chernu Jaye, Patrick S. Lysaght, Daniel A. Fischer, David Prendergast, and Sarbajit Banerjee. On chemical bonding and electronic structure of graphene–metal contacts. *Chem. Sci.*, 4:494–502, 2013.
- [48] Maxim Ziatdinov, Shintaro Fujii, Koichi Kusakabe, Manabu Kiguchi, Takehiko Mori, and Toshiaki Enoki. Direct imaging of monovacancy-hydrogen complexes in a single graphitic layer. *Phys. Rev. B*, 89:155405–155420, Apr 2014.
- [49] Maxim Ziatdinov, Shintaro Fujii, Koichi Kusakabe, Manabu Kiguchi, Takehiko Mori, and Toshiaki Enoki. Visualization of electronic states on atomically smooth graphitic edges with different types of hydrogen termination. *Phys. Rev. B*, 87:115427–115434, Mar 2013.
- [50] Naoki Morishita, Gagus Ketut Sunnardianto, Satoaki Miyao, and Koichi Kusakabe. Theoretical analysis of pseudodegenerate zero-energy modes in vacancy-centered hexagonal armchair nanographene. *Journal of the Physical Society of Japan*, 85(8):084703–084711, 2016.
- [51] Satoaki Miyao, Naoki Morishita, Gagus Ketut Sunnardianto, and Koichi Kusakabe. Structure deformation and level splitting in vacancy-centered hexagonal armchair nanographene. *Journal of the Physical Society of Japan*, 86(3):034802–034805, 2017.
- [52] M. Ziatdinov, H. Lim, S. Fujii, K. Kusakabe, M. Kiguchi, T. Enoki, and Y. Kim. Chemically induced topological zero mode at graphene armchair edges. *Phys. Chem. Chem. Phys.*, 19:5145–5154, 2017.
- [53] M. Weser, Y. Rehder, K. Horn, M. Sicot, M. Fonin, A. B. Preobrajenski, E. N. Voloshina, E. Goering, and Yu. S. Dedkov. Induced magnetism of carbon atoms at the graphene/ni(111) interface. *Applied Physics Letters*, 96(1):012504–012505, 2010.
- [54] Maëlis Piquemal-Banci, Regina Galceran, Marie-Blandine Martin, Florian Godel, Abdelmadjid Anane, Frederic Petroff, Bruno Dlubak, and Pierre Seneor. 2d-MTJs: introducing 2d materials in magnetic tunnel junctions. *Journal of Physics D: Applied Physics*, 50(20):203002, apr 2017.

- [55] Yusuf Wicaksono, Shingo Teranishi, Kazutaka Nishiguchi, and Koichi Kusakabe. Tunable induced magnetic moment and in-plane conductance of graphene in ni/graphene/ni nano-spin-valve-like structure: A first principles study. *Carbon*, 143:828–836, 2019.
- [56] Yusuf Wicaksono, Halimah Harfah, Gagus Ketut Sunnardianto, Muhammad Aziz Majidi, and Koichi Kusakabe. Colossal in-plane magnetoresistance ratio of graphene sandwiched with ni nanostructures. *RSC Advances*, 12(22):13985–13991, 2022.
- [57] Halimah Harfah, Yusuf Wicaksono, Gagus Ketut Sunnardianto, Muhammad Aziz Majidi, and Koichi Kusakabe. High magnetoresistance of a hexagonal boron nitride–graphene heterostructure-based mtj through excited-electron transmission. *Nanoscale Advances*, 4(1):117–124, 2022.
- [58] M. Born and R. Oppenheimer. Zur quantentheorie der molekeln. *Annalen der Physik*, 389(20):457–484, 1927.
- [59] D. M. Ceperley and B. J. Alder. Ground state of electron gas by stochastic method. *Phys.Rev. Lett.*, 45:566, 1980.
- [60] S. J. Wright J. Nocedal. *Numerical Optimization*. Springer, 1999.
- [61] David Vanderbilt. Soft self-consistent pseudopotentials in a generalized eigenvalue formalism. *Phys. Rev. B*, 41:7892–7895, Apr 1990.
- [62] S. Y. Zhou, G. H. Gwon, A. V. Fedorov, P. N. First, W. A. De Heer, D. H. Lee, V. Guinea, A. H. Castro Neto, and A.Lanzara. Substrate induced band gap opening in epitaxial graphene. *Natt. Mat.*, 6:770, 2007.
- [63] Niharika Joshi, Nirmalya Ballav, and Prasenjit Ghosh. Hydrogen-induced reversal of spin alignment in graphene supported on ni(111) surface. *Phys. Rev. B*, 86:121411, Sep 2012.
- [64] Paolo Giannozzi, Stefano Baroni, Nicola Bonini, Matteo Calandra, Roberto Car, Carlo Cavazzoni, Davide Ceresoli, Guido L Chiarotti, Matteo Cococcioni, Ismaila Dabo, Andrea Dal Corso, Stefano de Gironcoli, Stefano Fabris, Guido Fratesi, Ralph Gebauer, Uwe Gerstmann, Christos Gougoussis, Anton Kokalj, Michele Lazzeri, Layla Martin-Samos, Nicola Marzari, Francesco Mauri, Riccardo Mazzarello, Stefano Paolini, Alfredo Pasquarello, Lorenzo Paulatto, Carlo Sbraccia, Sandro Scandolo, Gabriele

- Scaluzero, Ari P Seitsonen, Alexander Smogunov, Paolo Umari, and Renata M Wentzcovitch. Quantum espresso: a modular and open-source software project for quantum simulations of materials. *Journal of Physics: Condensed Matter*, 21(39):395502, 2009.
- [65] John P. Perdew, Kieron Burke, and Matthias Ernzerhof. Generalized gradient approximation made simple. *Phys. Rev. Lett.*, 77:3865–3868, Oct 1996.
- [66] Thomas Olsen and Kristian S. Thygesen. Random phase approximation applied to solids, molecules, and graphene-metal interfaces: From van der waals to covalent bonding. *Phys. Rev. B*, 87:075111, 2013.
- [67] John P. Perdew, Adrienn Ruzsinszky, Gábor I. Csonka, Oleg A. Vydrov, Gustavo E. Scuseria, Lucian A. Constantin, Xiaolan Zhou, and Kieron Burke. Restoring the density-gradient expansion for exchange in solids and surfaces. *Phys. Rev. Lett.*, 100:136406, Apr 2008.
- [68] Arjun Dahal and Matthias Batzill. Graphene-nickel interfaces: a review. *Nanoscale*, 6:2548–2562, 2014.
- [69] Jayeeta Lahiri, Travis S Miller, Andrew J Ross, Lyudmyla Adamska, Ivan I Oleynik, and Matthias Batzill. Graphene growth and stability at nickel surfaces. *New Journal of Physics*, 13(2):025001, 2011.
- [70] Sergey M. Kozlov, Francesc Viñes, and Andreas Görling. Bonding mechanisms of graphene on metal surfaces. *The Journal of Physical Chemistry C*, 116(13):7360–7366, 2012.
- [71] Daniel Sánchez-Portal, Pablo Ordejón, Emilio Artacho, and José M. Soler. Density-functional method for very large systems with lcao basis sets. *International Journal of Quantum Chemistry*, 65(5):453–461, 2022/05/10 1997.
- [72] José M Soler, Emilio Artacho, Julian D Gale, Alberto García, Javier Junquera, Pablo Ordejón, and Daniel Sánchez-Portal. The siesta method for ab initio order-n materials simulation. *Journal of Physics: Condensed Matter*, 14(11):2745–2779, 2002.
- [73] Mads Brandbyge, José-Luis Mozos, Pablo Ordejón, Jeremy Taylor, and Kurt Stokbro. Density-functional method for nonequilibrium electron transport. *Physical Review B*, 65(16):165401–, 03 2002.

- [74] Nick Papior, Nicolás Lorente, Thomas Frederiksen, Alberto García, and Mads Brandbyge. Improvements on non-equilibrium and transport green function techniques: The next-generation transiesta. *Computer Physics Communications*, 212:8–24, 2017.
- [75] N. Troullier and JoséLuís Martins. Efficient pseudopotentials for plane-wave calculations. *Physical Review B*, 43(3):1993–2006, 01 1991.
- [76] T. Ozaki and H. Kino. Numerical atomic basis orbitals from h to kr. *Physical Review B*, 69(19):195113–, 05 2004.
- [77] T. Ozaki. Variationally optimized atomic orbitals for large-scale electronic structures. *Physical Review B*, 67(15):155108–, 04 2003.
- [78] Daniel Sánchez-Portal, Emilio Artacho, and JoséM Soler. Analysis of atomic orbital basis sets from the projection of plane-wave results. *Journal of Physics: Condensed Matter*, 8(21):3859–3880, 1996.
- [79] P Giannozzi, O Andreussi, T Brumme, O Bunau, M Buongiorno Nardelli, M Calandra, R Car, C Cavazzoni, D Ceresoli, M Cococcioni, N Colonna, I Carnimeo, A Dal Corso, S de Gironcoli, P Delugas, R A DiStasio, A Ferretti, A Floris, G Fratesi, G Fugallo, R Gebauer, U Gerstmann, F Giustino, T Gorni, J Jia, M Kawamura, H-Y Ko, A Kokalj, E Küçükbenli, M Lazzeri, M Marsili, N Marzari, F Mauri, N L Nguyen, H-V Nguyen, A Otero-de-la Roza, L Paulatto, S Poncé, D Rocca, R Sabatini, B Santra, M Schlipf, A P Seitsonen, A Smogunov, I Timrov, T Thonhauser, P Umari, N Vast, X Wu, and S Baroni. Advanced capabilities for materials modelling with quantum espresso. *Journal of Physics: Condensed Matter*, 29(46):465901, 2017.
- [80] Stefan Grimme, Jens Antony, Stephan Ehrlich, and Helge Krieg. A consistent and accurate ab initio parametrization of density functional dispersion correction (dft-d) for the 94 elements h-pu. *The Journal of Chemical Physics*, 132(15):154104, 2022/05/10 2010.
- [81] A. A. Tonkikh, E. N. Voloshina, P. Werner, H. Blumtritt, B. Senkovskiy, G. Güntherodt, S. S. P. Parkin, and Yu. S. Dedkov. Structural and electronic properties of epitaxial multilayer h-bn on ni(111) for spintronics applications. *Scientific Reports*, 6(1):23547, 2016.

- [82] R. W. Lynch and H. G. Drickamer. Effect of high pressure on the lattice parameters of diamond, graphite, and hexagonal boron nitride. *The Journal of Chemical Physics*, 44(1):181–184, 2022/05/10 1966.
- [83] Rolf Landauer. Electrical resistance of disordered one-dimensional lattices. *The Philosophical Magazine: A Journal of Theoretical Experimental and Applied Physics*, 21(172):863–867, 04 1970.
- [84] M. Büttiker, Y. Imry, R. Landauer, and S. Pinhas. Generalized many-channel conductance formula with application to small rings. *Physical Review B*, 31(10):6207–6215, 05 1985.
- [85] Alexander Smogunov, Andrea Dal Corso, and Erio Tosatti. Ballistic conductance of magnetic co and ni nanowires with ultrasoft pseudopotentials. *Physical Review B*, 70(4):045417–, 07 2004.
- [86] Stefan Grimme. Semiempirical gga-type density functional constructed with a long-range dispersion correction. *Journal of Computational Chemistry*, 27(15):1787–1799, 2022/05/10 2006.
- [87] K. Itoh. Electron spin resonance of an aromatic hydrocarbon in its quintet ground state. *Chemical Physics Letters*, 1(5):235 – 238, 1967.
- [88] Edel. Wasserman, Robert Wallace. Murray, William A. Yager, Anthony M. Trozzolo, and Gerald. Smolinsky. Quintet ground states of m-dicarbene and m-dinitrene compounds. *J. Am. Chem. Soc.*, 89(19):5076–5078, 1967.
- [89] Xiaojie Liu, C. Z. Wang, Y. X. Yao, W. C. Lu, M. Hupalo, M. C. Tringides, and K. M. Ho. Bonding and charge transfer by metal adatom adsorption on graphene. *Phys. Rev. B*, 83:235411, Jun 2011.
- [90] Mayra Peralta, Luis Colmenarez, Alejandro López, Bertrand Berche, and Ernesto Medina. Ferromagnetic order induced on graphene by ni/co proximity effects. *Phys. Rev. B*, 94:235407, Dec 2016.
- [91] C. L. Kane and E. J. Mele. Quantum spin hall effect in graphene. *Phys. Rev. Lett.*, 95:226801, Nov 2005.
- [92] Halimah Harfah, Yusuf Wicaksono, Muhammad A. Majidi, and Koichi Kusakabe. Spin-current control by induced electric polarization reversal in ni/hbn/ni: A cross-correlation material. *ACS Applied Electronic Materials*, 2(6):1689–1699, 06 2020.

- [93] Mikko Kataja, Francisco Freire-Fernández, Jorn P. Witteveen, Tommi K. Hakala, Päivi Törmä, and Sebastiaan van Dijken. Plasmon-induced demagnetization and magnetic switching in nickel nanoparticle arrays. *Applied Physics Letters*, 112(7):072406, 2022/05/11 2018.

This page intentionally left blank

Academic Achievements

List of Publication

1. YUSUF WICAKSONO, S. Teranishi, K. Nishiguchi, and K. Kusakabe, “Tunable induced magnetic moment and in-plane conductance of graphene in Ni/graphene/Ni nano-spin-valve-like structure: A first principles study,” *Carbon* 2019, 143, 828– 836.
2. YUSUF WICAKSONO, H. Harfah, G. K. Sunnardianto, M. A. Majidi, and K. Kusakabe, “Colossal In-plane Magnetoresistance Ratio of Graphene Sandwiched with Ni Nanostructures,” *RSC Adv.*, 2022, 12, 13985-13991.
3. H. Harfah*, YUSUF WICAKSONO*, G. K. Sunnardianto, M. A. Majidi, and K. Kusakabe, “High magnetoresistance of a hexagonal boron nitride–graphene heterostructure-based MTJ through excited-electron transmission,” *Nanoscale Adv.*, 2022, 4, 117-124. (*Co-first author)
4. YUSUF WICAKSONO, H. Harfah, G. K. Sunnardianto, M. A. Majidi, and K. Kusakabe, “Effect of interface on the graphene Dirac cone control in a Ni/hBN-graphene-hBN/Ni magnetic junction for spin-mechatronics device”, under 2nd round peer-review after revision in *RSC Advances*.
5. G. K. Sunnardianto, YUSUF WICAKSONO, H. Harfah, K. Kusakabe, “Discovery of nanographene for hydrogen storage solving low reversibility issues”, under peer-review in *Int. Journal of Hydrogen Storage*.
6. H. Harfah*, YUSUF WICAKSONO*, M. A. Majidi, and K. Kusakabe, “Spin-Current Control by Induced Electric Polarization Reversal in Ni/hBN/Ni: A Cross-Correlation Material,” *ACS Appl. Electron. Mater.* 2020, 2, 6, 1689–1699. (*Co-first author)

7. K. Kusakabe, K. Nishiguchi, S. Teranishi, YUSUF WICAKSONO, “Edge States Caused by Shift of Dirac Points at the Armchair Edge of Distorted nanographene,” J. Phys. Soc. Jpn. 2018, 87, 084716.
8. M A Majidi, YUSUF WICAKSONO, A D Fauzi, A Taufik, R Saleh and A Rusydi, “Theoretical Investigation on the Magnetization Enhancement of Fe₃O₄-Reduced Graspene Oxide Nanoparticle System”, IOP Conference Series: Material Science and Engineering 2017, 1, 188, 012033.
9. YUSUF WICAKSONO, A. Bupu, H. Harfah, G. K. Sunnardianto, and K. Kusakabe, “Spin-flipping Mechanism of Graphene Induced Magnetic Moment in Gr/Ni(111) by Giving Mechanical Pressure through Ni-based Metal Complex”, under preparation
10. YUSUF WICAKSONO, H. Harfah, G. K. Sunnardianto, M. A. Majidi, and K. Kusakabe, “The influence of van der Waals interaction at interface in controlling graphene Dirac cone Fermi Energy in Ni/atomic gas-graphene magnetic junction”, under preparation.

Fellowships/Awards

Fellowships

1. Japan Society for the Promotion of Science (JSPS), Research Fellow for Young Scientist DC1, April 1st, 2020 – March 31st, 2023

Awards

1. Japan International Agency Corporation (JICA), Scholarship for master course and internship (Innovative Asia Program, ID Number D1707483), October 1st, 2017 – March 31st, 2020
2. The International Symposium for Materials Scientists: Inspiration for Innovation by Interaction, Osaka, Japan, Best Oral Presentation, December 2018

Fundings

1. Japan Society for the Promotion of Science (JSPS)-KAKENHI, 2021 Special Researcher Incentive Fee, Grant No: 20J22909, “Theoretical

Study of Spintronics Devices Based on Two-Dimensional Materials”,
Budget Amount: 2,500,000 Yen, April 1st, 2020 – March 31st, 2023
(<https://kaken.nii.ac.jp/grant/KAKENHI-PROJECT-20J22909/>)

Internship

1. Nano-carbon Materials Group, Research Incubation Center, Innovation and Business Development Headquarters, Daicel Corporation, Research Intern, “Detonation soot as Hydrogen storage and generation” October 1st, 2019 – March 31st, 2020, Supervisor: Dr. Masahiro Nishikawa

Oral Presentations

1. YUSUF WICAKSONO, H. Harfah, G. K. Sunnardianto, M. A. Majidi, and K. Kusakabe, “Controlling the Gapped Dirac Cone of Graphene through Pseudospin to Achieve Colossal in-Plane Magnetoresistance”, *Materials Info 2022*, March 2022, Online.
2. H. Harfah, YUSUF WICAKSONO, G. K. Sunnardianto, M. A. Majidi, K. Kusakabe, “Realizing a Novel Functionality on 2D Materials Based Magnetic Tunnel Junction”, *Materials Info 2022*, March 2022, Online.
3. YUSUF WICAKSONO, H. Harfah, G. K. Sunnardianto, M. A. Majidi, and K. Kusakabe, “The Importance of Interface in Controlling Mass Gapped Dirac Cone of Graphene through Pseudospin via Magnetic Proximity Effect”, the 69th JSAP Spring Meeting, March 2022, Online.
4. H. Harfah, YUSUF WICAKSONO, M. A. Majidi, K. Kusakabe, “Understanding the Optimum Spin-Current Control by Induced Electric Polarization Reversal in hBN-based Magnetic Tunnel Junction”, *The International Symposium for Nano Science*, November 2019, Osaka, Japan.
5. YUSUF WICAKSONO, H. Harfah, and K. Kusakabe, “A Comparison of Theoretical Estimate of the Energy Barrier between Bi-stable state of hBN-based Magnetic Tunnel Junction”, the 80th JSAP Autumn Meeting, September 2019, Hokkaido, Japan.
6. YUSUF WICAKSONO, H. Harfah, and K. Kusakabe, “The Influence of Symmetry on the Charge Transfer Mechanism of Ni/graphene/Ni Nano-Spin-Valve Structure”, *5th International Symposium on Current*

Progress in Mathematics and Sciences 2019 (5th ISCPMS 2019), July 2019, Depok, Indonesia

7. H. Harfah, YUSUF WICAKSONO, M. A. Majidi, K. Kusakabe, “Influence of Stacking Arrangement of the 2D Materials-Based Spin Valve on Magnetoresistance Performance: A First Principles Study of Ni/hBN/Ni Spin Valve”, The 66th JSAP Spring meeting, Tokyo, March 2019
8. YUSUF WICAKSONO, H. Harfah, and K. Kusakabe, “In-plane Magnetoresistance of Graphene in Ni/Graphene/Ni Spin-valve-like Structure: A New Prospective of Spin-logic Device”, the 66th JSAP Spring Meeting, March 2019, Tokyo, Japan.
9. YUSUF WICAKSONO, S. Teranishi, K. Nishiguchi, and K. Kusakabe, “In-plane Magnetoresistance of Graphene in Ni/graphene/Ni Nano-Spin-Valve-Like Structure: The Importance of Stacking Arrangement at the Interface”, Joint Seminar on Graphene and Related 2D Materials, January 2019, Osaka, Japan.
10. YUSUF WICAKSONO, S. Teranishi, K. Nishiguchi, and K. Kusakabe, “Tunable Induced Magnetic Moment and In-Plane Conductance of Graphene in Ni/Graphene/Ni Nano Spin-Valve Like Structure: A First Principles Study”, The International Symposium for Materials Scientists: Inspiration for Innovation by Interaction, December 2018, Osaka, Japan.
11. YUSUF WICAKSONO, A. D. Fauzi, M. A. Majidi, A. Taufik, R. Saleh, and A. Rusydi, “Theoretical Investigation on The Magnetization Enhancement of Fe₃O₄-Reduced Graphene Oxide Nanoparticle System”, International Symposium on Current Progress in Functional Materials, July 2017, Bali, Indonesia
12. YUSUF WICAKSONO, A. D. Fauzi, M. A. Majidi, “Dynamical Mean-Field Theoretical Approach to Explore the Magnetic Field Dependence of Fe₃O₄ - Reduced Graphene Oxide Nanoparticle Systems”, The 9th Seminar on Magnetic Materials, October 2015, Palembang, Indonesia

Poster Presentations

1. H. Harfah, YUSUF WICAKSONO, G. K. Sunnardianto, M. A. Majidi, K. Kusakabe, “High magnetoresistance of hexagonal boron nitride-

graphene heterostructure-based MTJ through excited-electron transmission”, the 69th JSAP Spring Meeting, March 2022, Online.

2. YUSUF WICAKSONO, H. Harfah, and K. Kusakabe, “High Magnetoresistance Ratio on the In-plane Conductance of Graphene in Ni/Graphene/Ni Nanostructure”, the 68th JSAP Spring Meeting, March 2021, Online.
3. YUSUF WICAKSONO, H. Harfah, and K. Kusakabe, “Theoretical Study on Optical-induced Magnetic Tunnel Junction based on Gr-hBN Heterostructure”, the JSAP Kansai Branch Meeting, January 2021, Online.
4. H. Harfah, YUSUF WICAKSONO, K. Kusakabe, “Optimizing the Spin-Current Control by Induced Electric-Polarization Reversal in hBN-based Magnetic Tunnel Junction”, The 22nd Asian Workshop on First-Principles Electronic Structure Calculations, October 2019, Osaka, Japan.
5. YUSUF WICAKSONO, H. Harfah, and K. Kusakabe, “First Principles Study on Ni(111)/hBN/Co(0001): Toward Realization of hBN-based Spin-Valve Nanostructure as Cross-Correlation Materials”, Recent Progress on Graphene and 2D Materials Research (RPGR) 2019, October 2019, Matsue, Japan.
6. YUSUF WICAKSONO, H. Harfah, and K. Kusakabe, “Magnetic Field Dependence of Opening and Closing Dirac Cone in Ni/Graphene/Ni nano-spin-valve-like structure”, 1and2DM International Conference, January 2019, Tokyo, Japan.
7. H. Harfah, YUSUF WICAKSONO, and K. Kusakabe, “A Theoretical Estimate of the Energy Barrier between Bi-stable state in Ni/hBN/Ni”, The 11th annual Recent Progress in Graphene and Two-dimensional Materials Research Conference (RPGR), October 2019, Matsue, Japan.
8. H. Harfah, YUSUF WICAKSONO, M. A. Majidi, K. Kusakabe, “Spin-Current Control by Induced Electric-Polarization Reversal in Ni/hBN/Ni Magnetic Tunnel Junction: A Cross-Correlation Materials”, The 80th JSAP Autumn Meeting, September 2019, Hokkaido, Japan.
9. H. Harfah, YUSUF WICAKSONO, M. A. Majidi, K. Kusakabe, “First-Principles Studies of Ni/hBN/Ni nano-spin-valve-like Structure for Spin

Electronics”, 1and2DM International Conference, January 2019, Tokyo, Japan.

Acknowledgments

First, I would like to express my gratitude to Allah SWT., who allowed me to study and do research until I got my Ph.D. degree. Second, I gratefully acknowledge the Japan Society for the Promotion of Science (JSPS) for giving me a fellowship to pursue a doctoral degree. Third, I also acknowledge the research funding for supporting my research in the Doctoral course from JSPS-KAKENHI with grant no. 20J22909 through Grant-in-Aid for Young Scientists. The calculation in this thesis were performed at the computer center of Kyushu University. This thesis is dedicated to my late father (Dr. Triyono M.Eng.Sc.). He always encouraged me to pursue a higher degree and seek opportunities to obtain a doctoral degree and research experience abroad, especially in Japan. May Allah SWT. pleased with him in the hereafter. Finally, I would like to give my utmost gratitude and respect to the following people:

- Professor Koichi Kusakabe. It was an honor and an excellent opportunity for me to have Prof. Koichi Kusakabe as my supervisor during my Master and Doctoral course. I would like to express my gratitude for his tremendous and kind effort in giving guidance, constructive while critical comments, and his sincerity during my five years of study and research in Japan.
- Professor Hajime Ishihara. For his sincere and kind guidance while staying in Ishihara-Laboratory. His great effort helps me to complete my doctoral thesis and get my doctoral degree.
- Professor Masaaki Ashida and Hidekazu Tanaka. I would like to give my gratitude for their willingness and valuable time to be a member of my doctoral defense reviewer committee. I also would like to thank them for the fruitful discussion and their constructive comments during the defense.

- Ms. Toshika Yura for her support and help arranging all the administration work related to research and study.
- My wife, Ms. Halimah Harfah and my mother, Ms. Sri Ambarwati. I would like to give my utmost gratitude for their unfilial love, unwavering support, and endless encouragement (including their supplication to Allah SWT.) during my study, research, and everyday life.
- My beloved son, Yusha Wicaksono, for being my strength in doing all the work and research.
- Last but not least, all my friends in the Kusakabe group. There were so many great people from the start of my Master until getting my Ph.D. (Dr. Nishiguchi, Mr. Matsushita, Mr. James, Dr. Teranishi, Mr. Akiyama, Mr. Tamagaki, Mr. Oishi, and Mr. Ouchi) who supported me in adapting my life in Japan, gave fruitful discussions and advice during my research, and help me to solve my daily life problem in Japan. I would like to cherish our togetherness, beautiful memories, and friendship.